

ELECTRODEPOSITION OF MATERIALS  
FROM NOVEL SOLVENTS

by

WILLIAM DONALD SIDES

QIANG HUANG, COMMITTEE CHAIR  
AMANDA KOH  
DAWEN LI  
QING PENG  
JOHN WILLIAM VAN ZEE

A DISSERTATION

Submitted in partial fulfillment of the requirements  
for the degree of Doctor of Philosophy  
in the Department of Chemical and Biological Engineering  
in the Graduate School of  
The University of Alabama

TUSCALOOSA, ALABAMA

2019

Copyright William Donald Sides 2019  
ALL RIGHTS RESERVED

## **ABSTRACT**

The electrodeposition of metals and alloys is explored with a focus on solvents and additives capable of reducing or eliminating hydrogen evolution while operating at highly cathodic potentials. The nucleation and growth behavior of binary codepositing systems are modelled in Chapter 2. Deep eutectic solvents based on choline chloride and urea are demonstrated to be capable of electrodepositing metallic manganese for the first time in Chapter 3. Chapter 4 describes the first time manganese has been incorporated into an electrodeposited magnetic iron-group alloy.

Water-in-salt electrolytes are applied to the electrodeposition of metals in Chapters 5 and 6. These electrolytes are shown to suppress the proton reduction reaction and subsequent hydrogen evolution in aqueous systems. The tetrabutylammonium ion is also shown to be capable of suppression of proton reduction. The origins of this suppression are examined in Chapter 6, and it is determined that the additive adsorbs onto the electrode surface, blocking proton access. The suppressing behaviors of tetrabutylammonium and water-in-salt electrolytes are combined to achieve significant suppression of proton reduction and the ability to electrodeposit metals at highly negative cathodic potentials. Chapter 6 describes the use of these solvents to electrodeposit ruthenium for interconnect applications.

The origin of enhanced superconductivity in rhenium electrodeposited from water-in-salt electrolytes is explored in Chapter 5. A disordered atomic structure is found to be highly correlated with enhanced superconductivity.

## LIST OF ABBREVIATIONS AND SYMBOLS

$A$	Nucleation rate per active site
AFM	Atomic force microscopy
$C_0$	Bulk concentration of active species
$c$	Concentration
ChCl	Choline chloride
CI(G)S	Copper indium (gallium) selenide
CV	Cyclic voltammogram
CVD	Chemical vapor deposition
$D$	Diffusion coefficient
$D$	Grain size
DA	Single donor, single acceptor of hydrogen bonds
DAA	Single donor, double acceptor of hydrogen bonds
DDA	Double donor, single acceptor of hydrogen bonds
DDAA	Double donor, double acceptor of hydrogen bonds
DES	Deep eutectic solvent
$E$	Electric potential
$E_A$	Activation energy
EDS	Energy dispersive x-ray spectroscopy
EIS	Electrochemical impedance spectroscopy
EQCM	Electrochemical quartz crystal microbalance

$F$	Faraday's constant
FM	Frank-van der Merwe
$H_c$	Magnetic coercivity
HBD	Hydrogen bond donor
HER	Hydrogen evolution reaction
$i$	Current density
$K$	Crystallite shape factor
$k_{cap}$	Capacitive current density constant
$M$	Molar mass
$M_s$	Saturation magnetization
M-H	Magnetic field strength versus magnetization
$N_0$	Number density per active site
PPMS	Physical property measurement system
$R$	Gas constant
RDE	Rotating disk electrode
RMS	Root mean square
SCE	Saturated calomel reference electrode
SEM	Scanning electron microscopy
SIMS	Secondary ion mass spectroscopy
SK	Stranski-Krastanov
STEM	Scanning transmission electron microscopy
$T$	Temperature
$T_c$	Critical temperature of superconductivity

$t$	Time
TBA	Tetrabutylammonium
TEM	Transmission electron microscopy
U	Urea
UPD	Underpotential deposition
VSM	Vibrating sample magnetometry
VW	Volmer-Weber
WiSE	Water-in-salt electrolyte
XRD	X-ray diffraction
XRF	X-ray fluorescence
$z$	Number of electrons transferred per molecule reduced
$\alpha$	Dimensionless nucleation parameter
$\beta$	Full peak width at half maximum
$\Delta G_f$	Standard Gibbs free energy of formation
$\theta$	Diffraction angle
$\lambda$	Wavelength
$\mu_0$	Vacuum permeability
$\nu$	Kinematic viscosity
$\rho$	Density
$\sigma$	Standard deviation
$\tau_{cap}$	Capacitive charging time constant
$\omega$	Angular rotation rate

## **ACKNOWLEDGEMENTS**

I would like to thank everyone who supported and guided me throughout my time at The University of Alabama. My PhD advisor Qiang Huang provided me with invaluable guidance both in research and in life. I truly appreciate his feedback on manuscripts, his backing of my academic travel and networking opportunities, and his tremendous support of my professional development.

I would like to acknowledge my committee members Amanda Koh, Dawen Li, Qing Peng, and John William Van Zee, for their invaluable guidance and suggestions. I wish to recognize Shuvodeep De, Yang Hu, Joseph Ortenero, Tim Brusuelas, William Freeman, Nikolas Kassouf, Tyler Lyons, Dan Mantoni, Christopher Menas, Ryan Morelock, Keaton Ramsey, John White, and all other members of my research group for their help. I would also like to thank my colleagues in the graduate school Matthew Confer, Al Gilani, Haoming Yan, and Xiaozhou Yu for encouragement and advice along the way.

Of course, I would not be where I am without the unwavering support of my family, for which I am forever thankful.

Finally, I need to thank all faculty, staff, and students of the Department of Chemical and Biological Engineering at The University of Alabama, as well as the Central Analytical Facility, the Center for Materials for Information Technology, the Chemistry Glass Shop, and the College of Engineering Machine Shop. Financial support by the National Science Foundation, the Graduate Council, and the Research Grant Council at The University of Alabama is greatly appreciated.

## CONTENTS

ABSTRACT .....	ii
LIST OF ABBREVIATIONS AND SYMBOLS.....	iii
ACKNOWLEDGEMENTS .....	vi
LIST OF TABLES.....	xi
LIST OF FIGURES.....	xii
CHAPTER 1. INTRODUCTION.....	1
Motivation.....	1
Electrochemical Methods.....	5
References.....	7
CHAPTER 2. ELECTROCHEMICAL NUCLEATION AND GROWTH OF ANTIMONY TELLURIDE BINARY COMPOUND ON GOLD SUBSTRATE.....	10
Summary.....	10
Introduction.....	10
Experimental.....	12
Results and Discussion.....	13
Voltammetric studies .....	13
Chronoamperometry studies.....	17
Nucleation site characterization .....	24
Conclusion.....	25
Acknowledgements .....	26
References.....	26

Supplementary Information.....	30
<b>CHAPTER 3. ELECTRODEPOSITION OF MANGANESE THIN FILMS ON A ROTATING DISK ELECTRODE FROM CHOLINE CHLORIDE/UREA BASED IONIC LIQUIDS.....</b>	<b>32</b>
Summary.....	32
Introduction.....	32
Experimental.....	34
Results and Discussion.....	36
Characteristics of solvent .....	36
Electrochemical behavior of manganese system.....	40
Effect of glycine.....	47
Characterization of manganese films.....	49
Ag reference electrode.....	51
Conclusion.....	52
Acknowledgements .....	52
References.....	53
Supplementary Information.....	56
<b>CHAPTER 4. ELECTRODEPOSITION OF FERROMAGNETIC FeCo AND FeCoMn ALLOY FROM CHOLINE CHLORIDE BASED DEEP EUTECTIC SOLVENT.....</b>	<b>58</b>
Summary.....	58
Introduction.....	58
Experimental.....	60
Results and Discussion.....	62
Conclusion.....	79
Acknowledgements .....	79
References.....	79

CHAPTER 5. GRAIN GROWTH AND SUPERCONDUCTIVITY OF RHENIUM ELECTROPOSITED FROM WATER-IN-SALT ELECTROLYTES .....	84
Summary.....	84
Introduction.....	84
Methods.....	86
Results and Discussion.....	89
Electrochemical behavior of rhenium deposition electrolytes.....	89
Superconductivity and grain structure of electrodeposited rhenium .....	95
Impurity analysis of water-in-salt deposited Re .....	100
Conclusion.....	102
Acknowledgements .....	103
References.....	103
Supplementary Information.....	106
CHAPTER 6. RUTHENIUM ELECTRODEPOSITION FROM WATER-IN-SALT ELECTROLYTES FOR INTERCONNECT APPLICATIONS AND THE INFLUENCE OF TETRABUYTLAMMONIUM.....	107
Summary.....	107
Introduction.....	107
Methods.....	110
Results and Discussion.....	112
Tetrabutylammonium additive and water-in-salt electrolyte .....	112
Ruthenium deposition .....	118
Conclusion.....	122
Acknowledgements .....	123
References.....	123
CHAPTER 7. CONCLUSIONS AND RECOMMENDATIONS .....	127

References.....	129
APPENDIX.....	131
Ongoing Work.....	131
Manganese and Mn-Re alloys.....	131
Molybdenum rhenium alloys .....	134
References.....	137

## LIST OF TABLES

Table 2-1. Symbols and definitions for nucleation modelling equations .....	20
Table 2-2. Fitted parameters for current transients .....	20
Table 2-3. Calculated $\alpha$ values for current transients.....	22
Table 4-1. Conditions of potentiostatic deposition experiments .....	66
Table 4-2. Properties of FeCo alloy films .....	70
Table 4-3. Properties of FeCoMn alloy films.....	74
Table 5-1. Change in impurity elements within Re upon annealing .....	102

## LIST OF FIGURES

Figure 2–1. CVs and EQCM measurements of solutions containing Te and Sb.....	13
Figure 2–2. CVs of solutions containing Te and Sb in various ratios .....	15
Figure 2–3. Experimental current transients for potential step experiments .....	18
Figure 2–4. $i_{3D}$ portion of current transients normalized to $t_m$ and $i_m$ .....	23
Figure 2–5. Composition variation along a SbTe nucleation site .....	24
Figure S 2–1. Te current transients plotted against the model.....	30
Figure S 2–2. Sb current transients plotted against the model.....	30
Figure S 2–3. Sb-Te current transients plotted against the model .....	31
Figure 3–1. Cyclic voltammogram of ChCl-U.....	37
Figure 3–2. Viscosity and conductance of ChCl-U with $MnCl_2 \cdot 4H_2O$ .....	40
Figure 3–3. CV of ChCl-U containing various amounts of Mn(II) .....	41
Figure 3–4. CV of ChCl-U containing Mn(II) at various scan rates.....	42
Figure 3–5. CVs of ChCl-U containing Mn(II) to different cathodic limits.....	43
Figure 3–6. CV of ChCl-U containing Mn(II) with measurements of film thickness.....	46
Figure 3–7. Chronoamperometry of manganese deposition .....	47
Figure 3–8. Partial currents of Mn deposition in the presence of glycine .....	48
Figure 3–9. Surface morphologies of Mn deposits.....	50
Figure S 3–1. CV of a Mn and a Pt electrode in ChCl-U.....	56
Figure S 3–2. CV showing the effect of excess urea in ChCl-U .....	56
Figure S 3–3. Images of the substrate after linear sweep voltammetry .....	57
Figure S 3–4. X-ray diffractograms of Mn films.....	57

Figure 4–1. CVs of ChCl-U containing Fe(II) or Co(II).....	62
Figure 4–2. The effect of temperature, rotation rate, and concentration on the CVs.....	65
Figure 4–3. Growth rates of the alloy film.....	67
Figure 4–4. Compositions of FeCo films.....	68
Figure 4–5. CV of ChCl-U containing Fe, Co, and Mn.....	71
Figure 4–6. Compositions of FeCoMn films.....	72
Figure 4–7. Hysteresis loops of FeCo and FeCoMn films.....	73
Figure 4–8. Morphologies of FeCo and FeCoMn films.....	75
Figure 4–9. X-ray diffractograms of FeCo and FeCoMn films.....	76
Figure 4–10. Impurity compositions of FeCo films.....	78
Figure 5–1. Partial and total currents of rhenium deposition.....	90
Figure 5–2. Current efficiencies of rhenium deposition.....	94
Figure 5–3. Resistances of Re films.....	96
Figure 5–4. X-ray diffractograms of Re films.....	97
Figure 5–5. Resistance of Re films deposited on Au and Pd seeds.....	98
Figure 5–6. X-ray diffractograms of Re films taken <i>in-situ</i> during annealing.....	99
Figure 5–7. SIMS depth profiles showing impurity content of Re films.....	101
Figure S 5–1. Re deposition partial current densities from Re depositions on Au strips....	106
Figure S 5–2. Calculated x-ray diffractogram of an ideal Re powder sample.....	106
Figure 6–1. Raman spectra of water with various amounts of LiCl.....	113
Figure 6–2. CVs of acidic solutions with TBA.....	114
Figure 6–3. CVs on an electrode pre-derivatized with TBA.....	115
Figure 6–4. Proton reduction current during TBA injections.....	117
Figure 6–5. CVs of acidic solutions with TBA and/or LiCl.....	118
Figure 6–6. Photographs of Ru solutions.....	119

Figure 6–7. Ruthenium deposition partial currents and current efficiencies.....	120
Figure 6–8. X-ray diffractograms of Ru thin films.....	121
Figure A 1. CVs in a water-in-salt electrolyte containing Mn(II).....	131
Figure A 2. Partial currents and current efficiencies of Mn deposition.....	132
Figure A 3. CVs in a water-in-salt electrolyte containing Mn(II) and Re(VII).....	133
Figure A 4. Image of a Au/Mo/Re/Au stacked structure.....	135
Figure A 5. Superconducting critical temperature of a Re/Mo layered structure.....	136

## CHAPTER 1. INTRODUCTION

### Motivation

Electrochemical deposition is a process in which metal cations in solution are reduced at an electrode to form a solid metal on the surface of the electrode. Often called electroplating when used to fabricate metal films and coatings onto conductive substrates, it has been performed for over a century. Decorative chrome, corrosion and wear protection, and electrical contacts are but a few of the applications where electrodeposition is commonly used in industry today. Electrodeposition has been found to be well-suited for microdevice fabrication, enabling advances such as magnetic hard drive write heads in the late 1970's,<sup>1</sup> and the introduction of copper interconnects in the late 1990's,<sup>2</sup> a key achievement that even up to today has enabled integrated circuits to continue scaling according to Moore's law. A notable feature of electroplating is its conformal coating style – meaning complex substrate geometries can be coated with films of uniform thickness. Additionally, control of the process is straight-forward by adjusting simple process parameters. It typically has mild process conditions, is inexpensive to implement, and can be easily scaled.

Almost all industrial electroplating is carried out in aqueous electrolyte baths. Water provides a convenient solvent, as it is readily available, non-toxic, and can easily dissolve many metal salts. Acid is often added to increase the conductivity of the bath and the solubility of the metal salt precursors. The substrate to be plated acts as the cathode in an electrochemical cell. Dissolved metal ions adjacent to the substrate will be reduced to

their metallic state if the electric potential applied to the substrate is more negative than the reduction potential of the metal ion. By negatively polarizing the substrate, the electrodeposition reaction can be driven forward, and a metallic coating can be deposited. The rate of the reaction can be conveniently determined by measuring the current flowing through the system and applying Faraday's law of electrolysis. Such a scheme works well for metals such as copper, where the reduction potential of  $\text{Cu}^{2+}$  is +0.34 V versus the reduction potential of protons.<sup>3</sup> However, many metals, such as cobalt and chromium, have a reduction potential more negative than (at an overpotential to) the reduction potential of protons from the solvent. The potential applied to the substrate must be more negative than the deposition potential of the metal ion in order to drive the reaction forward, necessitating that for these metals, deposition is accompanied by some amount of proton reduction to hydrogen. In mild cases such as cobalt plating (which is typically performed at current efficiencies greater than 80%), this hydrogen can usually escape the film without causing major issues. In more severe cases, such as typical chromium electroplating processes, hydrogen can become trapped inside the growing film, causing embrittlement within the film or cracks. If the deposition potential of a metal ion is at a sufficient overpotential to proton reduction, however, it becomes impractical to electrodeposit the metal in acidic aqueous media.

Overcoming these limitations with aqueous electrolytes often is often attempted by electrodepositing films from a variety of non-aqueous solvents which are electrochemically stable to a more negative potential than protons or water. Protic and aprotic organic solvents have been used to electrodeposit a variety of elements, such as Al,<sup>4-6</sup> Mg,<sup>7</sup> Au,<sup>8</sup> Si,<sup>9</sup> and alloys including AlMg<sup>7</sup> and ZnTe.<sup>10</sup> Of these, the process to have achieved the most

significant commercial success is Al.<sup>11</sup> The solvents are often expensive and toxic, and the metal precursors added to the solution are sometimes extremely dangerous. More fundamentally, the low conductivity in these baths can lead to poor deposit morphology and uniformity, and the incorporation of organic impurities is often significant.<sup>9</sup> High temperature molten salt electrolytes can overcome the conductivity and metal solubility issues and have been used to achieve electrodeposition of several metals, however extreme process conditions, expense of the solvent and necessary corrosion-resistant process equipment, and toxicity have prevented widespread adoption.

Room temperature ionic liquids are generally defined as salts which remain liquid at below 100 °C.<sup>12</sup> These solvents have been widely studied for aluminum deposition, and they provide high conductivity and can dissolve many metal salts. They have a wide enough potential window to allow for the electrodeposition of alkali metals,<sup>13</sup> refractory metals as well as compound semiconductors.<sup>14</sup> These solvents are often toxic and unstable in the presence of oxygen or water.

Deep eutectic solvents (DES) have much more recently been applied as electrodeposition solvents, retaining many of the desirable properties of room temperature ionic liquids but being much more practical to work with. The mixture of quaternary ammonium salts with hydrogen bond donors such as carboxylic acids or urea, attains a eutectic melting point much lower than either individual component, in many cases below room temperature.<sup>15-16</sup> Although not strictly ionic liquids, DES's physical properties such as viscosity, conductivity, and surface tension are similar to room temperature ionic liquids. They are capable of dissolving many metal salts including metal oxides,<sup>17</sup> and have the benefits of being stable in air, non-toxic, environmentally benign, and inexpensive. Their

low vapor pressure enables elevated process temperatures, allowing for additional process flexibility. These benefits make DES very attractive for electrodeposition solvents, so they have acquired much interest over the most recent decade. The 1:2 molar mixture of choline chloride and urea (ChCl-U) is probably the most frequently used DES in the literature, with a melting point of 12 °C.<sup>16</sup> This system has been used to deposit several metals and alloys,<sup>18-24</sup> including copper indium gallium selenide chalcopyrite solar absorber material from a single bath.<sup>25</sup> In Chapter 3 of this dissertation, the use of this solvent to electrodeposit metallic manganese is described for the first time. Additionally, Mn has been incorporated into electrodeposited magnetic iron-group alloys for the first time through the use of ChCl-U, as described in Chapter 4. Prospects for using this process to fabricate high magnetization devices are discussed.

DES overcome many of the obstacles to commercialization that other non-aqueous solvents typically encounter. However commercial adoption has been slow due to various practical concerns, such as incompatibility with current processing equipment and impurity incorporation into films. Extremely concentrated aqueous solutions of lithium salts were introduced in 2015 as solvents that can enable high voltage aqueous lithium batteries.<sup>26</sup> This so-called water-in-salt electrolyte is capable of suppressing the rate of hydrogen evolution while depositing metals at significant overpotentials to proton reduction. Our group has applied this solvent toward the electrodeposition of materials for the first time,<sup>27</sup> and this dissertation reports on its use for the deposition of Ru for interconnect applications in Chapter 6. This chapter also describes an additional technique to suppress hydrogen evolution in aqueous electrolytes is examined. The addition of a small amount of a hydrophobic cation into the plating bath is shown to inhibit proton

access to the electrode interface, dramatically slowing down the proton reduction reaction. Chapter 5 describes the electrodeposition of superconducting rhenium from a water-in-salt electrolyte. It has been found that metallic Re has enhanced superconducting properties when electrodeposited from water-in-salt electrolytes.<sup>28</sup> The origins of these enhanced properties are explored. The crystallinity of rhenium films is correlated to their superconducting properties, and the disordered atomic structure within electrodeposited Re is responsible. The conditions upon which grain growth occurs in electrodeposited films are thoroughly studied and discussed.

### **Electrochemical Methods**

The field of electrochemistry is extremely diverse, encompassing a vast number of fields, each with their own set of carefully devised experimental and theoretical frameworks. An excellent, in-depth description of these has been written by Bard and Faulkner.<sup>29</sup> This section will present a brief overview of some of the electrochemical methods most frequently used in this work.

All electrochemical work done in this dissertation is performed in a three electrode cell, consisting of a working electrode, counter electrode, and reference electrode. This setup allows the measurement and control of the potential applied to the working electrode, without regard to the Faradaic or Ohmic processes occurring at the counter electrode.

Cyclic voltammograms (CVs) are one of the first tests often performed on an electrochemical system. This test is usually begun at a potential where no current flows and thus no electrochemical reactions take place. The potential of the cathode is then swept at a constant rate toward more negative potentials, and the current flow is measured. Upon

reaching the onset of a reaction, current will be measured through the cell, proportionally to the reaction rate. This current will initially follow the Butler-Volmer equation, until the reactants in the stagnant diffusion boundary layer near the electrode surface are depleted, at which point the current will decrease. This gives rise to characteristic peaks in CVs, whose height depends on the potential sweep rate and the concentration of reactants in the solution.

Alternatively, well-defined solution agitation, such as by a rotating disk electrode, can ensure fresh reactants are continuously provided to the electrode surface. In this operating mode, a mass transfer limiting current would eventually form as a horizontal line in a CV. Its value depends on the rate of reactant replenishment to the electrode surface across a well-established constant boundary layer, and is calculated for the rotating disk electrode by the Levich equation.<sup>30</sup> Upon reaching a defined cathodic potential, the sweep direction is reversed. This allows for the observation of any reverse reactions occurring, such as oxidation of any freshly deposited metal back into the solution phase.

Metal deposition is performed under one of two control modes. In the potentiostatic mode, the potential is held constant while the current is measured. In galvanostatic mode, a constant current is maintained across the cell while the potential required to maintain that current is measured. In cases where proton reduction or other side reactions accompany metal deposition, the current efficiency of the metal deposition reaction is decreased. The efficiency, or fraction of total current going towards the desired deposition reaction, can be calculated using Faraday's law of electrolysis by measuring the amount of deposited metal. The amount can be measured either directly by mass or thickness, or indirectly by

electrochemically stripping the deposit and measuring the amount of electric charge required.

## References

1. Chiu, A.; Croll, I. M.; Heim, D.; R.E, J. J.; Kasiraj, P.; B. Klaassen, K.; Denis Mee, C.; G. Simmons, R., Thin Film Inductive Heads. *IBM Journal of Research and Development* **1996**, *40*, 283-300.
2. Andricacos, P. C.; Uzoh, C.; Dukovic, J. O.; Horkans, J.; Deligianni, H., Damascene copper electroplating for chip interconnections. *IBM Journal of Research and Development* **1998**, *42* (5), 567-574.
3. Vanýsek, P., Electrochemical Series. In *CRC Handbook of Chemistry and Physics*, 96th ed.; Haynes, W. M., Ed. CRC Press: Boca Raton, FL, 2015; pp 5.80-5.89.
4. Couch, D. E.; Brenner, A., A Hydride Bath for the Electrodeposition of Aluminum. *Journal of The Electrochemical Society* **1952**, *99* (6), 234-244.
5. Gálová, M., Electrodeposition of aluminium from organic aprotic solvents. *Surface Technology* **1980**, *11* (5), 357-369.
6. Zhao, Y.; VanderNoot, T. J., Electrodeposition of aluminium from nonaqueous organic electrolytic systems and room temperature molten salts. *Electrochimica Acta* **1997**, *42* (1), 3-13.
7. Connor, J. H.; Reid, W. E.; Wood, G. B., Electrodeposition of Metals from Organic Solutions: V. Electrodeposition of Magnesium and Magnesium Alloys. *Journal of The Electrochemical Society* **1957**, *104* (1), 38-41.
8. Monzon, L. M. A.; Byrne, F.; Coey, J. M. D., Gold electrodeposition in organic media. *Journal of Electroanalytical Chemistry* **2011**, *657* (1), 54-60.
9. Munisamy, T.; Bard, A. J., Electrodeposition of Si from organic solvents and studies related to initial stages of Si growth. *Electrochimica Acta* **2010**, *55* (11), 3797-3803.
10. Heo, P.; Ichino, R.; Okido, M., ZnTe electrodeposition from organic solvents. *Electrochimica Acta* **2006**, *51* (28), 6325-6330.

11. Liu, Q. X.; El Abedin, S. Z.; Endres, F., Electroplating of mild steel by aluminium in a first generation ionic liquid: A green alternative to commercial Al-plating in organic solvents. *Surface and Coatings Technology* **2006**, *201* (3), 1352-1356.
12. Endres, F., Ionic Liquids: Solvents for the Electrodeposition of Metals and Semiconductors. *ChemPhysChem* **2002**, *3* (2), 144-154.
13. Gray, G. E.; Kohl, P. A.; Winnick, J., Stability of sodium electrodeposited from a room temperature chloroaluminate molten salt. *Journal of the Electrochemical Society* **1995**, *142* (11), 3636-3642.
14. Wicelinski, S. P.; Gale, R. J., Gallium Species Electrochemistry in Room Temperature Chloroaluminate Melts. *ECS Proceedings Volumes* **1987**, *1987-7*, 591-601.
15. Abbott, A. P.; Boothby, D.; Capper, G.; Davies, D. L.; Rasheed, R. K., Deep Eutectic Solvents Formed between Choline Chloride and Carboxylic Acids: Versatile Alternatives to Ionic Liquids. *J. Am. Chem. Soc.* **2004**, *126* (29), 9142-9147.
16. Abbott, A. P.; Capper, G.; Davies, D. L.; Rasheed, R. K.; Tambyrajah, V., Novel solvent properties of choline chloride/urea mixtures. *Chemical Communications* **2003**, (1), 70-71.
17. Abbott, A. P.; Capper, G.; Davies, D. L.; McKenzie, K. J.; Obi, S. U., Solubility of metal oxides in deep eutectic solvents based on choline chloride. *J. Chem. Eng. Data* **2006**, *51* (4), 1280-1282.
18. Abbott, A. P.; Capper, G.; McKenzie, K. J.; Ryder, K. S., Electrodeposition of zinc-tin alloys from deep eutectic solvents based on choline chloride. *Journal of Electroanalytical Chemistry* **2007**, *599* (2), 288-294.
19. Chung, P. P.; Cantwell, P. A.; Wilcox, G. D.; Critchlow, G. W., Electrodeposition of zinc-manganese alloy coatings from ionic liquid electrolytes. *Trans. Inst. Metal Finish.* **2008**, *86* (4), 211-219.
20. Abbott, A. P.; El Ttaib, K.; Frisch, G.; McKenzie, K. J.; Ryder, K. S., Electrodeposition of copper composites from deep eutectic solvents based on choline chloride. *Physical Chemistry Chemical Physics* **2009**, *11* (21), 4269-4277.
21. Golgovici, F.; Cojocaru, A.; Nedelcu, M.; Visan, T., VOLTAMMETRIC AND IMPEDANCE STUDIES OF ELECTRODEPOSITION OF Te AND ITS BINARY COMPOUNDS WITH Bi AND Sb

USING CHOLINE CHLORIDE - UREA BASED ELECTROLYTE. *Chalcogenide Lett.* **2009**, 6 (8), 323-333.

22. Gómez, E.; Cojocar, P.; Magagnin, L.; Valles, E., Electrodeposition of Co, Sm and SmCo from a Deep Eutectic Solvent. *Journal of Electroanalytical Chemistry* **2011**, 658 (1-2), 18-24.

23. Bougouma, M.; Elewyck, A.; Steichen, M.; Buess-Herman, C.; Doneux, T., Selenium electrochemistry in choline chloride-urea deep eutectic electrolyte. *Journal of Solid State Electrochemistry* **2012**, 17 (2), 527-536.

24. You, Y. H.; Gu, C. D.; Wang, X. L.; Tu, J. P., Electrodeposition of Ni-Co alloys from a deep eutectic solvent. *Surface and Coatings Technology* **2012**, 206 (17), 3632-3638.

25. Shivagan, D. D.; Dale, P. J.; Samantilleke, A. P.; Peter, L. M., Electrodeposition of chalcopyrite films from ionic liquid electrolytes. *Thin Solid Films* **2007**, 515, 5899-5903.

26. Suo, L.; Borodin, O.; Gao, T.; Olguin, M.; Ho, J.; Fan, X.; Luo, C.; Wang, C.; Xu, K., "Water-in-salt" electrolyte enables high-voltage aqueous lithium-ion chemistries. *Science* **2015**, 350 (6263), 938.

27. Huang, Q.; Lyons, T. W., Electrodeposition of rhenium with suppressed hydrogen evolution from water-in-salt electrolyte. *Electrochemistry Communications* **2018**, 93, 53-56.

28. Huang, Q.; Hu, Y., Electrodeposition of Superconducting Rhenium with Water-in-Salt Electrolyte. *Journal of The Electrochemical Society* **2018**, 165 (16), D796-D801.

29. Bard, A. J.; Faulkner, L. R., *Electrochemical methods: fundamentals and applications*. Second ed.; Wiley New York: 2001.

30. Levich, V. G., *Physicochemical hydrodynamics. : Prentice-Hall international series in the physical and chemical engineering sciences*. Englewood Cliffs, N.J., Prentice-Hall, 1962.: 1962.

## CHAPTER 2. ELECTROCHEMICAL NUCLEATION AND GROWTH OF ANTIMONY TELLURIDE BINARY COMPOUND ON GOLD SUBSTRATE\*

### Summary

The nucleation and growth of SbTe compound on gold substrate has been studied by voltammetric and chronoamperometric methods coupled with quartz microbalance. Direct deposition on transmission microscope grids was performed to determine the compositional evolution of single nuclei. 3D nucleation and growth behaviors were observed for both Te and Sb, despite the presence of under-potential deposition, suggesting a Stranski–Krastanov nucleation mode. Sb deposition follows a progressive nucleation model, whereas Te follows an instantaneous nucleation model. The compound nucleation behavior is found to be influenced more by that of Te, the more noble species, and to proceed more rapidly than either elemental species.

### Introduction

The electrodeposition of binary compounds has become widely studied in the last several years as an effective fabrication method for a number of compounds that are finding interesting advanced applications. Particular interest has been paid to chalcogenide compounds, as these have many unique properties and are capable of being co-electrodeposited. Antimony telluride possesses a unique crystal structure that makes it useful for a number of applications such as thermoelectric generators,<sup>1</sup> solar cells,<sup>2</sup> and

---

\* This chapter was published in the *Journal of The Electrochemical Society* **2018**, 165 (11), W.D. Sides, Q. Huang.

phase change memory,<sup>3</sup> and its electrodeposition from acidic baths has been proven by several researchers.<sup>4-7</sup> From a device perspective, where materials are typically in the shape of thin films or nanostructures, the nucleation and growth of materials at the beginning stage of deposition is of critical importance.

While electrochemical nucleation studies are widely available in the literature for many elements and substrates,<sup>8-15</sup> such studies on codepositing species are rarely available.<sup>16</sup> The nucleation behaviors of a single element on a foreign substrate are classified into three categories, 2D (Frank–van der Merwe, FM), 3D (Volmer–Weber, VW), and 2D followed by 3D (Stranski–Krastanov, SK), depending on the interaction between the substrate and depositing elements.<sup>17</sup> While these three behaviors have all been observed for electrodeposition,<sup>18-20</sup> the 3D VW growth is the most commonly observed among them. On the other hand, nucleation during compound electrodeposition is expected to be influenced by additional factors, such as the thermodynamic energy gained by compound formation during deposition.

This chapter studies the nucleation of SbTe on gold substrates from an acidic aqueous bath. Chronoamperometry studies have been carried out in conjunction with an electrochemical quartz crystal microbalance (EQCM) to determine the nucleation behavior of both antimony and tellurium as well as the binary compound onto gold substrates. Nucleation sites have been observed using transmission electron microscopy (TEM) equipped with elemental analysis to further characterize the nucleation and initial growth behavior of SbTe.

## Experimental

The electrodeposition bath was made by mixing antimony(III) chloride (Alfa Aesar, 99+%) and tellurium(IV) oxide (Alfa Aesar, technical grade) into a concentrated solution of nitric acid (Ricca Chemical, ACS grade) and citric acid (VWR, ACS grade) until dissolved. Solutions were then diluted to 0.21 M citric acid and 1 M nitric acid with 18.2 M $\Omega$  DI water, and the pH was adjusted to 2.3 using ammonium hydroxide (VWR, ACS grade). The typical three-electrode cell was employed, with a saturated Ag/AgCl reference electrode and a Au counter electrode. All potentials referenced to in this chapter are with respect to this reference electrode. The substrate for voltammetric and chronoamperometry experiments was a Au plated EQCM crystal with a Ti adhesion layer, and a plated area of 0.385 cm<sup>2</sup>. Nuclei for transmission electron microscope analysis were electrodeposited on Cu TEM grids (Ted Pella) sputter coated with Au for 60 s at 25 mA (approximately 30 Å) to provide a conductive, electron transparent substrate for deposition and TEM analysis. Electrical and mechanical contact was made with the grids using conductive silver paint.

An Autolab PG320N potentiostat/galvanostat workstation is used for all electrochemical studies, which is equipped with an EQCM module using a 6 MHz crystal. All experiments were performed at room temperature without bath agitation. After depositions, TEM substrates were cleaned by gently dipping them into DI water and were air dried. The deposition bath was refreshed between each experiment. A FEI Tecnai F-20 TEM equipped with an energy dispersive x-ray spectrometer (EDS) was utilized for nuclear characterization.

## Results and Discussion

### Voltammetric studies

Cyclic voltammograms (CV) with EQCM measurements performed on solutions of 5 mM TeO<sub>2</sub>, 10 mM SbCl<sub>3</sub>, and 5 mM TeO<sub>2</sub> + 10 mM SbCl<sub>3</sub> are presented in Figure 2-1. EQCM measurements were coupled with CVs to allow for an easy explanation of the peaks seen in the CV. In the Te(IV) containing solution, an initial cathodic peak due to Te deposition has an onset potential of -0.30 V. The reverse (anodic) CV scan current crosses over the forward (cathodic) scan current, indicating a 3-dimensional nucleation and growth process is occurring at this potential. The underpotential deposition (UPD) of Te on Au is well

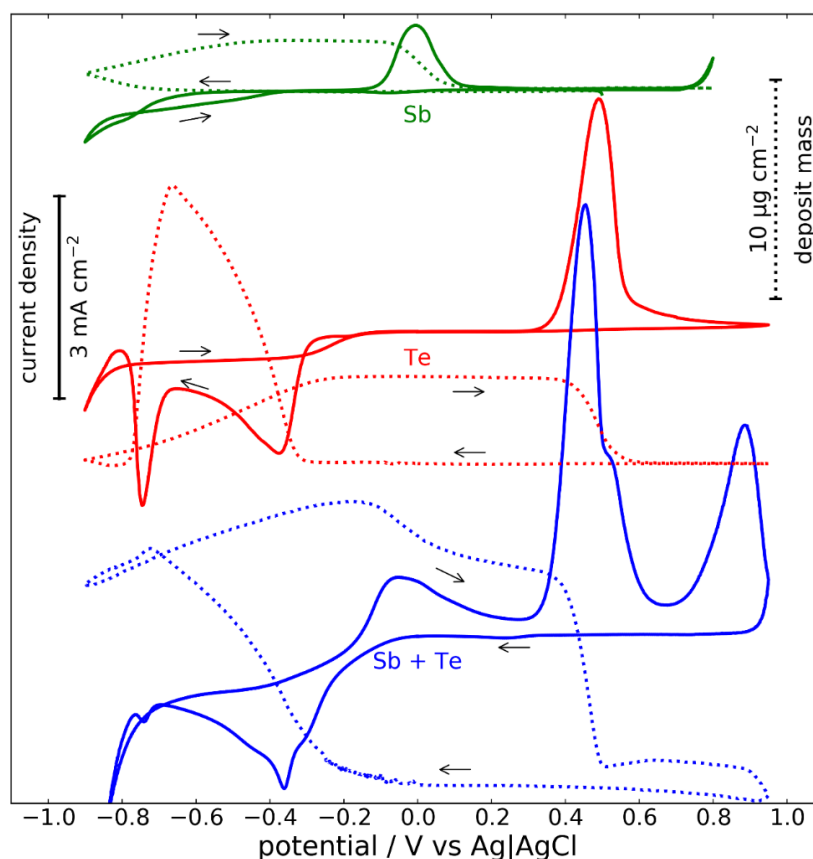


Figure 2-1. CVs (solid lines) and corresponding EQCM measurements (dotted lines) of solutions containing 5 mM TeO<sub>2</sub>, 10 mM SbCl<sub>3</sub>, and 5 mM TeO<sub>2</sub> + 10 mM SbCl<sub>3</sub>. Scan rate 20 mV·s<sup>-1</sup>.

known and has also been studied in the past for the fabrication of SbTe films via an atomic layer deposition approach.<sup>6, 21-25</sup> This UPD is also observed at potentials as positive as 0.04 V in this study. However, the 3D nucleation at more negative potentials observed here is consistent with the literature, where 2D UPD layer formation followed by 3D nucleation (SK growth) was reported and ascribed to an extremely low surface mobility of Te adatoms on the UPD Te monolayer.<sup>20</sup>

At more negative potentials, the Te deposit is stripped cathodically to form Te(-II), beginning at -0.67 V, resulting in a second cathodic peak. A single anodic peak is observed with its peak at 0.49 V, corresponding to anodic stripping of the Te deposited during the reverse scan. The stripping of UPD Te is indistinguishable due to the large amount of Te deposited at overpotential. The Sb(III) containing solution exhibited a small UPD peak, but no distinct cathodic peak related to bulk Sb deposition was observed for the potential range we studied. The slight cathodic current observed below -0.38 V was confirmed by an increasing deposit mass as observed by EQCM to be due to bulk Sb deposition. This current exhibited a crossover for a wide potential window, characteristic of a slow nucleation and growth process, which is also manifested in the accelerating deposition rate observed in EQCM measurements. An anodic stripping peak is observed at 0.00 V.

When Sb and Te are combined in solution, the primary cathodic peak in the CV is at the potential -0.36 V and is attributed to the codeposition of a SbTe compound. A small shoulder at -0.30 V is attributed to elemental Te deposition, and a small peak at -0.74 V is attributed to the cathodic stripping of Te. It is noted that both the small size of this peak and the only slight reduction in deposit mass after this peak (as compared to pure Te solution, which loses nearly all deposited mass) indicate that the majority of the Te is not

cathodically stripped. The free energy of compound formation stabilizes this SbTe species compared to elemental Te, preventing the bonded Te from stripping cathodically. Thus, the Te stripping current that is observed is thought to be due to excess elemental Te in the deposit. Four anodic peaks are observed, three of which correspond to a reduction in deposit mass. These are assigned to stripping of elemental Sb at -0.06 V, stripping of SbTe at 0.45 V, and stripping of elemental Te at 0.53 V. The peak at 0.88 V is believed to correspond to the oxidation of Au and is briefly discussed at the end of this section. Broadening of the Sb stripping peak in the binary solution is observed in agreement with results from Leimküler et al.<sup>7</sup> The shift in stripping potential of the compound relative to the elemental phases is a result of a large free energy of Sb<sub>2</sub>Te<sub>3</sub> formation ( $\Delta G_f =$

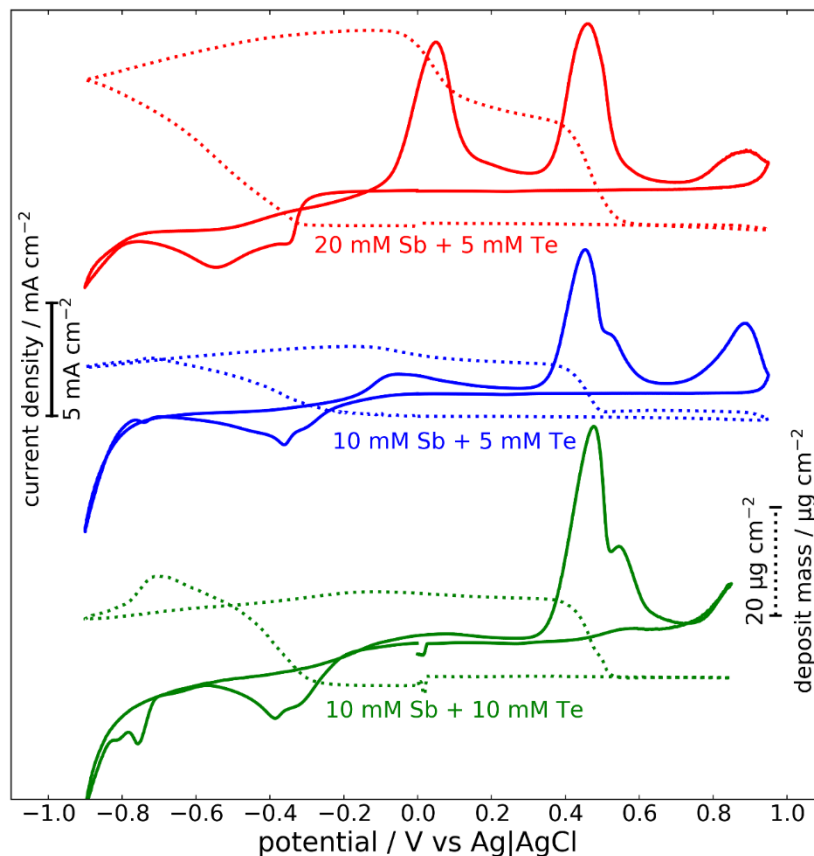


Figure 2-2. CVs and corresponding EQCM measurements of solutions containing both TeO<sub>2</sub> and SbCl<sub>3</sub> in various ratios. Scan rate 20 mV·s<sup>-1</sup>.

$-57.5 \text{ kJ}\cdot\text{mol}^{-1}$ ).<sup>7</sup> This peak assignment supposes that the deposit contains the compound phase in conjunction with elemental Sb and Te phases. To confirm peak assignments, CVs were performed on solutions containing various concentration ratios of Sb(III):Te(IV), namely 4:1, 2:1, and 1:1. Results presented in Figure 2–2 largely support the hypothesis. The solution containing the highest Sb ratio exhibits a much larger peak due to stripping of bulk Sb, and the shoulder attributed to excess Te stripping is eliminated, indicating that such a high Sb content eliminates free Te atoms in deposit. Additionally, the EQCM reveals that no Te is cathodically stripped on the negative side of the CV, further indicating bulk Te does not form. On the other hand, the highest Te:Sb ratio in solution results in a more pronounced anodic peak at 0.54 V and an enhanced cathodic stripping peak at -0.75 V, both of which indicate that bulk Te is easily formed from this solution. The anodic peak assigned to stripping of Sb is nearly eliminated in this case. In no cases are either the peak at 0.45 V, assigned to compound stripping, or the peak at 0.88 V for substrate oxidation, eliminated.

The anodic peak at +0.88 V seen throughout Figures 2–1 and 2–2 is caused by oxidation of the gold substrate in the presence of adsorbed chloride to form  $[\text{AuCl}_2]^-$ , which can further react to form soluble  $\text{AuCl}_4^-$ . This reaction is well known in chloride containing solutions, and the potential of this peak, 0.88 V, is in close agreement with that found by Gallego et al for this reaction in the presence of 30 mM  $\text{Cl}^-$ .<sup>26</sup> This assignment is further supported by the dependence of this peak on the presence of chloride. In the CV of the Te only bath in Figure 2–1, which contains no  $\text{Cl}^-$ , no peak is observed at this potential, however all CVs in baths containing chloride from Sb salt exhibit this peak. EQCM measurements reveal a slight reduction of mass at this point in the scan which reduces the

mass to less than the initial value, further indicating that the substrate itself is being oxidized to a soluble species.

### Chronoamperometry studies

Chronoamperometry was employed here to study the nucleation and growth behavior of SbTe deposits, in which the applied potential is stepped from open-circuit to a potential where deposition occurs. This was performed in solutions containing only 5 mM Te(IV), only 10 mM Sb(III), and both 5 mM Te(IV) and 10 mM Sb(III). In every case at each potential step tested, an initial capacitive current spike quickly decays, likely due to a combination of double layer charging, adsorption reaction, and 2-dimensional UPD nucleation. A nucleation peak is then observed which can be modelled with the Scharifker-Mostany Model for 3D nucleation and diffusion controlled growth.<sup>27</sup> The current transients for the three solutions are presented in Figure 2-3. To adequately model the current transients, a linear combination of a capacitive charging current,  $i_{cap}$ , and the Scharifker-Mostany nucleation and growth current,  $i_{3D}$ , is employed to model the overall current,  $i$ , as follows:<sup>28-29</sup>

$$i = i_{cap} + i_{3D}$$

$$i_{cap} = -k_{cap} \exp\left(-\frac{t}{\tau_{cap}}\right)$$

$$i_{3D} = zFD^{1/2}c(\pi t)^{-1/2} \left\{ 1 - \exp\left[-N_0\pi D(8\pi Mc/\rho)^{1/2}t\left(1 - \frac{1 - e^{-At}}{At}\right)\right]\right\}$$

The physical meanings of the symbols in this model are summarized in Table 2-1. The known parameters for Te are  $M = 127.6 \text{ g}\cdot\text{mol}^{-1}$ ,  $\rho = 6.23 \text{ g}\cdot\text{cm}^{-3}$ , and  $z = 4$ ; the known parameters for Sb are  $M = 121.8 \text{ g}\cdot\text{mol}^{-1}$ ,  $\rho = 6.68 \text{ g}\cdot\text{cm}^{-3}$ , and  $z = 3$ .<sup>30</sup> The five unknown parameters are  $k_{cap}$ ,  $\tau_{cap}$ ,  $D$ ,  $N_0$ , and  $A$ . These parameters were fitted to the experimental

current transients using a non-linear least squares method;<sup>31</sup> the resultant parameters are presented in Table 2–2, while the fitted data is presented in the Supplementary Information. This model was found to fit well with the experimental current transients obtained from Te and Sb + Te solution. Experiments in Sb solution in general exhibit a long incubation time before the onset of the nucleation peak, due to the difficulty of Sb nucleation on Au at low overpotentials. While this long incubation time prevents a successful fitting of the proposed model at these low overpotentials, the model fits well at sufficiently negative potential steps of -0.85 and -0.90 V. At lesser potentials, the proposed model does not fit experimental transients even if a time offset is applied to account for the

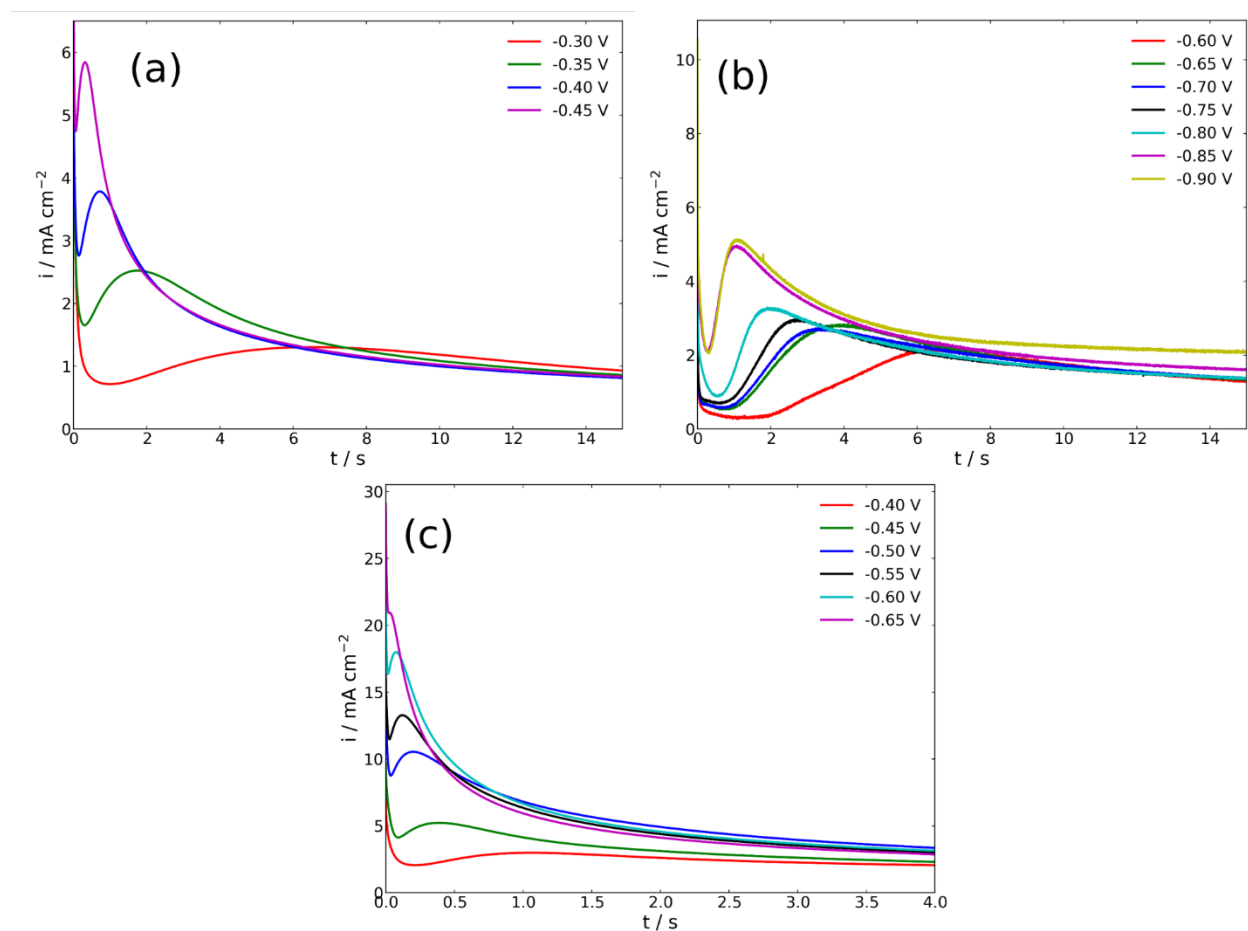


Figure 2–3. Experimental current transients for potential step experiments, where the potential was stepped from open-circuit to the indicated potential, in solutions containing (a) 5 mM Te(IV), (b) 10 mM Sb(III), and (c) 5 mM Te(IV) + 10 mM Sb(III).

incubation delay, likely due to electrode processes that are not adequately captured by the model. Therefore, fitted data are only presented for potential steps that did not exhibit long incubation times. For the Sb + Te solution,  $M$ ,  $\rho$ , and  $z$  were taken as the average values of the two components. Since the values of these parameters are very similar between Sb and Te, this method is not expected to result in significant error. The fitted model is plotted alongside the experimental current transients in the supplementary information.

The parameter  $k_{cap}$  corresponds to the initial current of the capacitance charging, therefore it is expected to monotonically increase as the overpotential of the step increases; this expectation is confirmed for the solutions of Te and SbTe. In addition, the total charge of capacitive current ( $k_{cap} * \tau_{cap}$ ) is found to be approximately constant regardless of the applied potential for the Te electrolyte, consistent with a surface area limited capacitive phenomenon. However, in the Sb solution, the incubation times prevent precise fitting of the model at short ( $t < 0.3$  s) times.

The diffusion coefficient,  $D$  should not depend on potential so long as the depositing species does not change, and this is confirmed to be the case for Te only and Sb only solutions. Furthermore, the diffusion coefficients obtained from curve fitting were similar for Te(IV) and Sb(III) species in the two electrolytes. However, in the multi-component solution, not only were the diffusion coefficients obtained therein much different from the ones from single element systems, but also a potential dependence of the coefficients was observed. The latter can be explained by a different ratio of ionic components being deposited at different potentials. The former demonstrates the difficulty in modelling a codepositing species with a model designed for a single depositing species. For instance, the Scharifker-Mostany model is based on a diffusion controlled nuclear growth behavior.

Table 2-1. Symbols and definitions for nucleation modelling equations

Symbol	Meaning
$A$	Nucleation rate per active site, $s^{-1}$
$c$	Concentration, $\text{mol}\cdot\text{cm}^{-3}$
$D$	Diffusion coefficient, $\text{cm}^2\cdot\text{s}^{-1}$
$F$	Faraday constant, $\text{C}\cdot\text{mol}^{-1}$
$i$	Current density, $\text{A}\cdot\text{cm}^{-2}$
$k_{cap}$	Capacitive current density constant, $\text{A}\cdot\text{cm}^{-2}$
$\tau_{cap}$	Capacitive charging time constant, s
$M$	Molar mass, $\text{g}\cdot\text{mol}^{-1}$
$N_0$	Number density of active sites, $\text{cm}^{-2}$
$t$	Time, s
$z$	Number of electrons transferred per atom reduced
$\rho$	Density, $\text{g}\cdot\text{cm}^{-3}$

Table 2-2. Fitted parameters for current transients

	Potential V	$k_{cap} * 10^3$ $\text{A}\cdot\text{cm}^{-2}$	$\tau_{cap} * 10^3$ s	$D * 10^6$ $\text{cm}^2\cdot\text{s}^{-1}$	A $\text{s}^{-1}$	$N_0 * 10^{-5}$ $\text{cm}^{-2}$
Te	-0.30	4.1	159	14	6.01	9.66
	-0.35	4.3	162	11	1.83	111
	-0.40	5.2	122	9.5	0.831	108
	-0.45	7.7	65.9	10.0	1.19	352
Sb	-0.85	5.0	142	12.9	0.00123	10400
	-0.90	6.1	127	14.2	0.00105	10400
Sb + Te	-0.40	5.2	84.0	7.77	12.4	9.74
	-0.45	9.0	46.1	8.79	25.4	25.0
	-0.50	12.5	21.0	22.5	450	14.2
	-0.55	16.7	14.3	19.6	301	30.2
	-0.60	21.4	21.8	22.2	62.8	49.4
	-0.65	29.6	16.1	17.9	92.1	93.5

While the deposition of Te is believed to be under diffusion control in the conditions used in alloy deposition, the deposition of Sb at those conditions is not necessarily limited by diffusion. Such a difference between elements may also contribute to the discrepancy in the diffusion coefficient. If the fitted values are considered as effective diffusion coefficients

specific to the codeposition conditions, then they are still of the appropriate order of magnitude.

The curve fitted values of  $A$  and  $N_0$  are listed in Table 2-2 for nucleation behavior comparison. For a typical cathodic nucleation process, the total number of nucleation sites available, given by  $N_0$ , is expected to increase with increasing cathodic potentials. In other words, more locations on the surface become active as more negative potential can overcome a higher activation barrier, this is seen to be the case for all three solutions. All fitting parameters fall within an appropriate order of magnitude for their respective expected values, taken from similar studies of metal nucleation on foreign substrates,<sup>29, 31</sup> demonstrating the robustness of the fitting process. The suitability of this model for the experimental current transients is confirmed due to the aforementioned behavior of the fitting parameters.

Nucleation behavior is often characterized as either progressive or instantaneous. The former describes a large number of nucleation sites and a slow nucleation rate, leading to new nuclei being continuously formed during deposition. The latter results from a small number of nucleation sites with a fast nucleation rate, leading to nuclei that all form immediately upon the potential step. Scharifker and Mostany suggested a dimensionless parameter,  $\alpha$ , given as

$$\alpha = \frac{N_0 \pi D}{A} \left( \frac{8 \pi c M}{\rho} \right)^{1/2}$$

to characterize nucleation behavior as either instantaneous ( $\alpha \rightarrow 0$ ) or progressive ( $\alpha \rightarrow \infty$ ).<sup>27</sup> Calculated  $\alpha$  values for the experimental current transients are given in Table 2-3.

The  $\alpha$  values for Sb at highly negative potentials are beyond  $10^6$ , while they increase from

Table 2–3. Calculated  $\alpha$  values for current transients

	Potential V	$\alpha$
Te	-0.3	0.037
	-0.35	1.08
	-0.4	19.5
	-0.45	47.0
Sb	-0.85	2.32*10 <sup>6</sup>
	-0.9	2.98*10 <sup>6</sup>
Sb + Te	-0.4	0.115
	-0.45	0.165
	-0.5	0.0134
	-0.55	0.0372
	-0.6	0.331
	-0.65	0.344

less than 0.1 to 47 for the case of Te at different potentials. While the cutoff value for  $\alpha$  between instantaneous and progressive nucleation is not well defined,<sup>31</sup> these values suggest that Te nucleation is expected to exhibit a transition from more instantaneous to more progressive behavior as the potential applied becomes more negative, primarily due to an increasing number of available nucleation sites. In addition, the Sb is expected to exhibit more progressive behavior than Te. Interestingly, the  $\alpha$  values in SbTe codeposition are consistently small, even smaller than elemental Te nucleation, suggesting more instantaneous behavior across the potentials studied. This can be explained as the instantaneous behavior of Te rapidly inducing deposition on the Au substrate, followed by compound growth, which proceeds more rapidly than pure Te due to the thermodynamic favorability of compound formation. As an alternative approach, many authors normalize experimental current transients to the time,  $t_m$ , and current,  $i_m$ , at the peak of the curve, plotting the results against normalized ideal progressive and instantaneous curves given by:<sup>27, 29, 32</sup>

$$\left(\frac{i}{i_m}\right)^2 = \frac{1.9542}{t/t_m} \left(1 - \exp\left[-1.2564\left(\frac{t}{t_m}\right)\right]\right)^2 \quad (\text{instantaneous})$$

$$\left(\frac{i}{i_m}\right)^2 = \frac{1.2254}{t/t_m} \left(1 - \exp\left[-2.3367\left(\frac{t}{t_m}\right)^2\right]\right)^2 \quad (\text{progressive})$$

We have taken a similar approach, plotting the normalized  $i_{3D}$  portion of the experimental transient, to compare to ideal progressive and instantaneous nucleation behaviors, in Figure 2-4. These plots visually confirm the conclusion that pure Te generally follows an instantaneous nucleation behavior, Sb exhibits progressive behavior, and SbTe codeposition behavior is heavily influenced by the behavior of Te.

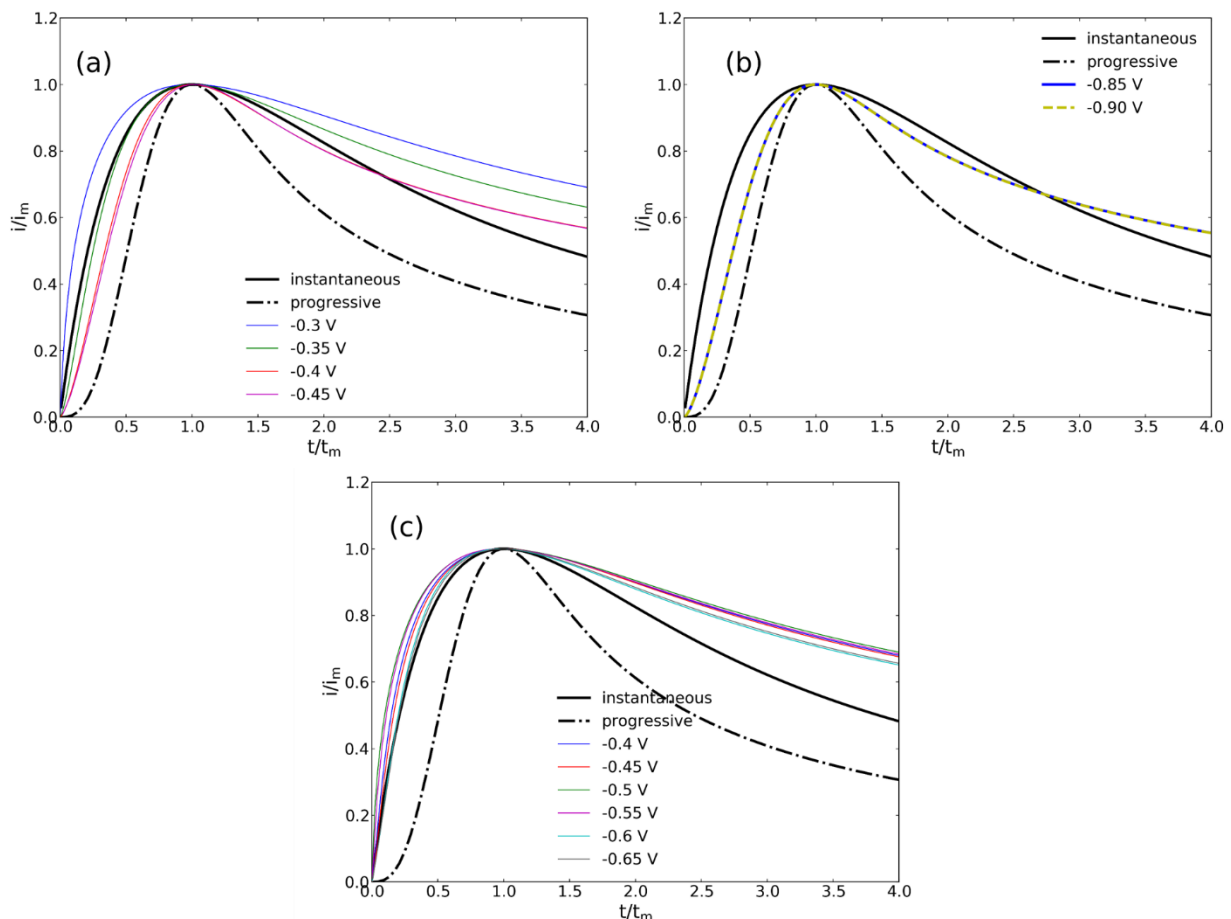


Figure 2-4.  $i_{3D}$  portion of current transients normalized to  $t_m$  and  $i_m$ , plotted against ideal normalized current transients for instantaneous and progressive nucleation and growth, for solutions containing (a) 5 mM Te(IV), (b) 10 mM Sb(III), and (c) 5 mM Te(IV) + 10 mM Sb(III).

## Nucleation site characterization

The composition of the growing nuclei has been observed directly in order to determine how interactions between the depositing elements affect film growth. Deposits were made from the solution containing 20 mM Sb(III) and 5 mM Te(IV) for short times (2-5 s) directly on TEM grids sputter coated with a layer of gold. The gold layer was sufficiently thick to achieve uniform nucleation yet thin enough for electron transparency. This allowed for STEM imaging and compositional analysis of the nucleation sites with good spatial resolution using an EDS line scan. Figure 2-5 shows the compositional variation across the diameter of typical nucleation sites obtained from depositions at -0.65 V and -0.45 V. EDS also confirmed that the grid membrane was coated with a uniform layer of Au, and that the Sb and Te deposit was constrained to the visible nucleation sites. The nuclei formed at -0.45 V showed more than 90% Te and a very limited amount of Sb, consistent with the fact that nucleation behavior was dominated by Te as observed in Figure 2-3. On the other hand, at a more negative potential of -0.65 V, the Sb content in nuclei increased to between 12 and 30 at%. More importantly, at both potentials, results

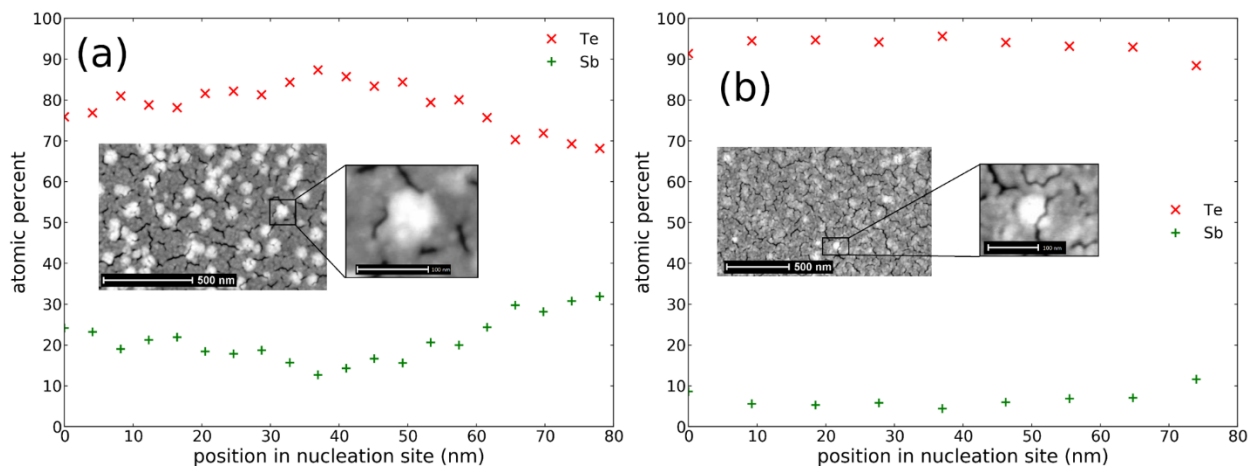


Figure 2-5. Composition variation along the diameter of a typical SbTe nucleation site obtained at a potential of (a) -0.65 V and (b) -0.45 V, insets show STEM micrographs of nucleation sites.

reveal a higher Sb content at the outskirts of the nucleation sites, and centers that are rich in Te. This difference is more pronounced for the case of -0.65 V. For a 3D island growth process, the initial nucleation is expected to occur in the center of each site, and outward hemispherical growth is expected from there. While the wettability of the deposited material on the substrate can impact the contact angle and alter the aspect ratio of the nuclei,<sup>17</sup> the outward growth direction is expected to remain the same. In this case, a Te rich center indicates the initial deposited species is Te, upon which the compound growth will occur.

### **Conclusion**

The growth of SbTe compound has been studied with voltammetric methods and is found to include the deposition of one or more SbTe phases simultaneously with elemental Sb or Te phases, depending on the concentration ratio of the depositing species in the electrodeposition bath. The free energy of formation of SbTe compounds thermodynamically stabilizes the compound phases with respect to the elemental phases. The binary compound deposition is found to fit an instantaneous 3D nucleation and growth model. This is a behavior that, while similar to that of individually depositing Te, is in direct contrast to individually depositing Sb. Since initial nucleation behavior of the compound resembles that of Te, this is likely the species which initially deposits at active nucleation sites, followed by compound growth over the initial Te deposit. The nucleation sites are found to be richer in Te at the center, further supporting that the compound nucleation process is initialized by Te.

## Acknowledgements

Research Grant Council (RGC) at the University of Alabama (UA) is acknowledged for support through Grant RG-14741. The authors would like to thank the Central Analytical Facility at University of Alabama for instrument access and training.

## References

1. DiSalvo, F. J., Thermoelectric Cooling and Power Generation. *Science* **1999**, *285* (5428), 703-706.
2. Romeo, N.; Bosio, A.; Tedeschi, R.; Romeo, A.; Canevari, V., A highly efficient and stable CdTe/CdS thin film solar cell. *Solar Energy Materials and Solar Cells* **1999**, *58* (2), 209-218.
3. van Pieterse, L.; Lankhorst, M. H. R.; van Schijndel, M.; Kuiper, A. E. T.; Roosen, J. H. J., Phase-change recording materials with a growth-dominated crystallization mechanism: A materials overview. *Journal of Applied Physics* **2005**, *97* (8), 083520.
4. Huang, Q.; Kellock, A. J.; Raoux, S., Electrodeposition of SbTe Phase-Change Alloys. *Journal of The Electrochemical Society* **2008**, *155* (2), D104-D109.
5. Jung, H.; Myung, N. V., Electrodeposition of antimony telluride thin films from acidic nitrate-tartrate baths. *Electrochimica Acta* **2011**, *56* (16), 5611-5615.
6. Venkatasamy, V.; Shao, I.; Huang, Q.; Stickney, J. L., ALD Approach toward Electrodeposition of Sb<sub>2</sub>Te<sub>3</sub> for Phase-Change Memory Applications. *Journal of The Electrochemical Society* **2008**, *155* (11), D693-D698.
7. Leimkühler, G.; Kerkamm, I.; Reineke-Koch, R., Electrodeposition of Antimony Telluride. *Journal of The Electrochemical Society* **2002**, *149* (10), C474-C478.
8. Liang, X.; Kim, Y.-G.; Gebergziabher, D. K.; Stickney, J. L., Aqueous Electrodeposition of Ge Monolayers. *Langmuir* **2010**, *26* (4), 2877-2884.
9. Lai, Y.; Liu, F.; Li, J.; Zhang, Z.; Liu, Y., Nucleation and growth of selenium electrodeposition onto tin oxide electrode. *Journal of Electroanalytical Chemistry* **2010**, *639* (1-2), 187-192.

10. Rashkova, B.; Guel, B.; Pötzschke, R. T.; Staikov, G.; Lorenz, W. J., Electrodeposition of Pb on n-Si(111). *Electrochimica Acta* **1998**, *43* (19), 3021-3028.
11. Mendoza-Huizar, L. H.; Robles, J.; Palomar-Pardavé, M., Nucleation and growth of cobalt onto different substrates: Part I. Underpotential deposition onto a gold electrode. *Journal of Electroanalytical Chemistry* **2002**, *521* (1), 95-106.
12. Fleischmann, M.; Thirsk, H. R., Electrochemical kinetics of formation of monolayers of solid phases. *Electrochimica Acta* **1964**, *9* (6), 757-771.
13. Vasilakopoulos, D.; Bouroushian, M.; Spyrellis, N., Electrocrystallisation of zinc from acidic sulphate baths; A nucleation and crystal growth process. *Electrochimica Acta* **2009**, *54* (9), 2509-2514.
14. Gunawardena, G. A.; Hills, G. J.; Montenegro, I., Potentiostatic studies of electrochemical nucleation. *Electrochimica Acta* **1978**, *23* (8), 693-697.
15. Soto, A. B.; Arce, E. M.; Palomar-Pardavé, M.; González, I., Electrochemical nucleation of cobalt onto glassy carbon electrode from ammonium chloride solutions. *Electrochimica Acta* **1996**, *41* (16), 2647-2655.
16. Gómez, H.; Henríquez, R.; Schrebler, R.; Córdova, R.; Ramírez, D.; Riveros, G.; Dalchiale, E. A., Electrodeposition of CdTe thin films onto n-Si(1 0 0): nucleation and growth mechanisms. *Electrochimica Acta* **2005**, *50* (6), 1299-1305.
17. Bauer, E.; Poppa, H., Recent advances in epitaxy. *Thin Solid Films* **1972**, *12* (1), 167-185.
18. Corcoran, S. G.; Chakarova, G. S.; Sieradzki, K., Stranski-Krastanov growth of Ag on Au(111) electrodes. *Physical Review Letters* **1993**, *71* (10), 1585-1588.
19. Nichols, R. J.; Schröer, D.; Meyer, H., An in situ scanning probe microscopy study of copper electrodeposition on conductive polypyrrole. *Electrochimica Acta* **1995**, *40* (10), 1479-1485.
20. Ikemiya, N.; Iwai, D.; Yamada, K.; Vidu, R.; Hara, S., Atomic structures and growth morphologies of electrodeposited Te film on Au(100) and Au(111) observed by in situ atomic force microscopy. *Surface Science* **1996**, *369* (1), 199-208.

21. Yang, J. Y.; Zhu, W.; Gao, X. H.; Bao, S. Q.; Fan, M.; Duan, X. K.; Hou, J., Formation and characterization of Sb<sub>2</sub>Te<sub>3</sub> nanofilms on Pt by electrochemical atomic layer epitaxy. *J. Phys. Chem. B* **2006**, *110* (10), 4599-4604.
22. Zhu, W.; Yang, J. Y.; Zhou, D. X.; Bao, S. Q.; Fan, X. A.; Duan, X. K., Electrochemical characterization of the underpotential deposition of tellurium on Au electrode. *Electrochimica Acta* **2007**, *52* (11), 3660-3666.
23. Sorenson, T. A.; Wayne Suggs, D.; Nandhakumar, I.; Stickney, J. L., Phase transitions in the electrodeposition of tellurium atomic layers on Au(100). *Journal of Electroanalytical Chemistry* **1999**, *467* (1-2), 270-281.
24. Sorenson, T. A.; Lister, T. E.; Huang, B. M.; Stickney, J. L., A Comparison of Atomic Layers Formed by Electrodeposition of Selenium and Tellurium Scanning Tunneling Microscopy Studies on Au(100) and Au(111). *Journal of The Electrochemical Society* **1999**, *146* (3), 1019-1027.
25. Sorenson, T. A.; Varazo, K.; Suggs, D. W.; Stickney, J. L., Formation of and phase transitions in electrodeposited tellurium atomic layers on Au(1 1 1). *Surface Science* **2001**, *470* (3), 197-214.
26. Gallego, J. H.; Castellano, C.; Calandra, A.; Arvia, A., The electrochemistry of gold in acid aqueous solutions containing chloride ions. *Journal of Electroanalytical Chemistry and Interfacial Electrochemistry* **1975**, *66* (3), 207-230.
27. Scharifker, B. R.; Mostany, J., Three-dimensional nucleation with diffusion controlled growth: Part I. Number density of active sites and nucleation rates per site. *Journal of Electroanalytical Chemistry and Interfacial Electrochemistry* **1984**, *177* (1), 13-23.
28. Palomar-Pardavé, M.; Miranda-Hernández, M.; González, I.; Batina, N., Detailed characterization of potentiostatic current transients with 2D-2D and 2D-3D nucleation transitions. *Surface Science* **1998**, *399* (1), 80-95.
29. Mendoza-Huizar, L. H.; Robles, J.; Palomar-Pardavé, M., Nucleation and growth of cobalt onto different substrates: Part II. The upd-opd transition onto a gold electrode. *Journal of Electroanalytical Chemistry* **2003**, *545*, 39-45.
30. Haynes, W. M., *CRC handbook of chemistry and physics*. CRC press: 2014.

31. Heerman, L.; Tarallo, A., Theory of the chronoamperometric transient for electrochemical nucleation with diffusion-controlled growth. *Journal of Electroanalytical Chemistry* **1999**, *470* (1), 70-76.
  
32. Abbott, A. P.; El Ttaib, K.; Frisch, G.; McKenzie, K. J.; Ryder, K. S., Electrodeposition of copper composites from deep eutectic solvents based on choline chloride. *Physical Chemistry Chemical Physics* **2009**, *11* (21), 4269-4277.

## Supplementary Information

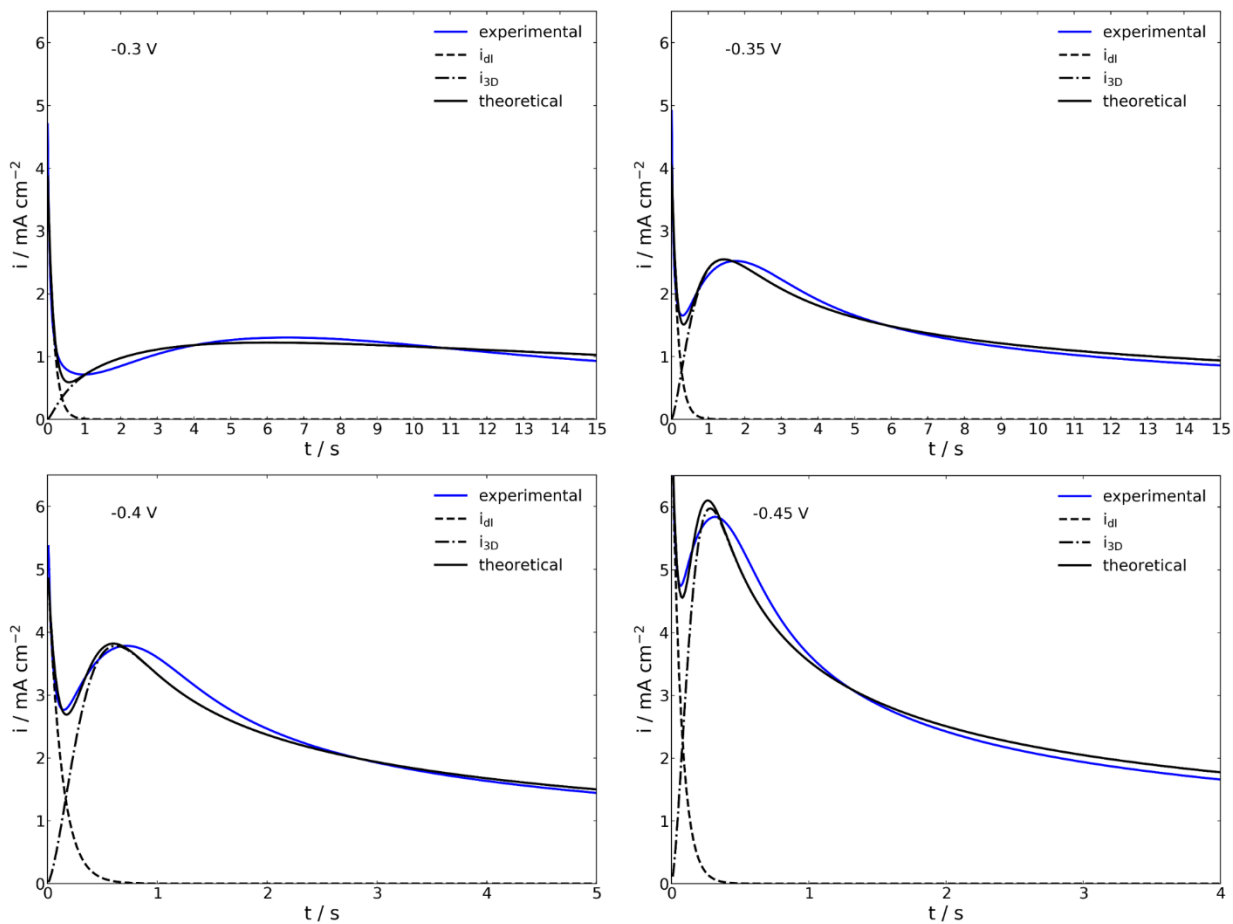


Figure S 2-1. Experimental current transients plotted against the fitted model for Te deposition.

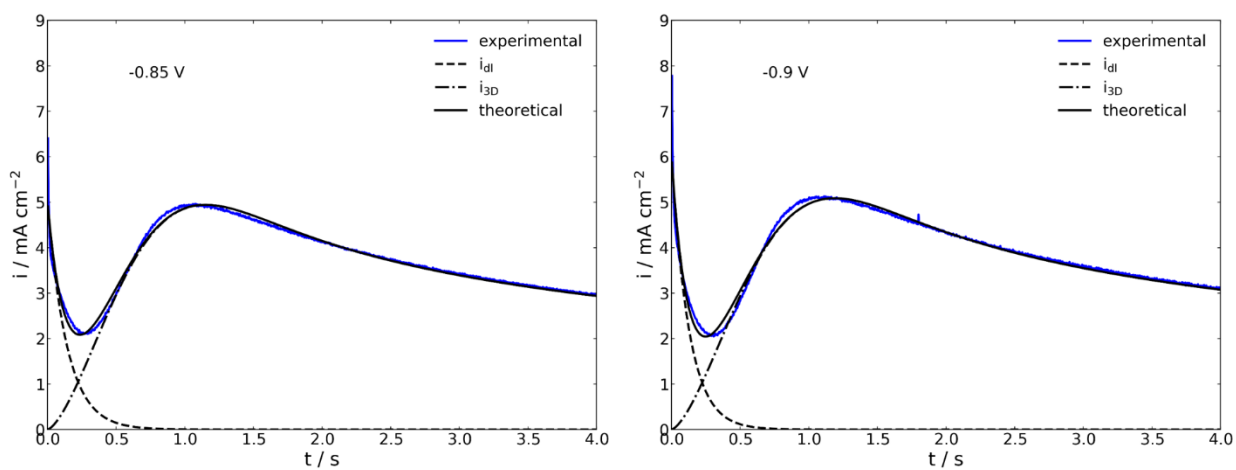


Figure S 2-2. Experimental current transients plotted against the fitted model for Sb deposition.

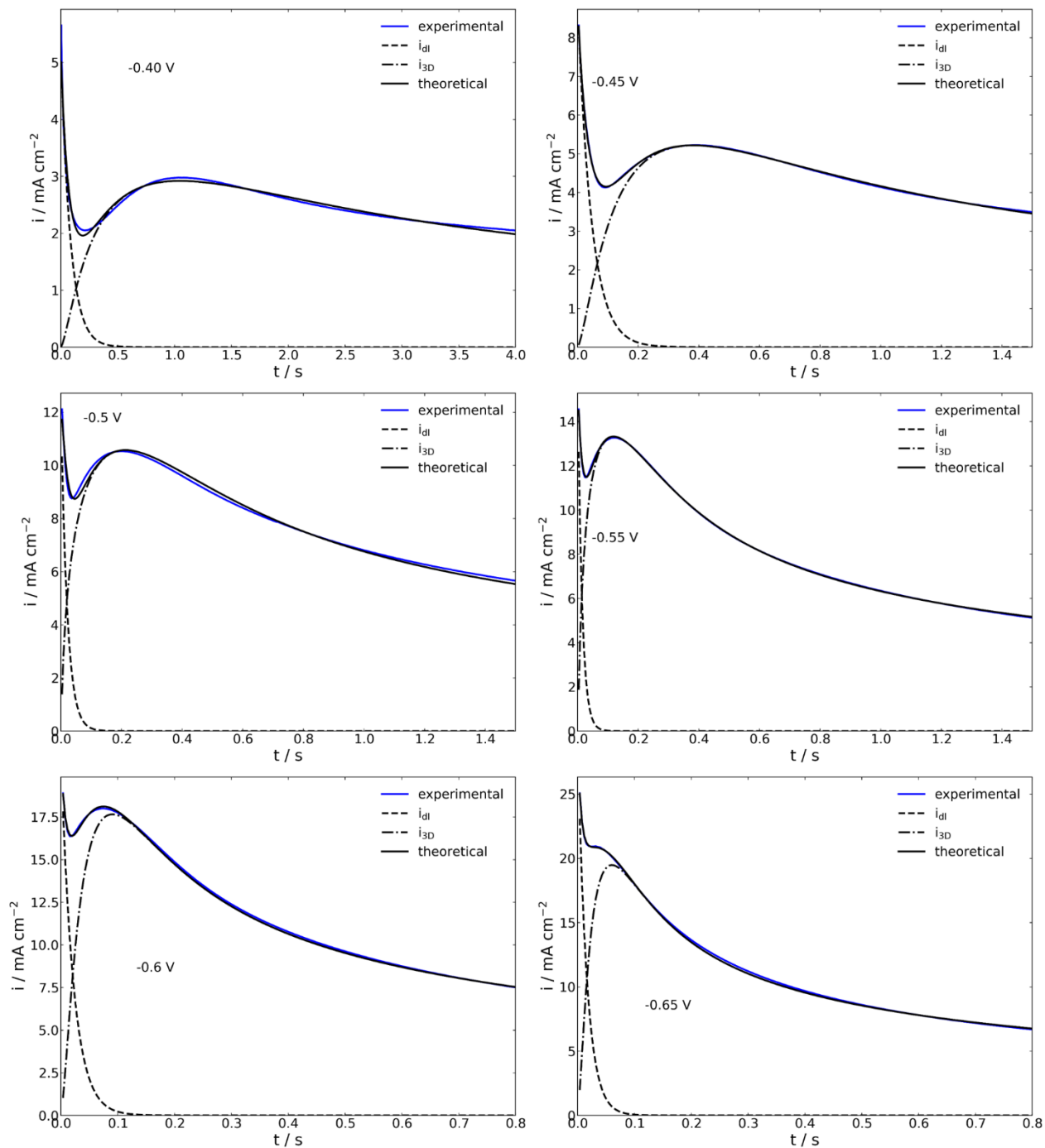


Figure S 2-3. Experimental current transients plotted against the fitted model for Sb-Te codeposition.

## CHAPTER 3. ELECTRODEPOSITION OF MANGANESE THIN FILMS ON A ROTATING DISK ELECTRODE FROM CHOLINE CHLORIDE/UREA BASED IONIC LIQUIDS\*

### Summary

The electrodeposition behavior of manganese from the choline chloride/urea based deep eutectic solvent is studied on a rotating disk electrode. Additionally, the effect of the organic additive glycine is analyzed, and the characteristics of deposited Mn films are examined. It is determined that Mn deposition will occur in this solvent at potentials below -1.2 V (vs. Ag), and is accompanied by one or more side reactions. Glycine is found to inhibit the deposition of Mn. In addition to an analysis of the potential dependent deposition behavior, this report studies the morphology of galvanostatic manganese deposits to determine the effect of the rate of Mn deposition.

### Introduction

Films of manganese and its alloys are widely used for a variety of applications including corrosion resistance, magnetic materials, and semiconductors. For example, manganese and zinc-manganese alloys have been demonstrated to show significantly enhanced corrosion resistance,<sup>1-2</sup> and manganese telluride has been investigated as a thermoelectric material as well as used for dilute magnetic semiconductors.<sup>3</sup> Whereas there has been significant interest to use electrodeposition to fabricate films of manganese containing alloys, the use of this technique has been limited for these films due to the

---

\* This chapter was published in *Electrochimica Acta*, 266, W.D. Sides, Q. Huang. Copyright Elsevier (2018).

highly cathodic potential required to deposit manganese.<sup>2</sup> In aqueous deposition systems, operating in this potential range presents numerous problems, namely low current efficiencies due to simultaneous reduction of water, as well as significant cracking and poor quality films resulting from hydrogen bubbles being produced on substrates.<sup>4</sup> These problems become worse when higher Mn content of alloys is required, generally limiting the incorporation of Mn into alloys to a low atomic percent. Additionally, oxidation of the manganese film cannot be easily avoided when depositing from aqueous systems.<sup>5</sup>

Non-aqueous solvents have been used to enable deposition of materials facing these problems, however these solvents are typically difficult to work with, highly corrosive,<sup>6</sup> prohibitively expensive, or unstable in atmospheric oxygen or moisture.<sup>7-9</sup> Recently, choline chloride (ChCl) based deep eutectic solvents (DES) have emerged as a promising deposition bath with the advantages of being inexpensive and non-toxic, having a wide potential window where deposition is possible without significant side reactions, and avoiding hydrogen evolution. Additionally, these baths are often stable at high temperatures (>100 °C). The kinetics of deposition reactions are greatly affected by temperature, and often have a marked effect on film morphology, thus the ability to deposit over a wide range of temperatures can be used to better control the surface characteristics of deposits.<sup>6</sup> ChCl based DES exhibit high conductivity, a good ability to dissolve metal salts, a relatively low viscosity compared to previous generations of ionic liquids, and stability in oxygen and moisture.<sup>10-11</sup> Several metal and alloy films have been successfully deposited from choline chloride based ionic liquids, including Cu,<sup>12</sup> Fe,<sup>13</sup> Ni,<sup>14</sup> Mn,<sup>15</sup> Zn-Mn,<sup>1</sup> Ni-Mn,<sup>4</sup> Zn-Sn,<sup>16</sup> Ni-Zn,<sup>17</sup> and Ni-Co.<sup>18</sup> Many of these films have been shown to have vastly superior characteristics, such as corrosion resistance, to films of the same material deposited from

aqueous baths, due to the avoidance of hydrogen evolution and other advantages afforded by these DES. While there have been some preliminary studies in literature on the deposition of metallic Mn and its alloys from choline chloride based ionic liquids,<sup>15</sup> there are no in-depth studies focusing on the deposition behavior or characteristics of Mn films obtained from these ionic liquids.

It is the goal of this chapter to present a good understanding of the deposition behavior of metallic Mn from the ionic liquid formed of a 2:1 molar mixture of urea and choline chloride (ChCl-U). The rotating disk electrode provides a convenient method to control the mass transport properties of a deposition system, which is critical in this solvent due to its relatively high viscosity. Rotation of the electrode provides a fresh supply of reactants at a well-defined rate, enabling approximations of steady state behavior to be made. Cyclic voltammetry (CV) under rotating conditions forms the basis of the understanding of the electrode reactions taking place. Deposition reactions are then studied with chronoamperometry and the morphology and crystallinity of Mn deposits are characterized. Additionally, the effect of glycine, which has been previously used as an additive in similar electrochemical systems,<sup>4</sup> on the behavior of manganese deposition is studied. Additives are widely used to alter the deposition potential of metals to reduce the difference in deposition potentials in an alloy deposition system. Since manganese has a large negative deposition potential relative to many of the metals it is commonly alloyed with, such as Zn and Ni, methods to reduce this potential difference are of interest.

## **Experimental**

Choline chloride (Acros Organics, 99%) was dried under vacuum for 2 days at 60 °C. Urea (Acros Organics, 99%) was dried for 2 days at 80 °C in air. Components were

combined in a 1:2 molar ratio at 70 °C and mixed until a clear, colorless liquid was formed. Solvent was then transferred into a nitrogen filled glove box where all solution preparation and electrochemical work were performed.  $\text{MnCl}_2 \cdot 4\text{H}_2\text{O}$  (Acros Organics, 99%) and glycine (Acros Organics, 98%) were used as received, and dissolved into the solvent in appropriate quantities at 80 °C. All electrochemical experiments were performed at 80 °C. The density of the solvent is reported to be  $1.164 \text{ g} \cdot \text{mL}^{-1}$  at 80 °C,<sup>19</sup> giving rise to choline chloride and urea concentrations of 4.5 and 9.0 M, respectively. The water added through the addition of hydrated metal salts was not removed, as dehydrating the salt was found to decrease its solubility. Moreover, it has been reported that small quantities of water do not interfere with, and may even enhance, metal deposition from  $\text{ChCl-U}$ .<sup>20-21</sup>

An Autolab PG320N potentiostat/galvanostat with a frequency analyzer was used for the electrochemical studies. The electrochemical cell was a 250 mL, three-neck, borosilicate round bottom flask, cleaned with aqua regia, acetone, DI water, and air dried before use. It consisted of an Ag wire quasi reference electrode and a Pt sheet counter electrode. All potentials referred to in this chapter are referenced against Ag. The working electrode was a Pt rotating disk electrode (RDE) of 5 mm diameter for all experiments except for those deposits analyzed with SEM and XRD, in which case a Cu RDE of the same size was used. The Pt RDE was polished to a mirror finish using successively smaller grits of alumina slurry, rinsed, and sonicated for 10 minutes in DI water. Prior to each experiment, it was cleaned in  $\text{HNO}_3$ , rinsed with DI water, acetone, more DI water, and air dried. Cu RDEs were polished to a mirror finish using diamond pastes with successively smaller grits down to  $0.25 \mu\text{m}$ , rinsed and sonicated for 10 minutes in DI water, and air dried prior to use. A Pine Research MSR rotator, shaft, and Pt disk insert were used, and Cu

disk inserts were cut in-house from a 99.99% copper rod. The position of electrodes within the bath was fixed between experiments, and solution resistance was measured using electrochemical impedance spectroscopy (EIS).

Samples were removed from the glove box for analytical measurements. Deposit thickness was determined using x-ray fluorescence (XRF) on a Bruker M1 Mistral. Samples requiring XRF measurements were promptly removed from electrolyte after deposition, rinsed with DI water, and dried under airflow. Film morphology was analyzed using a JEOL 7000 FE scanning electron microscope (SEM) equipped with an energy dispersive x-ray spectrometer (EDS). Viscosity measurements were taken with a ViscoLab 3000 viscometer. X-ray diffraction measurements were collected on a Bruker D8 Discover with Co K $\alpha$  source (1.79 Å).

## **Results and Discussion**

### **Characteristics of solvent**

CV studies were first performed on the ChCl-U without additional salts to determine the cathodic limit of the potential window of the solvent, and to characterize the reactions taking place. Figure 3–1 shows a CV curve of the solvent on a disk rotating at 1000 RPM. A slow scan rate of 5 mV·s<sup>-1</sup> was used to approximate a steady state polarization curve. Two reactions are seen to take place. A reaction beginning at -0.35 V has been suggested to be a reaction of non-complexed urea in solution.<sup>22</sup> A second reaction onset is seen at -0.85 V, which has been reported to be the bulk breakdown of the choline ion to form trimethyl amine gas.<sup>22</sup> This assignment is supported by the observation of bubble formation on the electrode near the cathodic limit of these CV scans, as well as a pungent, fishy odor within the glove box after prolonged electrochemical work. It has been reported that both

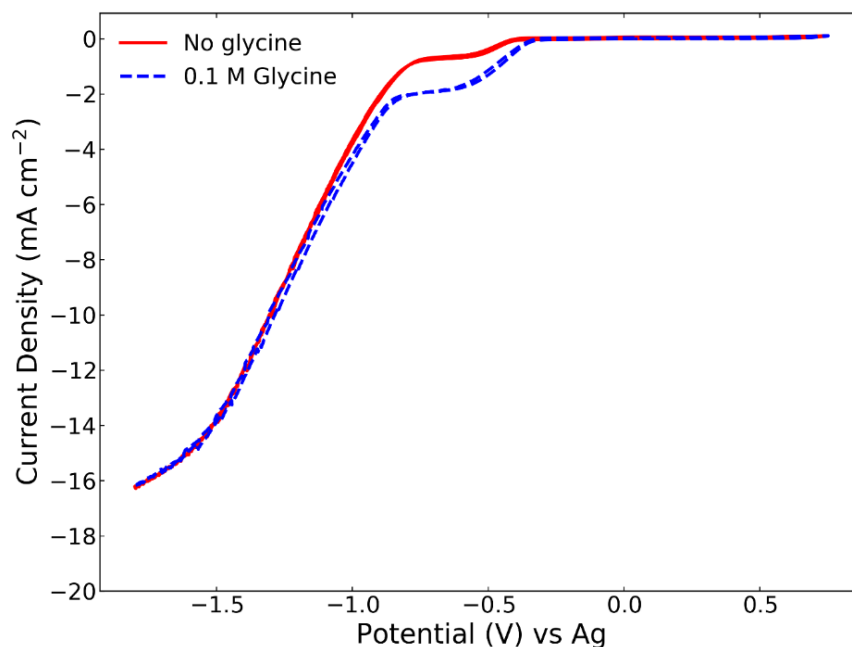


Figure 3–1. Cyclic voltammogram of ChCl-U on a Pt RDE rotating at 1000 RPM with a scan rate of  $5 \text{ mV}\cdot\text{s}^{-1}$ .

cathodic reactions are catalyzed by Pt electrodes, as the onset of these reactions is pushed to more negative potentials with the use of more inert electrode materials such as glassy carbon.<sup>22</sup> A CV scan was performed on the solvent using a Mn coated RDE. Results (seen in Figure S 3–1 of Supplementary Information) do indicate that both cathodic reactions are suppressed when Mn is used as the cathode as opposed to Pt.

The addition of 0.1 M glycine is marked by a large increase in the rate of the first reaction, but no change in the rate of the second reaction. Glycine and urea both act as a hydrogen bond donor (HBD) to the chloride ion, therefore the glycine could compete with urea in complexing with chloride, increasing the concentration of non-complexed urea available to participate in the first reaction. To confirm non-complexed urea as the active species in the first reaction (at  $-0.35 \text{ V}$ ), the limiting current was used, along with viscosity measurements described later in this section, to calculate the diffusion coefficient of the

active species. The limiting current at a rotating disk electrode can be related to the mass transfer parameters of the active species by

$$i_{lim} = 0.62zFD^{2/3}\omega^{1/2}\nu^{-1/6}C_0$$

where  $i_{lim}$  is the limiting current density,  $z$  is the number of electrons transferred per reactant molecule,  $F$  is Faraday's constant,  $D$  is the diffusion coefficient of the active species,  $\omega$  is the rotation rate of the RDE in  $\text{rad}\cdot\text{s}^{-1}$ ,  $\nu$  is the kinematic viscosity of the solution, and  $C_0$  is the concentration of the active species in the bulk of the solution.<sup>23</sup> From Figure 3-1,  $i_{lim}$  is determined to be  $-0.66$  and  $-1.93 \text{ mA}\cdot\text{cm}^{-2}$  before and after the addition of  $0.1 \text{ M}$  glycine, respectively. The kinematic viscosity is determined to be  $0.266 \text{ cm}^2\cdot\text{s}^{-1}$  as described later in this section. In order to find the concentration of non-complexed urea, an assumption is made that glycine competes with urea as the HBD for chloride ions, thus any added glycine increases the concentration of non-complexed urea in a 1:1 mole ratio. Since  $i_{lim}$  is directly proportional to  $C_0$ , the change in limiting current seen upon addition of  $0.1 \text{ M}$  glycine ( $1.27 \text{ mA}\cdot\text{cm}^{-2}$ ) is attributed to  $0.1 \text{ M}$  of non-complexed urea. The limiting current seen with no glycine therefore corresponds to  $C_0$  of  $0.052 \text{ M}$ . The diffusion coefficient can then be extracted, yielding  $D = 6.83 * 10^{-8} \text{ cm}^2\cdot\text{s}^{-1}$ . As a comparison, D'Agostino *et al.* have determined the diffusion coefficients of urea in this solvent at lower temperatures.<sup>24</sup> Their data was seen to fit well with an Arrhenius rate law:

$$D(T) = D_0 \exp\left(-\frac{E_A}{RT}\right)$$

where  $D_0 = 5.23 \text{ cm}^2\cdot\text{s}^{-1}$  and  $E_A = 45.0 \text{ kJ}\cdot\text{mol}^{-1}$  for urea diffusion in ChCl-U,  $R$  is the gas constant, and  $T$  is the temperature. This gives a diffusion coefficient of  $1.15 * 10^{-6} \text{ cm}^2\cdot\text{s}^{-1}$ , or about 16 times larger than the result based on the limiting current of the first reaction in

Figure 3–1. This discrepancy suggests that the active species is likely not non-complexed urea in the solution, as previously thought. As a confirmation, a solution was made that contained 1.92 M excess urea. Similar CV studies were performed, and the change in the limiting current of this reaction was noted in Figure S 3–2 of Supplementary Information. The excess urea only increased the limiting current by  $0.14 \text{ mA}\cdot\text{cm}^{-2}$ , further indicating that the reaction at  $-0.35 \text{ V}$  is not due to non-complexed urea.

An alternative suggestion may be that this reaction is of small amounts of residual water in the solution. This scenario appears unlikely, however, as Du et al have determined that water reduction in this solvent system occurs at more positive potentials, near  $0 \text{ V}$  vs Ag.<sup>25</sup> Their results also indicate that the water content must be higher than 3 wt% before appreciable water reduction current is noticed in a CV. Additionally, the same report demonstrates that water is easily driven out of this solvent when kept at  $80 \text{ }^\circ\text{C}$ , even in a humid environment, making it unlikely that any of the solutions tested in this study, which were in a dry atmosphere at  $80 \text{ }^\circ\text{C}$ , contained significant water concentrations. More research is needed to identify this side reaction.

Although this deep eutectic solvent exhibits relatively high ionic conductivity, this property is highly dependent on the viscosity of DES, particularly since the charge carriers are larger ions.<sup>26</sup> As a result, many researchers work with this solvent at slightly elevated temperatures ( $40\text{--}90 \text{ }^\circ\text{C}$ ) to reduce viscosity. Figure 3–2 shows the measured viscosity and conductance of the pure solvent and solutions containing various concentrations of  $\text{MnCl}_2\cdot 4\text{H}_2\text{O}$ . Conductance was determined using the impedance measured between the Pt cathode and the Ag quasi reference electrode near the open circuit potential, under non-rotating conditions. The EIS spectra was modelled with the solution resistance in series

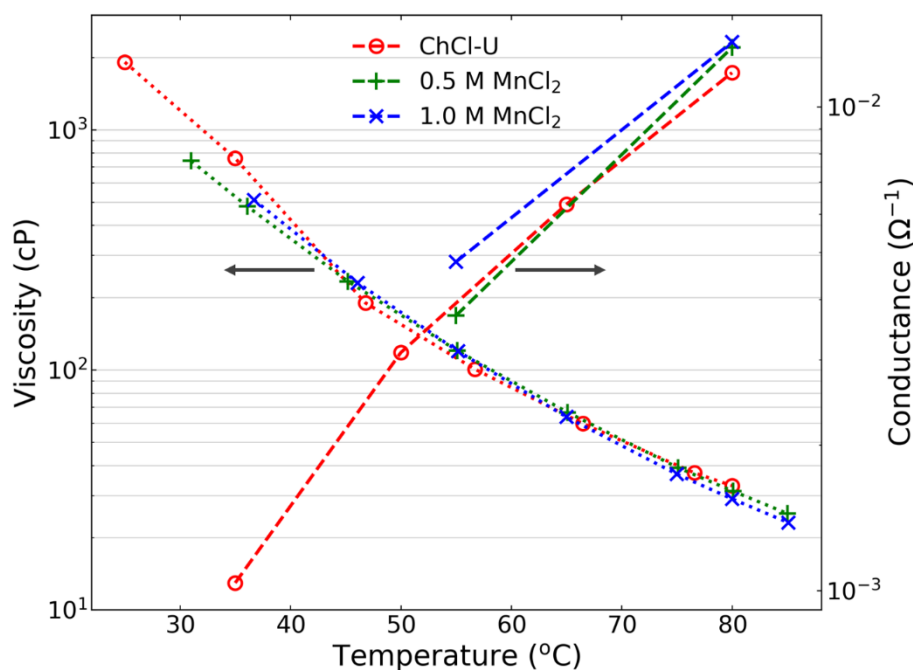


Figure 3-2. Viscosity and conductance of ChCl-U with varying amounts of dissolved  $\text{MnCl}_2 \cdot 4\text{H}_2\text{O}$ .

with a parallel combination of charge transfer resistance and double layer capacitance.

While the viscosity is highly sensitive to temperature in these ranges, it is not significantly affected by concentrations of salt in solution. Additionally, the small amount of water introduced with the hydrated metal salts did not have a marked effect of the viscosity, which increases exponentially from 30 cP to 700 cP as the temperature decreases from 80 °C to 35 °C. At the same time, the conductance drops from about 0.02 S to 0.001 S, consistent with the typical reciprocal relationship between conductivity and viscosity.

### Electrochemical behavior of manganese system

The addition of manganese to the system introduces a peak in the CV, as illustrated in Figure 3-3, for Mn(II) concentrations of 0.25 M, 0.50 M, and 0.75 M. The onset of this peak at -1.2 V is attributed to the deposition reaction  $\text{Mn(II)} \rightarrow \text{Mn}$  (more discussion later in this section). The peak current increases with additional Mn(II). It is seen that the bulk

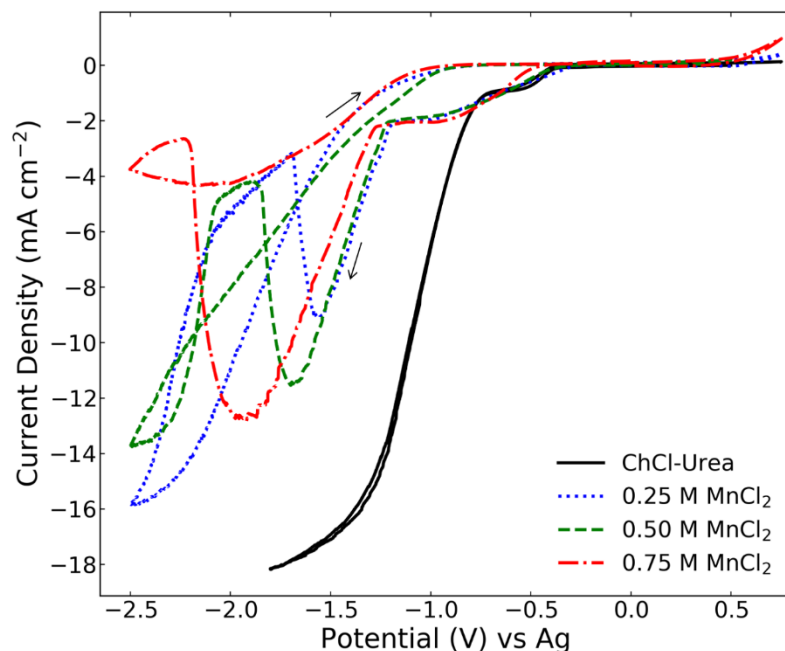


Figure 3–3. CV of ChCl-U containing various amounts of Mn(II) on a Pt RDE rotating at 1000 RPM with a scan rate of  $5 \text{ mV}\cdot\text{s}^{-1}$ .

solvent breakdown reaction observed as the second side reaction on Pt electrode in Figure 3–1 does not occur until the scan is more negative than -2 V, likely because the manganese film formed during the negative scan covers the Pt electrode, preventing it from catalyzing the decomposition. The significant peak shape was not expected in a CV while using a RDE at 1000 RPM. The use of slow scan rates and high rotation rates eliminates the transient mass transfer effects that are typically observed in stationary CV studies. Therefore, some other effect must be responsible for the decrease in current as the potential becomes more negative. Possible explanations could be a high resistivity in the growing manganese film, the formation of a passivating layer on the Mn film, or a competing side reaction that takes place at more negative potentials and is slower than the manganese reaction but significantly inhibits it. Deposits formed before the current peak are typically grey with metallic luster when examined before the peak (see Figure S 3–3 in Supplementary Information). Metallic manganese is expected to be highly conductive, and, more

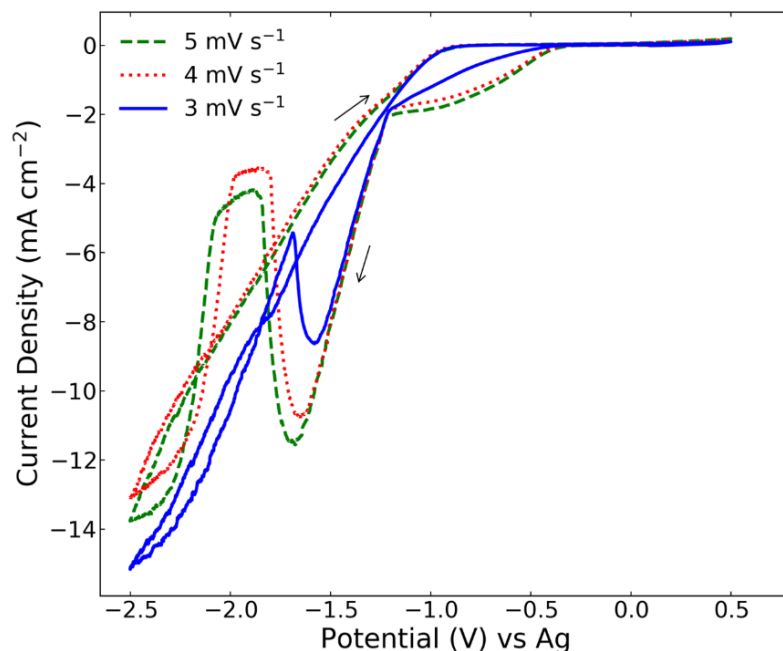


Figure 3–4. CV of ChCl-U containing 0.5 M Mn(II) on a Pt RDE rotating at 1000 RPM, taken at various scan rates.

importantly, film thickness is limited to around 300 nm. Therefore, film resistivity is unlikely to be the cause. To examine if the decrease in current is due to the potential, or deposit thickness, the scan rate was varied on a CV of the 0.5 M Mn(II) solution. As seen in Figure 3–4, the peak becomes narrower proportionally to the scan rate decrease. While the peaks at slower scan rates span a smaller potential range, they span a longer time, with 158 s, 150 s, and 128 s passing from the beginning to the end of the peak seen at  $3 \text{ mV}\cdot\text{s}^{-1}$ ,  $4 \text{ mV}\cdot\text{s}^{-1}$ , and  $5 \text{ mV}\cdot\text{s}^{-1}$ , respectively. These observations indicate the drop in current is not due to an effect of the potential, but that it is related either to the thickness of the deposit or the time of deposit growth, possibly allowing for the formation of a passivating layer.

Figure 3–5 shows an investigation into the nature of the peak by changing the cathodic limit of the CV and examining the changing shape of the reverse scan. The scan which reverses direction at -1.2 V, just before onset of Mn deposition, has a reverse scan that perfectly traces back the forward scan, indicating that no change in the electrode

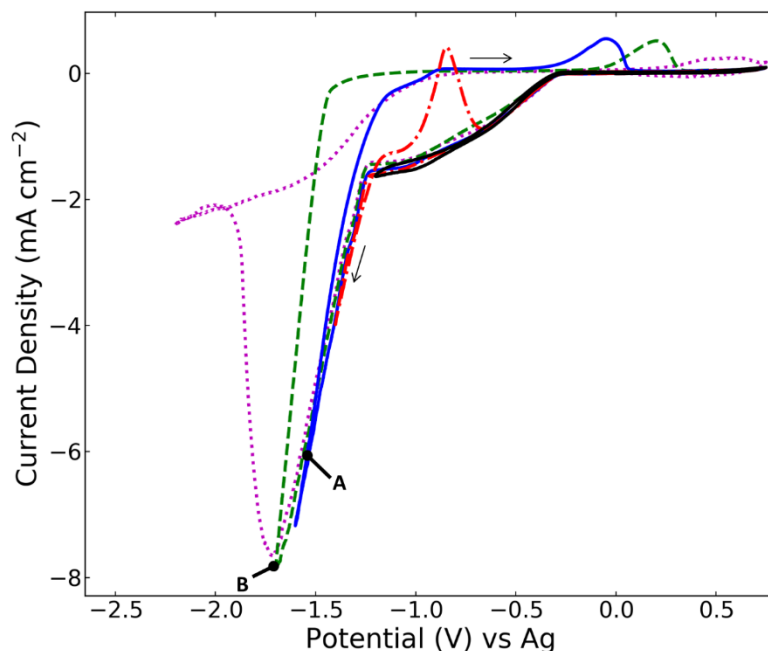


Figure 3-5. CV curves of ChCl-U containing 0.5 M Mn(II) on a Pt RDE rotating at 1000 RPM with a scan rate of  $5 \text{ mV}\cdot\text{s}^{-1}$ , scanning to different cathodic limits. No manganese film is observed once the reverse scan is complete.

surface has occurred before this point. This agrees with the assignment of that plateau to a side reaction which is catalyzed by Pt. The breakdown products remain in liquid phase and are flushed away by the RDE. The scan to  $-1.4 \text{ V}$  is accompanied by an anodic peak centered at  $-0.85 \text{ V}$  on the reverse scan, which is assigned to the dissolution of the manganese film. After this film dissolves, the background current returns to the same rate that is seen on the cathodic scan, indicating that the film has been completely removed, and that the electrode surface has been returned to Pt. Integrating the anodic current peak centered around  $-0.85 \text{ V}$  with the background current subtracted yields a charge of  $109.7 \text{ mC}\cdot\text{cm}^{-2}$ , which corresponds to  $43 \text{ nm}$  metallic Mn. On the other hand, the cathodic current measured in the Mn deposition region of this CV, between  $-1.22 \text{ V}$  and  $-1.40 \text{ V}$ , yields a total charge of  $122.4 \text{ mC}\cdot\text{cm}^{-2}$  when corrected for a background current of  $-1.6 \text{ mA}\cdot\text{cm}^{-2}$ . While the total cathodic charge is much higher due to the background side reaction, resulting in a

low current efficiency of 35%, the ratio between the deposition and stripping charges excluding the background reaches 90%. This suggests that the rise of the current in cathodic scan is due to the onset of Mn deposition, instead of the second side reaction observed on Pt surface in Figure 3–1. This is again consistent with the impeded bulk solvent break down observed on Mn electrode shown in Figure S 3–1 in Supplementary Information.

The remaining scans all exhibit a decrease in the rate of manganese deposition after reversal of the scan. Upon reversal of the scan to -1.6 V, the current does not deviate from that of the forward scan until it reaches -1.5 V (point **A**) at which point the current begins to decrease relative to the forward scan. Interestingly, it is noticed that point **A** occurs after the same period of time as would have been required for the current to begin to reduce if the scan had continued in the negative direction (point **B**). This evidence supports the explanation that there is a time dependent change in the film characteristics that inhibits the further deposition of Mn, such as a surface passivation that eventually grows to suppress Mn deposition. It seems to disagree with any explanation based on the thickness of the Mn deposit, because the deposit would not have grown to the same thickness at point **A** as it would have if the scan was continued to point **B**. In all scans past the cathodic peak, as the potential continues to be swept positively, the deposition current decreases to 0 and urea breakdown reaction is completely inhibited by the newly formed film on the electrode. The anodic peak associated with dissolution of the Mn film has been shifted significantly in the positive direction, and is significantly smaller than would be expected for a reversible process. In all cases, the Mn deposit had been completely removed, restoring the Pt surface by the end of the CV. Both effects become more pronounced as the

cathodic limit potential is decreased. The comparison between these CVs clearly suggests that a metallic and anodically removable Mn deposit was created during the CV down to -1.4 V and a permanent change of the Mn deposit occurred during the CVs beyond -1.7 V. In addition, this change seems to be a time dependent behavior. The permanently changed Mn not only suppresses the further deposition of Mn at a cathodic condition but also inhibits the anodic dissolution of itself. This is also consistent with the optical inspection of the films presented in Figure S 3–3 in Supplementary Information, where silver metallic films are formed before the current peak while brown and dull films are observed after the cathodic current decreases to form the current peak.

To better understand the growth rates of Mn, the thickness of the film was measured at several points along the cathodic scan. In each case, a fresh Pt RDE was swept negatively from an open circuit voltage to the desired potential, and the film thickness was measured by XRF. A Mn film density of  $7.44 \text{ g}\cdot\text{cm}^{-3}$  was used to determine film thicknesses from XRF spectra, although it should be noted that SEM observations (presented later) show non-compact film surfaces, which could lead to films that are thicker than determined here. While the film deposited at highly negative potentials could be non-metallic as discussed above, a metallic Mn profile was used in XRF analysis to ease the comparison between samples. Results in Figure 3–6 confirm the assignment of Mn deposition to the reaction with an onset at -1.2 V. Initial growth is consistent with the Butler-Volmer equation for a reduction reaction where the thickness of deposit exponentially increases. However, the Mn film growth comes to a halt as the current drops following the peak. After significantly more overpotential is applied, cathodic deposition resumes at about -2.25 V. No anodic stripping was observed in the reverse scan up to 0.5 V, consistent with the

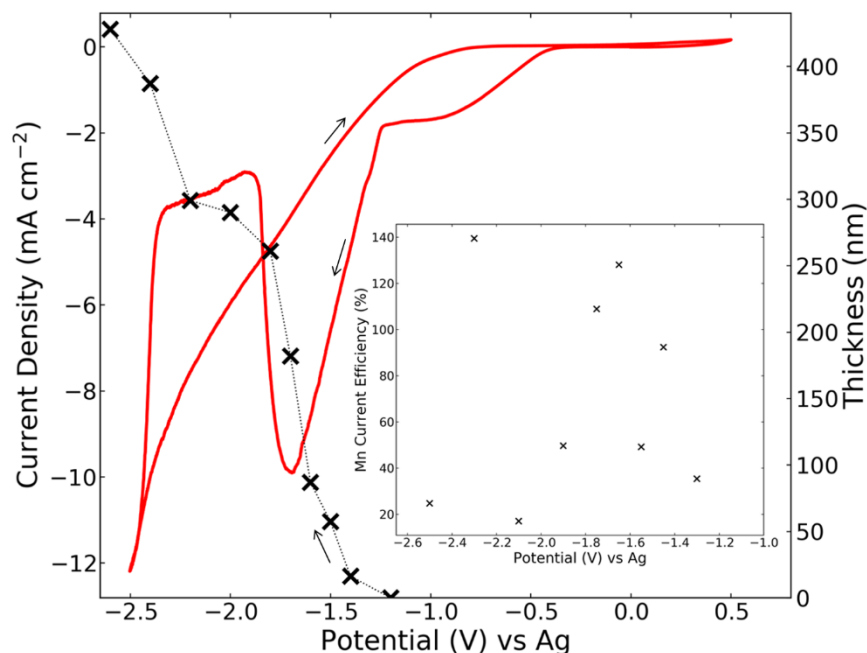


Figure 3-6. CV curve of ChCl-U containing 0.5 M Mn(II) on a Pt RDE rotating at 1000 RPM with a scan rate of  $5 \text{ mV}\cdot\text{s}^{-1}$  (red line), with XRF measurements of film thickness at various points along the negative sweep (black crosses). Thickness measurements were not acquired on the reverse (positive) scan. Inset: Average current efficiency between each pair of points, calculated using the derivatives of the measured film thicknesses.

anodic shift of the stripping peaks as the cathodic scans extend to more negative potentials in Figure 3-5. The average current efficiency between each pair of data points can be calculated with the Mn mass increase and corresponding cathodic charges. The inset in Figure 3-6 shows that the current efficiency reaches a maximum at around 1.7 V, where the passivation film discussed in CV studies began to form. The efficiency is very low at potentials more negative than -2.25 V, even though Mn deposition is resumed at these potentials, due to a significant side reaction. It is noted that efficiencies higher than 100% are sometimes obtained, particularly at highly negative potentials, due to the formation of Mn-containing passivation film and the non-uniform thickness of such films.

In order to deposit metallic Mn film, studies were undertaken to determine the potentiostatic deposition behavior of Mn at potentials before passivation occurs in the CV

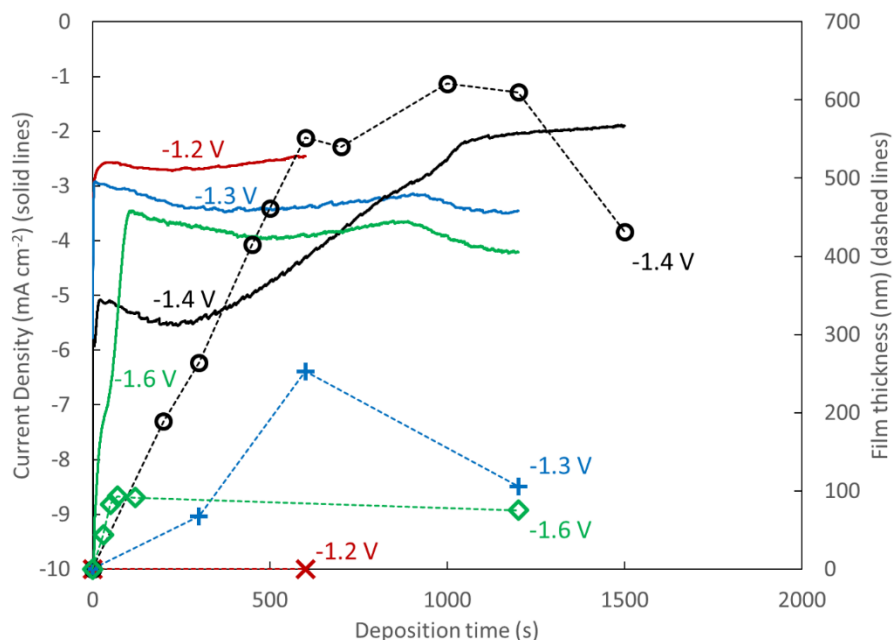


Figure 3-7. Chronoamperometry of manganese deposition at four applied potentials of a Pt RDE rotating at 1000 RPM from a 0.5 M Mn(II) solution, with film thicknesses measured at different stop times by XRF.

studies. Figure 3-7 shows the time evolution of current density on a Pt RDE rotating at 1000 RPM as well as film growth. At every potential where film growth is observed, it is seen that growth initially occurs in a linear fashion, however with time, the current density drops and film growth halts. The achievable thickness seems to be capped below 650 nm for all the conditions studied. In some cases, film thickness seems to even decrease after long deposition times; the cause of this is unknown. In any case, the initial rate of Mn growth increases with overpotential, however at the highest overpotential studied (-1.6 V) the growth halts rapidly and the film does not grow as thick. This indicates that in this potential region, a fast side reaction quickly passivates the Mn film and halts deposition.

### Effect of glycine

Glycine has been used in both aqueous<sup>27</sup> and deep eutectic solvents<sup>4</sup> as an additive to facilitate codeposition of metals for alloy deposition. Linear scan voltammetry at

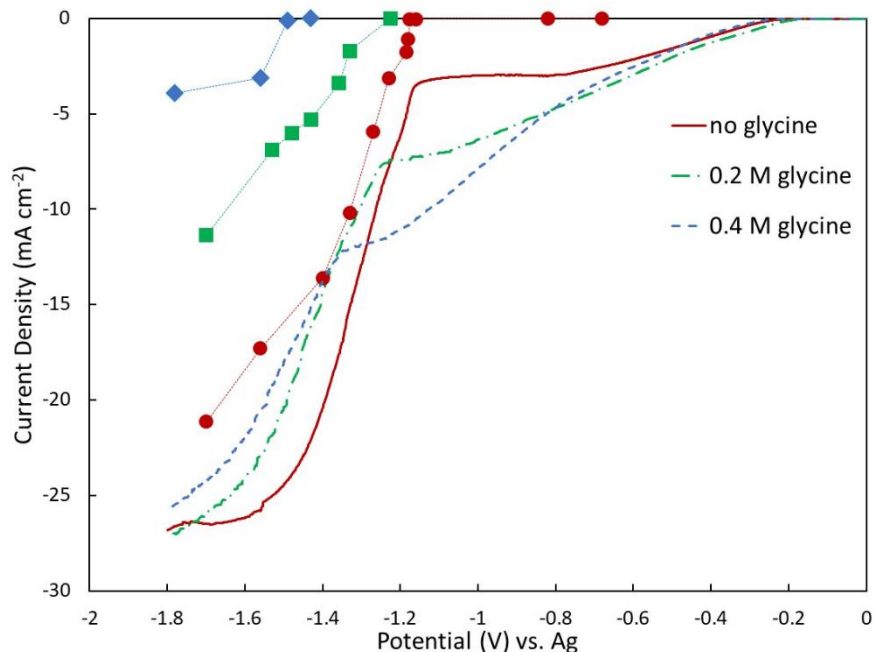


Figure 3–8. Partial currents (markers) of Mn deposition reaction from a 1.0 M Mn(II) solution. Films were deposited galvanostatically until  $1.5 \text{ C}\cdot\text{cm}^{-2}$  of charge had transferred and the measured thickness was used to calculate the amount of Mn deposited. Lines without markers show the negative scan of a  $5 \text{ mV}\cdot\text{s}^{-1}$  CV in the same solutions. All work was performed on a Pt RDE rotating at 1000 RPM.

1000 RPM was carried out to study the effect of glycine. Mn films were galvanostatically deposited and the partial current densities of Mn deposition were calculated from the film thickness. Figure 3–8 shows that the addition of glycine significantly enhances the rate of the first side reaction while inhibiting the deposition of Mn. It is seen that the onset potential for deposition is shifted more negative as glycine concentration increases. In addition, the Mn partial current and the current efficiency are greatly reduced. As observed in the blank solvent study, the addition of glycine greatly increases the rate of the side reaction beginning at  $-0.35 \text{ V}$ .

To determine whether the cause of Mn current inhibition is due to formation of a stable glycine-Mn chelate in solution, the concentration of free Mn(II) was calculated for each glycine-containing solution. Although the complexation of free Mn(II) is not well

known in ChCl-U, it is assumed to be unchanged by the addition of glycine, except that some of the Mn(II) forms the glycine-Mn chelate. Each solution was 1.0 M in MnCl<sub>2</sub>. The complexation between the carboxyl group in glycine with Mn(II) in aqueous system is extremely weak and the stability constant for the coordinated species between the amino group and Mn(II) is 2.8 as compared with the association constant of amino H<sup>+</sup>, 9.6.<sup>28</sup> Even if all the amino groups of glycine are available in ChCl-U system, the concentration of free Mn(II) in the 0.2 M and 0.4 M glycine solutions is still reduced only to 0.859 M and 0.731 M, respectively. However, in the same solutions, the Mn partial current is reduced by 40% and 80% respectively. In addition, such reduction was observed before a mass transport limit was reached, indicating that a mere reduction in availability of free Mn(II) cannot be the sole cause of partial current reduction. On the other hand, competition for active sites on electrode surface is commonly seen with organic additives, either by the organic molecule itself or by a metal cation species complexed with the organic molecule. Such adsorbed species can completely cover the surface and the inhibition effect saturates at a very low concentration. An increased inhibition effect is clearly seen in Figure 3–8, when the glycine concentration increases from 0.2 to 0.4 M, suggesting glycine itself is not the adsorbed inhibitor. Therefore, the inhibition of Mn deposition is likely caused by either an adsorbed Mn-glycine complex or an adsorbed intermediate created through a much faster side reaction. These conclusions need to be confirmed by further studies on the complexation of Mn(II) in ChCl-U and the effect of additives.

### **Characterization of manganese films**

The surface morphology of metallic lustrous Mn films deposited before the current peak was studied using a SEM. Figure 3–9 shows some representative films deposited for a

total charge of  $3 \text{ C}\cdot\text{cm}^{-2}$ , corresponding to a thickness of 415 nm at the current efficiency as low as 35%. Flake type of grains are observed for films deposited at  $-10$  and  $-15 \text{ mA}\cdot\text{cm}^{-2}$ , regardless of the addition of  $0.2 \text{ M}$  glycine, albeit a slightly larger grain size in presence of glycine. Higher current densities are seen to result in smaller grain size accompanied by a less adherent film that is cracked and appears raised from the substrate surface. Extremely high current densities result in films that sometimes fall from the substrate during rinsing. Depositions performed at or above  $20 \text{ mA}\cdot\text{cm}^{-2}$  from the solution without glycine were not adherent, even for very short deposition times. It is however possible to obtain adherent deposits at these higher current densities with the addition of  $0.2 \text{ M}$  glycine. Because the current efficiency in presence of glycine is much lower than in glycine free electrolyte, the loose films observed at high current density in absence of glycine are believed to relate to a

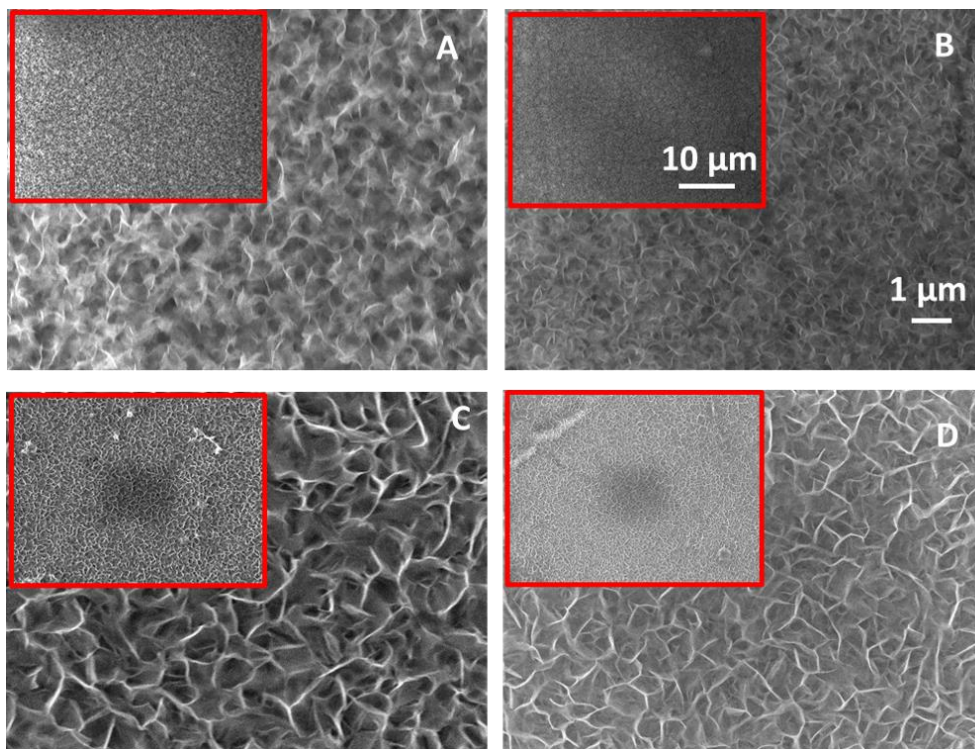


Figure 3-9. SEM images of the surface morphologies of deposits obtained galvanostatically at  $10.2 \text{ mA}\cdot\text{cm}^{-2}$  (A, C) or  $15.3 \text{ mA}\cdot\text{cm}^{-2}$  (B, D), with (C, D) and without (A, B)  $0.2 \text{ M}$  glycine. A total charge of  $3.0 \text{ C}\cdot\text{cm}^{-2}$  was passed in each case.

too high Mn deposition rate, too thick Mn film, or the formation of passivation film. EDS analysis of the deposits confirm the films in Figure 3–9 are primarily Mn, with impurities including chlorine and carbon (likely from the solvent) as well as oxygen (likely from the solvent as well as from oxidation of the Mn surface). X-ray diffraction measurements, however, did not show peaks associated with metallic manganese. Because these films were at least 400 nm thick, the absence of these peaks suggests the films are amorphous (spectra shown in Figure S 3–4 in Supplementary Information). Amorphous films deposited from organic solvent at high potentials are not uncommon and high temperature annealing are typically able to convert such amorphous films into a crystalline form.<sup>29</sup> However, due to the use of metal substrate in this study, annealing was not carried out to avoid inter-diffusion between Mn and electrode.

#### **Ag reference electrode**

The Ag wire reference electrode used in this study, while not a true reference electrode, was chosen due to its ubiquitous use in literature in similar ChCl-U systems, where no potential drift has been reported.<sup>16</sup> Nevertheless, it is worth mentioning that in the present study, the Ag reference seems to be suitable, as evidenced by numerous electrochemical tests. CVs were performed in several different batches of ChCl-U solvent, both before and after other electrochemical tests, and on subsequent days of solvent storage and use. In no instance was the onset potentials of the reactions significantly different from those observed in Figure 3–1. In addition, when the polarity of electrode switched from cathodic to anodic during CV studies, particularly for the CV down to -1.4 V in Figure 3–5, the current peak at -0.8 V was smooth and continuous, suggesting a

reversible redox reaction on Ag wire in ChCl-U system. It is therefore concluded that the Ag wire is a suitable and stable reference for ChCl-U based deposition systems.

## **Conclusion**

This chapter provides, for the first time, a comprehensive analysis of the reactions associated with the deposition of metallic manganese from ChCl-U. It is seen that Mn deposition will occur only below -1.2 V vs Ag. Contrary to previous reports,<sup>4</sup> all cathodic reactions at more positive potentials are side reactions. The Mn deposition reaction manifests as a large peak in the CV on the RDE, which is shown to be caused by a transient passivation of the growing deposit. While a Mn-containing passivation film formed upon the solvent breakdown is believed to cause the current decrease, the exact composition and nature of this film is yet to be determined. Manganese deposition can be resumed at low current efficiency by applying sufficiently negative potentials. The addition of glycine is seen to both inhibit the onset potential of Mn reaction and suppress the Mn partial current, leading to severely reduced current efficiency. The rate of Mn deposition is seen to affect the quality of the deposit, with too high of a rate leading to cracked or non-adherent films.

## **Acknowledgements**

National Science Foundation is acknowledged for the support through Grant CMMI-1662332. The authors would like to thank the University of Alabama Central Analytical Facility, College of Engineering Mechanical Shop, and Chemistry Glass Shop for their resources, as well as Sasha Zavgorodnya, Gabriela Gurau, and Robin D. Rodgers for their equipment and support with viscosity measurements.

## References

1. Fashu, S.; Gu, C. D.; Zhang, J. L.; Zheng, H.; Wang, X. L.; Tu, J. P., Electrodeposition, Morphology, Composition, and Corrosion Performance of Zn-Mn Coatings from a Deep Eutectic Solvent. *Journal of Materials Engineering and Performance* **2015**, *24* (1), 434-444.
2. Gong, J.; Zangari, G., Electrodeposition and Characterization of Manganese Coatings. *Journal of The Electrochemical Society* **2002**, *149* (4), C209-C217.
3. Yang, L.; Wang, Z. H.; Zhang, Z. D., Electrical properties of NiAs-type MnTe films with preferred crystallographic plane of (110). *Journal of Applied Physics* **2016**, *119* (4), 6.
4. Guo, J.; Guo, X.; Wang, S.; Zhang, Z.; Dong, J.; Peng, L.; Ding, W., Effects of glycine and current density on the mechanism of electrodeposition, composition and properties of Ni-Mn films prepared in ionic liquid. *Applied Surface Science* **2016**, *365*, 31-37.
5. Ganesan, S.; Prabhu, G.; Popov, B. N., Electrodeposition and characterization of Zn-Mn coatings for corrosion protection. *Surface and Coatings Technology* **2014**, *238*, 143-151.
6. Endres, F., Ionic Liquids: Solvents for the Electrodeposition of Metals and Semiconductors. *ChemPhysChem* **2002**, *3* (2), 144-154.
7. Shamsuri, A. A.; Abdullah, D. K., IONIC LIQUIDS: PREPARATIONS AND LIMITATIONS. *Makara Sains* **2010**, *14* (2), 101-106.
8. Endres, F.; Abbott, A. P.; MacFarlane, D. R., *Electrodeposition from Ionic Liquids*. Wiley-VCH: 2008.
9. Simka, W.; Puszczuk, D.; Nawrat, G., Electrodeposition of metals from non-aqueous solutions. *Electrochimica Acta* **2009**, *54* (23), 5307-5319.
10. Abbott, A. P.; Capper, G.; Davies, D. L.; Rasheed, R. K.; Tambyrajah, V., Novel solvent properties of choline chloride/urea mixtures. *Chemical Communications* **2003**, (1), 70-71.
11. Abbott, A. P.; Capper, G.; Davies, D. L.; McKenzie, K. J.; Obi, S. U., Solubility of metal oxides in deep eutectic solvents based on choline chloride. *J. Chem. Eng. Data* **2006**, *51* (4), 1280-1282.

12. Abbott, A. P.; El Ttaib K Fau - Frisch, G.; Frisch G Fau - McKenzie, K. J.; McKenzie Kj Fau - Ryder, K. S.; Ryder, K. S., Electrodeposition of copper composites from deep eutectic solvents based on choline chloride. **2009**, (1463-9076 (Print)).
13. Böck, R.; Wulf, S. E., Electrodeposition of iron films from an ionic liquid (ChCl/urea/FeCl<sub>3</sub> deep eutectic mixtures). *Transactions of the IMF* **2009**, *87* (1), 28-32.
14. Gu, C. D.; You, Y. H.; Yu, Y. L.; Qu, S. X.; Tu, J. P., Microstructure, nanoindentation, and electrochemical properties of the nanocrystalline nickel film electrodeposited from choline chloride–ethylene glycol. *Surface and Coatings Technology* **2011**, *205* (21), 4928-4933.
15. Bozzini, B.; Gianoncelli, A.; Kaulich, B.; Mele, C.; Prasciolu, M.; Kiskinova, M., Electrodeposition of manganese oxide from eutectic urea/choline chloride ionic liquid: An in situ study based on soft X-ray spectromicroscopy and visible reflectivity. *Journal of Power Sources* **2012**, *211*, 71-76.
16. Abbott, A. P.; Capper, G.; McKenzie, K. J.; Ryder, K. S., Electrodeposition of zinc–tin alloys from deep eutectic solvents based on choline chloride. *Journal of Electroanalytical Chemistry* **2007**, *599* (2), 288-294.
17. Yang, H. Y.; Guo, X. W.; Chen, X. B.; Wang, S. H.; Wu, G. H.; Ding, W. J.; Birbilis, N., On the electrodeposition of nickel–zinc alloys from a eutectic-based ionic liquid. *Electrochimica Acta* **2012**, *63*, 131-138.
18. You, Y. H.; Gu, C. D.; Wang, X. L.; Tu, J. P., Electrodeposition of Ni–Co alloys from a deep eutectic solvent. *Surface and Coatings Technology* **2012**, *206* (17), 3632-3638.
19. Yadav, A.; Pandey, S., Densities and Viscosities of (Choline Chloride + Urea) Deep Eutectic Solvent and Its Aqueous Mixtures in the Temperature Range 293.15 K to 363.15 K. *Journal of Chemical & Engineering Data* **2014**, *59* (7), 2221-2229.
20. Popescu, A.-M.; Constantin, V.; Cojocaru, A.; Olteanu, M., Electrochemical behaviour of copper (II) chloride in choline chloride-urea deep eutectic solvent. *Rev. Chim.(Bucharest)* **2011**, *62* (2), 206-211.
21. Haerens, K.; Matthijs, E.; Binnemans, K.; Van der Bruggen, B., Electrochemical decomposition of choline chloride based ionic liquid analogues. *Green Chem.* **2009**, *11* (9), 1357-1365.

22. Badea, M. L. M.; Cojocaru, A.; Anicai, L., ELECTRODE PROCESSES IN IONIC LIQUID SOLVENTS AS MIXTURES OF CHOLINE CHLORIDE WITH UREA, ETHYLENE GLYCOL OR MALONIC ACID. *UPB Sci. Bull. Series B* **2014**, 76, 21-32.
23. Levich, V. G., *Physicochemical hydrodynamics*. Englewood Cliffs, N.J., Prentice-Hall: 1962.
24. D'Agostino, C.; Harris, R. C.; Abbott, A. P.; Gladden, L. F.; Mantle, M. D., Molecular motion and ion diffusion in choline chloride based deep eutectic solvents studied by <sup>1</sup>H pulsed field gradient NMR spectroscopy. *Physical Chemistry Chemical Physics* **2011**, 13 (48), 21383-21391.
25. Du, C.; Zhao, B.; Chen, X.-B.; Birbilis, N.; Yang, H., Effect of water presence on choline chloride-2urea ionic liquid and coating platings from the hydrated ionic liquid. **2016**, 6, 29225.
26. Abbott, A. P.; Boothby, D.; Capper, G.; Davies, D. L.; Rasheed, R. K., Deep Eutectic Solvents Formed between Choline Chloride and Carboxylic Acids: Versatile Alternatives to Ionic Liquids. *J. Am. Chem. Soc.* **2004**, 126 (29), 9142-9147.
27. Wei, J. C.; Schwartz, M.; Nobe, K., Aqueous Electrodeposition of SmCo Alloys: I. Hull Cell Studies. *Journal of The Electrochemical Society* **2008**, 155 (10), D660-D665.
28. Martell, A. E.; Smith, R. M., Critical stability constants. **1974**.
29. Huang, Q.; Bedell, S. W.; Saenger, K. L.; Copel, M.; Deligianni, H.; Romankiw, L. T., Single-Crystalline Germanium Thin Films by Electrodeposition and Solid-Phase Epitaxy. *Electrochemical and Solid-State Letters* **2007**, 10 (11), D124-D126.

## Supplementary Information

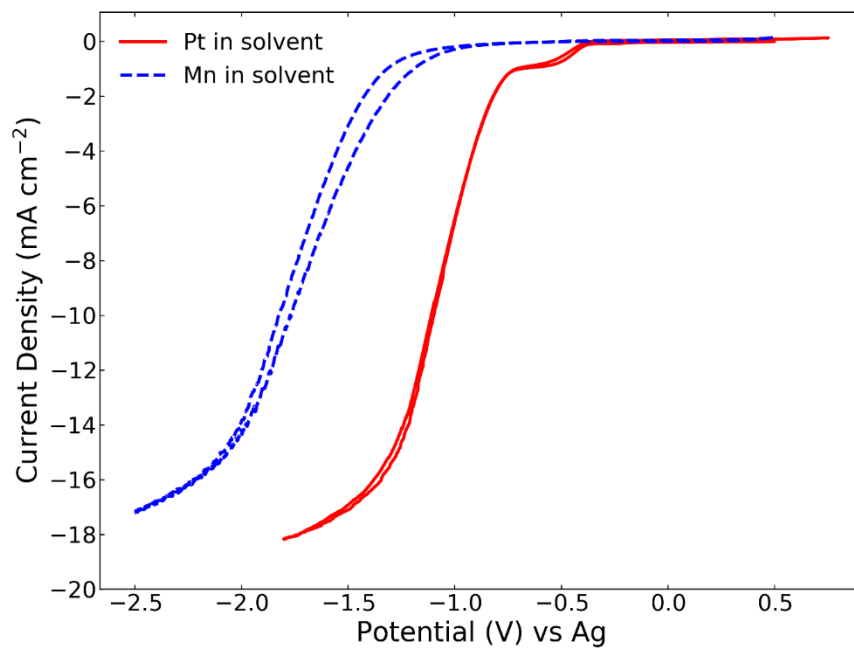


Figure S 3-1. Cyclic voltammogram of a Mn coated electrode in the ChCl-U solvent, compared with that of a Pt electrode in the same solvent, scan rate 5 mV·s<sup>-1</sup>.

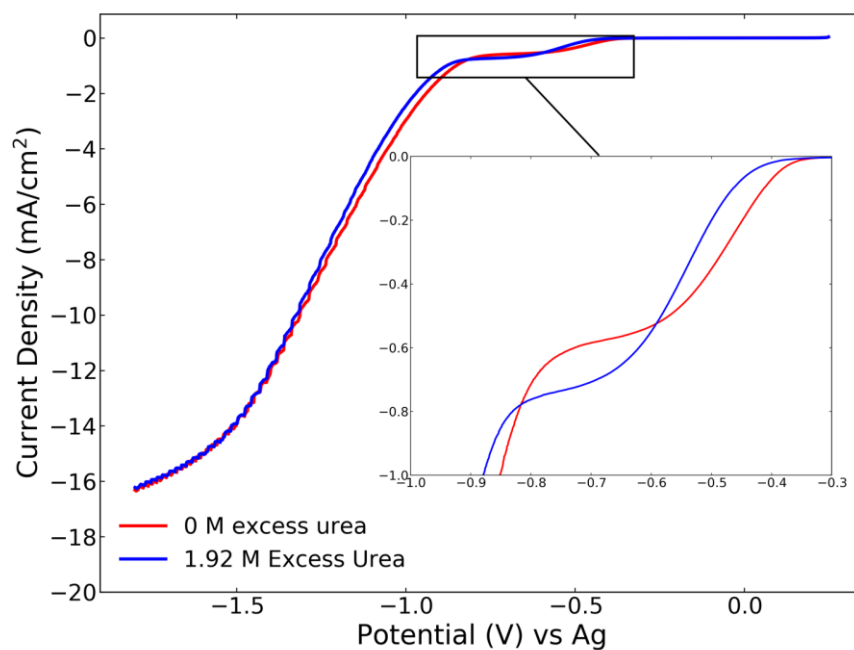


Figure S 3-2. Cyclic voltammogram taken at 5 mV·s<sup>-1</sup> showing the effect of excess urea in the solvent on the limiting current of the reaction beginning at -0.35 V.

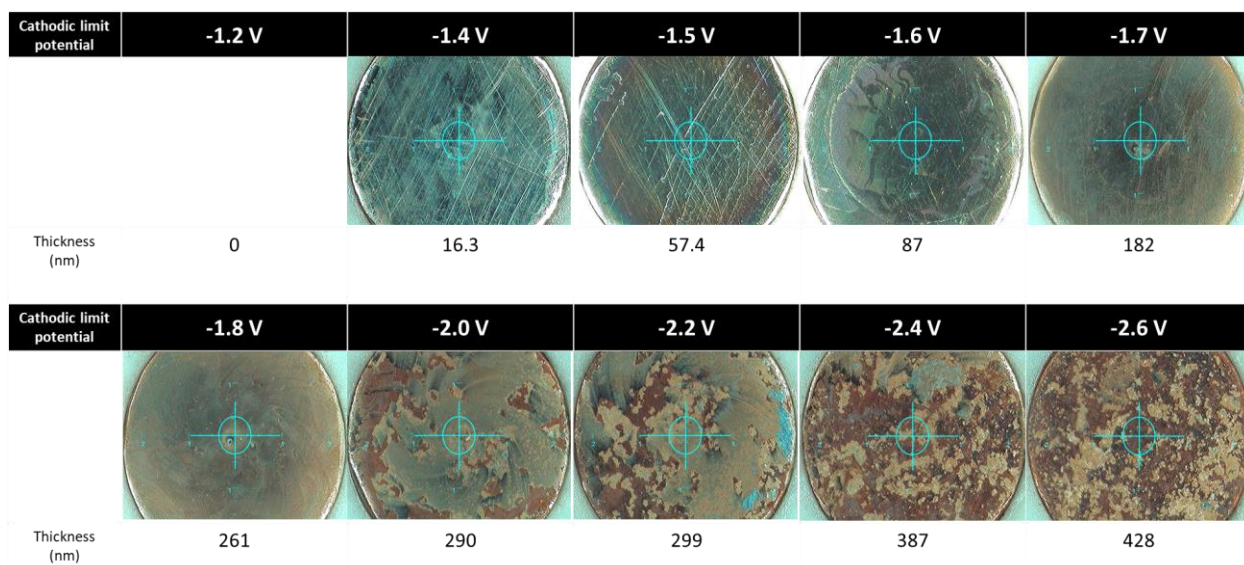


Figure S 3–3. Optical images of the substrate after linear sweep voltammetry from open circuit potentials to various cathodic limits, at a scan rate of  $5 \text{ mV}\cdot\text{s}^{-1}$ .

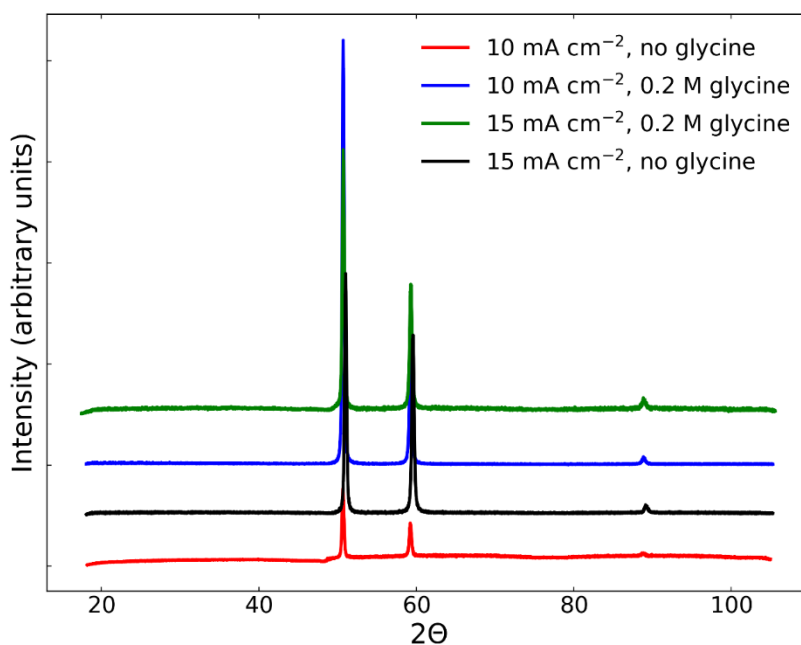


Figure S 3–4. XRD diffractograms of films deposited galvanostatically at various current densities, with and without glycine. Observed peaks are characteristic of the copper substrate.

## CHAPTER 4. ELECTRODEPOSITION OF FERROMAGNETIC FeCo AND FeCoMn ALLOY FROM CHOLINE CHLORIDE BASED DEEP EUTECTIC SOLVENT\*

### Summary

The electrodeposition of Fe, Co, FeCo, and FeCoMn alloy films has been performed from the choline chloride/urea deep eutectic solvent without additives. The effects of solution temperature, electrolyte concentration, deposition potential, and solution agitation on deposition rate have been studied. Film composition, morphology, crystallographic structure as well as the magnetic moment and coercivity were characterized and compared against the deposition conditions. A dominant mass transport effect was observed across most of the deposition cases. A manganese underpotential deposition phenomenon occurred with the alloy deposition. An elevated temperature results in significantly faster deposition and promotes smooth film growth with limited cracking. As-deposited FeCo alloy films are found to be ferromagnetic and nanocrystalline.

### Introduction

The desire to continue to increase areal data density in magnetic recording media requires advancements in many areas, one being the ability of the write head to overcome the higher anisotropy fields in the magnetic media.<sup>1</sup> Among the many techniques to increase the effectiveness of the write head, the simplest one is to increase the saturation magnetization,  $M_s$ , of the head material. This effort has successfully driven the

---

\* This chapter was published in the *Journal of The Electrochemical Society* **2019**, 166 (4), W.D. Sides, N. Kassouf, Q. Huang

development of magnetic recording in the past until the 2000's, when the 2.4 T FeCo alloy was implemented in production. Requirements for the write head material include a low coercivity  $H_c$ , high  $M_s$ , and good corrosion resistance.<sup>2</sup> While the early thin film write heads were made from permalloy, extensive research was undertaken to find suitable replacements with better soft magnetic properties, including binary, and later tertiary, Fe-Co alloys. Researchers have attempted to include B,<sup>3</sup> P,<sup>4</sup> Cr,<sup>5</sup> Cu,<sup>2</sup> and Ni<sup>6</sup> into tertiary Fe-Co materials, with the most well studied being Co-Fe-Ni. The binary Fe-Co alloy was found to possess the highest magnetic moment of all. Some other transition metals, such as Ru and Mn, have been predicted to have anomalous ferromagnetic ordering when incorporated into cobalt-rich Fe-Co alloys, increasing  $M_s$  for these tertiary systems.<sup>7</sup>

Electrodeposition has been used to produce write head thin films due to its low cost, compatibility with photoresist,<sup>8</sup> technical simplicity of orienting anisotropy during film growth,<sup>9</sup> and its ease of control over film composition. More importantly, electrodeposited films often have better soft magnetic properties than those fabricated by vacuum deposition or other methods due to the finer grains that result from the non-equilibrium nature of electrodeposition.<sup>8-9</sup> The limitations of electrodeposition generally arise from the simultaneous hydrogen evolution reaction that occurs when depositing from aqueous baths. When depositing thin films, this side reaction reduces current efficiency,<sup>2</sup> and in the worst cases can lead to cracked, low quality films.<sup>10</sup> The simultaneous hydrogen evolution during aqueous electrodeposition limits the metals that can be deposited to those with high electrochemical equilibrium potentials relative to water. This prevents the incorporation of metals such as Mn, which has been suggested to increase  $M_s$ ,<sup>7</sup> and enhance corrosion resistance.<sup>11</sup> Another pitfall to aqueous electrodeposition is the tendency to form and

incorporate metal compounds, such as hydrides, hydroxides, and oxides, which can be detrimental to the magnetism of deposited films.<sup>6,9</sup>

To overcome these limitations, non-aqueous solvents have been extensively investigated for electrodeposition in the last decade.<sup>12-19</sup> Among them, choline chloride based deep eutectic solvents (DES), a class of room temperature ionic liquids, have emerged as promising water substitutes for many thin film electrodepositions due to their low cost, atmospheric stability, thermal stability, low toxicity, ability to dissolve many metal salts, and relatively high conductivity.<sup>14, 20-22</sup> The use of DES avoids the issue of hydrogen evolution, generally leading to higher quality deposits, and allowing metals such as Mn to be easily incorporated into the alloy.<sup>23</sup> The wide electrochemical window of DES allows for more control over nucleation and deposition rates, which can affect crystal grain size. It has been observed that very fine crystallites are desirable to reduce the coercivity in soft magnetic materials,<sup>24</sup> thus the ability to tune this size could prove beneficial. In this work, the electrodeposition of magnetic Co-Fe alloy has been studied from the DES consisting of a 1:2 molar ratio of choline chloride to urea (ChCl-U). In addition, Mn has been incorporated to form a tertiary alloy from a single bath deposition. The composition and magnetic properties have been determined and correlated to deposition conditions, which were varied in temperature, bath agitation, metal ion concentration, and deposition potential.

## **Experimental**

Choline chloride (Acros Organics, 99%) was dried under vacuum for 2 days at 60 °C. Urea (Acros Organics, 99%) was dried for 2 days at 80 °C in air. Components were combined in a 1:2 molar ratio at 70 °C and mixed until a clear, colorless liquid was formed.

Cobalt sulfate heptahydrate, iron sulfate heptahydrate, and manganese chloride tetrahydrate were used as received, stirred into solutions in appropriate quantities. Based on a density of  $1.164 \text{ g}\cdot\text{mL}^{-1}$ ,<sup>25</sup> the concentrations of choline chloride and urea are 4.5 and 9.0 M, respectively. While no attempts were made to dehydrate the metal salts, the water content in the electrolyte is believed to be lower than 2 wt% due to the natural loss of water that occurs upon heating to  $80 \text{ }^\circ\text{C}$ .<sup>26</sup> Moreover, small amounts of water in the solution are reported to help the deposition characteristics by reducing the solution viscosity and increasing solution conductivity and the solubility of various metal salts, without impacting the electrochemical window of the solvent.

An Autolab PG320N potentiostat/galvanostat with a frequency analyzer was used for the electrochemical studies. The electrochemical cell consisted of an Ag wire pseudo reference electrode and a Pt sheet counter electrode. All potentials referred to in this chapter are referenced against Ag, Pt or Cu rotating disk electrodes (RDE) of 5 mm diameter were employed as the substrate. The former was used for cyclic voltammetry, and the latter for DC deposition of alloy films for characterization. While the Pt disk was used as provided, copper disks were cut in-house, polished to a mirror finish with diamond slurry, sonicated for 10 minutes in DI water, etched in dilute sulfuric acid, and air dried prior to use. The position of the electrodes within the bath was fixed between experiments, and solution resistance was measured using electrochemical impedance spectroscopy (EIS). After electrodeposition, films were thoroughly rinsed in DI water and air dried prior to analysis.

Deposit thickness and composition measurements were performed using a Bruker x-ray fluorescence (XRF) operated at 50 kV and  $800 \text{ }\mu\text{A}$ . An average value was calculated

from 6 measurements across the diameter of the copper RDE. Film morphology was analyzed using a JEOL 7000 FE scanning electron microscope (SEM) equipped with an energy dispersive x-ray spectrometer (EDS). X-ray diffraction (XRD) measurements were carried out on a Bruker D8 powder diffractometer with a Co  $K\alpha$  x-ray source. Magnetic hysteresis loops were collected on a DMS vibrating sample magnetometer (VSM).

## Results and Discussion

Before deposits were attempted, the habitual electrochemical studies were undertaken. Cyclic voltammograms (CV) were first taken on solutions of the individual Fe and Co metal ions, dissolved in ChCl-U, and are presented in Figure 4–1. All CVs in this study were performed with a slow scan rate of  $5 \text{ mV}\cdot\text{s}^{-1}$  in order to approximate a steady state polarization curve. A rotation rate of 550 RPM is approximately equivalent to a typical paddle movement velocity of  $0.4 \text{ m}\cdot\text{s}^{-1}$  or a frequency of 1 Hz in an 8-inch long paddle cell.

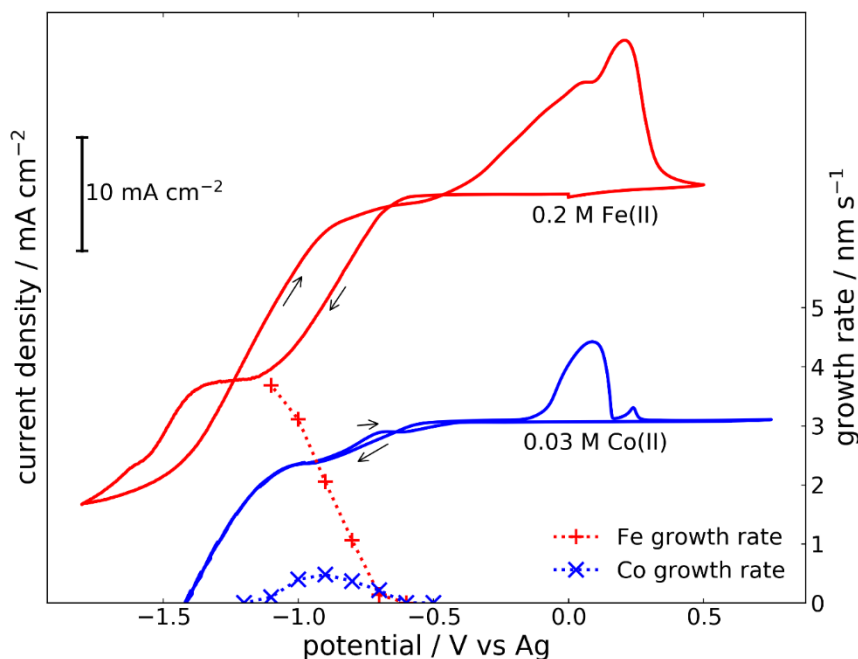


Figure 4–1. Cyclic voltammograms of ChCl-U solutions containing either 0.2 M Fe(II) or 0.03 M Co(II), on a Pt RDE at 1000 RPM, 80 °C, and a scan rate of  $5 \text{ mV}\cdot\text{s}^{-1}$ . Potentiostatic film growth rates from the same solutions are shown to confirm peak assignment.

This study covers a range of 1000 and 250 RPM. Detailed electrochemical studies of Mn in this solvent have been presented elsewhere in the literature.<sup>23</sup> The Fe solution had a concentration of 0.2 M  $\text{FeSO}_4 \cdot 7\text{H}_2\text{O}$ , and the Co solution had a concentration of 0.03 M  $\text{CoSO}_4 \cdot 7\text{H}_2\text{O}$ . Metal salts were not dehydrated prior to use, resulting in the introduction of water into solution. It has been observed, however, water easily evaporates from this solvent to less than 2 wt% when held at 80 °C for several hours, as done here.<sup>26</sup> Moreover, small amounts of water (< 6 wt%) are not electrochemically active and may, in fact, increase the solubility of metal salts and decrease the viscosity of the solution. Scans were taken on a Pt RDE at 80 °C and a rotation rate of 1000 RPM. Curves for both species behaved similarly, exhibiting a cathodic current plateau corresponding to metal ion reduction, followed at more negative potentials by a sharp rise in cathodic current due to solvent breakdown. Deposition began near -0.6 V for both metals, and a limiting current is observed at -1.1 V and -0.9 V for Fe and Co, respectively. It is seen that the difference in onset potentials for Co and Fe deposition is much less than 100 mV, whereas the difference in their reduction potentials expected from Pourbaix diagram is 139 mV in aqueous solutions.<sup>27-28</sup> This confirms observations by other researchers that this class of DES can bring the deposition potentials of many metals closer together.<sup>29-31</sup> A variation in deposition onset potentials in DES versus water is expected because the metal ions form different complexes. Whereas Co(II) ions in aqueous solution are expected to exist as hexahydrate complexes, they are likely to exist as anionic chloro-complexes in this DES, potentially altering the electrochemical behavior of the Co(II) significantly. The predominate reaction occurring beyond the metal deposition limiting current plateau has been reported to be the breakdown of choline to form trimethylamine gas.<sup>32</sup> The

emergence of a fishy odor from the electrochemical cell supports this reaction assignment. In both cases, anodic stripping peaks are observed as expected. To confirm peak assignments, potentiostatic depositions were performed at various potentials, for 5 minutes. The resulting film thickness was measured by XRF to determine the potential dependent growth rate of Fe or Co metal films. Results are shown in Figure 4–1. It is seen that the Fe growth rate increases proportionally to the CV current from its deposition onset potential until the CV plateau is reached. On the other hand, Co growth initially follows this expected behavior, however large overpotentials lead to a decrease in the film growth rate. No Co film growth is possible after 5 minutes at potentials below -1.2 V. Even at the potential where the Fe partial current was greatest, -0.9 V, the current efficiency of deposition was merely 33%. It is possible that cobalt forms surface compounds at highly cathodic potentials in the presence of chloride that inhibit its growth. Similar behavior has been observed during Mn deposition from this solvent,<sup>23</sup> as well as Co and Ru deposition from aqueous solvents with a similarly high concentration of chloride ions. Metal chlorine compounds have also been reported for Cu in choline chloride based solvents.<sup>33</sup> Based on these results, the limiting partial currents of metal deposition for Fe and Co are found to be -9.82 and -1.38 mA·cm<sup>-2</sup>, respectively.

CVs were then performed on the Fe-Co codeposition system, under various conditions. Figure 4–2 (a) shows the effect of temperature and rotation rate on the deposition behavior, while Figure 4–2 (b) shows the effect of Fe(II) concentration. In any case, a single peak is observed with an onset potential of -0.76 V. At 80 °C and 1000 RPM, the limiting current of codeposition is -9.4 mA·cm<sup>-2</sup>. This is less than the sum of the limiting currents observed in Fe and Co individual depositions observed in Figure 4–1,

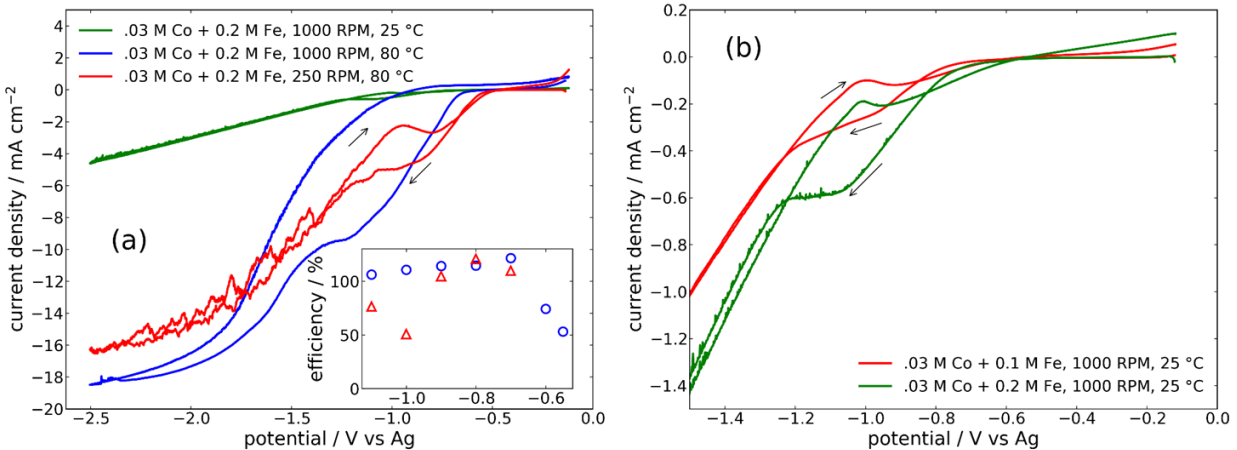


Figure 4-2. Cyclic voltammograms at  $5 \text{ mV}\cdot\text{s}^{-1}$  on a Cu RDE in Fe and Co containing ChCl-U solution showing (a) the effect of temperature and rotation rate and (b) the effect of Fe ion concentration at room temperature. Inset in (a): current efficiencies of 300 s potentiostatic depositions at identical conditions to (blue circles) the 1000 RPM,  $80 \text{ }^\circ\text{C}$  CV curve, and (red triangles) the 250 RPM  $80 \text{ }^\circ\text{C}$  CV curve.

under identical conditions, which are  $-16.5$  and  $-3.7 \text{ mA}\cdot\text{cm}^{-2}$ , respectively. The limiting current in the codepositing system is very similar, however, to the sum of the Fe and Co partial currents during individual depositions,  $-9.82$  and  $-1.38 \text{ mA}\cdot\text{cm}^{-2}$ , respectively. This indicates that during Fe-Co codeposition, the side reaction was nearly eliminated. Current efficiency measurements taken of potentiostatic depositions by XRF, shown in the inset of Figure 4-2 (a), show that this is indeed the case, as deposition current efficiency is near 100% in the potential range where the limiting current was observed in the CV. Although XRF is accurate enough to obtain information on trends in the results, slight errors are observed manifested as current efficiencies greater than 100%. The thickness calculation in the XRF machine relies on the x-ray intensity and expected density of the deposited layer as well as the x-ray intensity of the substrate. Given the fact that the film may contain significant amounts of impurities (to be presented in Figure 4-10), the measured film thickness may be greater than the effective thickness of only the electrochemically deposited Fe and Co, had it been a pure film. The limiting current was not observed on the

Table 4-1. Conditions of potentiostatic deposition experiments

	Fe(II) Concentration M	Co(II) Concentration M	Temperature °C	RDE rotation RPM
Condition 1	0.1	0.03	25	1000
Condition 2	0.2	0.03	25	1000
Condition 3	0.2	0.03	80	1000
Condition 4	0.2	0.03	60	1000
Condition 5	0.2	0.03	80	250

reverse scan of the CV, resulting in significant hysteresis in the potential region where metal deposition dominates. This hysteresis is likely resultant from a passivating layer that forms on the electrode surface at highly negative potentials, which is discussed in more detail later. At 80 °C, reducing the rotation rate by a factor of four had the expected effect of halving the mass transfer limited current. Interestingly, it also allowed for the solvent breakdown to occur at an onset potential of -1.0 V as shown by a reduction in current efficiency at these potentials and rising current wave on the CV beginning at -1.0 V, whereas this rising current wave did not occur until -1.3 V when the RDE was set to 1000 RPM. Noise introduced into the 250 RPM CV during the second current wave is a further indication of a gaseous product such as trimethyl amine, as bubbles are continuously formed and partially block the RDE surface, before being spun off by the rotation. At the faster rotation rate, bubbles are spun off more rapidly and so do not introduce the same noise. By reducing the temperature to 25 °C, the limiting current is reduced by three orders of magnitude, nearly the same amount by which the viscosity of the solvent increases over this temperature range. At room temperature, the solution containing only 0.1 M Fe(II) reaches a mass transport limited plateau near -0.96 V. When the Fe(II) concentration is doubled, increasing the total dissolved metal concentration by 77%, the limiting current increases by 62% and is not reached until -1.09 V.

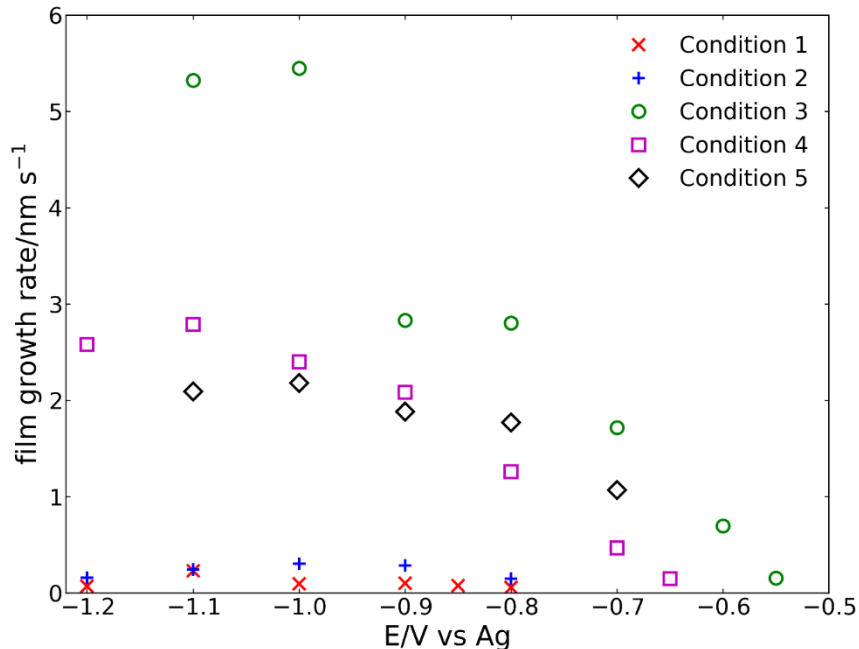


Figure 4-3. Potential dependent growth rate of the alloy film under the various conditions listed in Table 4-1.

A series of potentiostatic depositions were run at various conditions to determine the effect of temperature, metal ion concentration, mass transport (rotation rate), and potential on the composition and growth rate of the Co-Fe alloy film. The conditions listed in Table 4-1 were each tested over a range of potentials. Figure 4-3 shows the total alloy growth rate based on XRF film thickness measurements of the films. In agreement with the cyclic voltammogram, doubling the Fe(II) concentration doubles the film growth rate at most deposition potentials, indicating that the alloy deposition is mass transport controlled in this potential range. Increasing the temperature results in an increase in growth rate proportional to the viscosity reduction over the same temperature range. At 20 °C, the viscosity of this solvent is reported to be 1372 cP, increasing the temperature to 60 °C and 80 °C reduces the viscosity to 69 cP and 28 cP, respectively.<sup>25</sup> As predicted by Levich,<sup>34</sup> increasing the rotation rate four-fold from 250 to 1000 RPM results in a doubling of the deposition rate within the mass transfer limited region. At low overpotentials, however

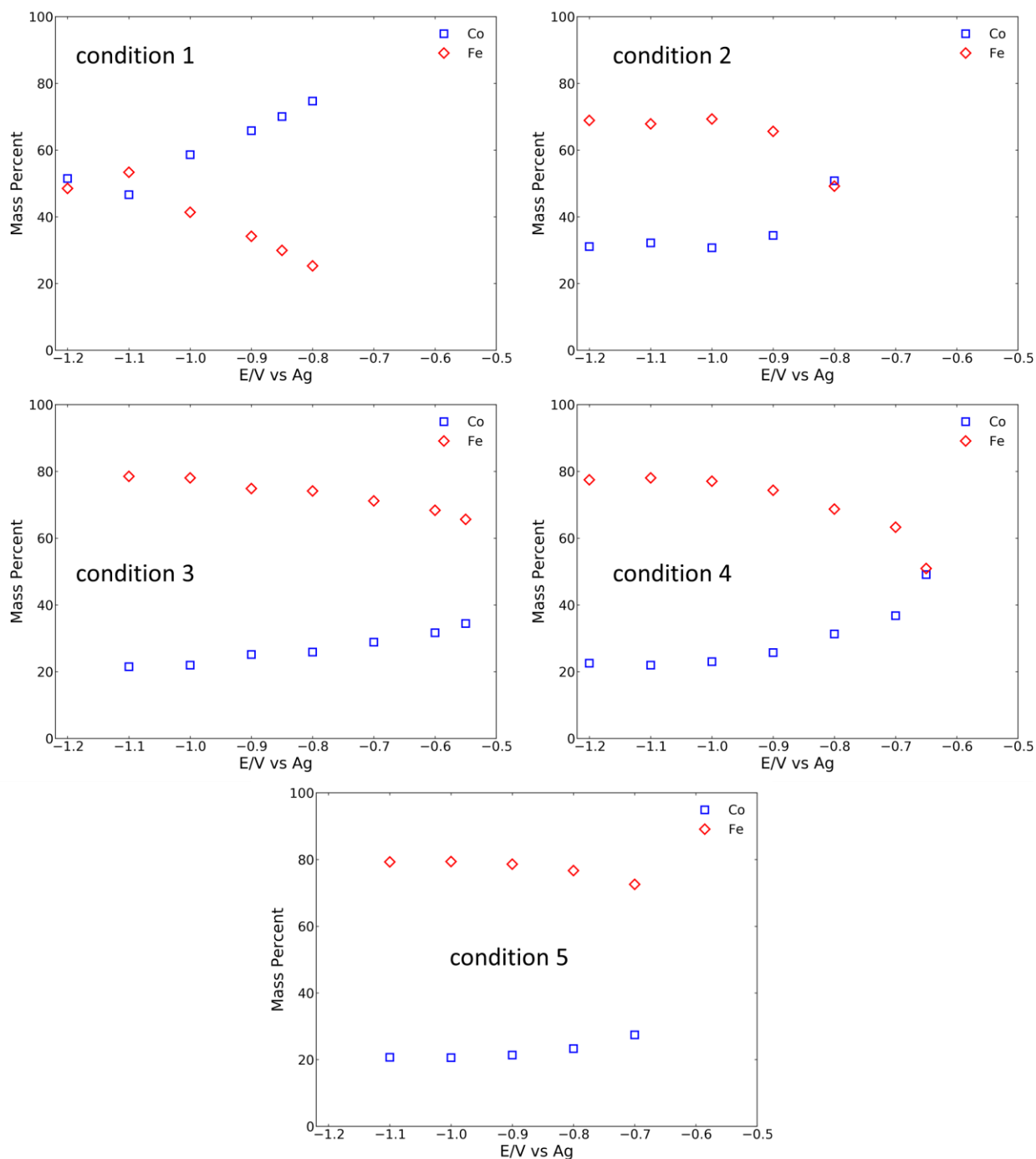


Figure 4-4. Compositions of FeCo films grown potentiostatically at various potentials, under the conditions listed in Table 4-1.

there is less difference between the deposition rate at 1000 RPM and at 250 RPM, indicating that ionic mass transport is not the rate limiting factor at these lesser overpotentials.

Figure 4–4 presents the compositions of films grown under the various different conditions listed in Table 4–1. When the composition of the films depends on the deposition potential, a mass transport limitation of deposition rate has not yet been reached for at least one depositing species. Doubling the Fe ion concentration results in a corresponding increase of Fe content in the deposit. By increasing the temperature of the solution to 60 °C, the limiting current should increase due to reduced viscosity and increased ion diffusivity. Indeed, greater overpotentials are required at 60 °C (condition 4) to achieve limiting currents for both species. Further increasing the temperature to 80 °C (condition 3) continues the same trend; at this temperature at 1000 RPM, the composition of the deposit is dependent on potential throughout the entire potential range tested. By reducing the rotation rate to 250 RPM, thereby reducing the limiting current, the composition of the films is observed to again be independent of potential within the potential test range. In all cases studied, more negative deposition potentials led to a higher composition of Fe in the film, indicating that the reduction potential of Fe remains more negative than that of Co in this solvent. The Fe composition in deposited films remains smaller than that of Fe ions in the solution in all cases. Since no enhancement of Fe deposition or inhibition of Co deposition is observed, the anomalous codeposition phenomenon often exhibited in aqueous systems is not detected in the ChCl-U solvent. Other researchers have come to similar conclusions, finding that alloys which exhibit anomalous codeposition in aqueous systems do not behave similarly in ionic liquids.<sup>31</sup> The properties of all deposits are tabulated in Table 4–2.

As a demonstration of this solvent's ability to incorporate into alloys metals with a very negative deposition potential relative to hydrogen evolution, Mn was incorporated

Table 4–2. Properties of FeCo alloy films obtained from potentiostatic depositions

Condition	$E$ V	Time s	Thickness nm	Co %	Fe %	$H_c$ Oe	$\mu_o M_s$ T	$D$ nm
1	-0.85	600	47	70.1	30.0	-	-	-
1	-0.90	600	62	65.8	34.2	-	-	-
1	-1.00	600	59	58.6	41.4	-	-	-
1	-1.10	600	139	46.6	53.4	-	-	-
1	-1.20	600	42	51.5	48.5	-	-	-
2	-0.80	600	90	50.8	49.2	-	-	-
2	-0.90	600	172	34.4	65.6	-	-	-
2	-1.00	600	183	30.7	69.3	-	-	-
2	-1.10	600	146	32.2	67.8	-	-	-
2	-1.20	600	96	31.1	68.9	-	-	-
2	-1.25	600	54	27.2	72.8	-	-	-
3	-0.55	300	46	34.4	65.6	-	-	-
3	-0.60	300	209	31.7	68.3	244	1.16	-
3	-0.70	300	515	28.8	71.2	-	-	79
3	-0.80	600	1683	25.9	74.1	-	-	223
3	-0.90	300	850	25.1	74.9	-	-	-
3	-1.00	300	1635	21.9	78.1	794	0.41	-
3	-1.10	300	1597	21.5	78.5	258	0.83	33.4
4	-0.65	300	45	49.1	50.9	-	-	-
4	-0.70	300	141	36.7	63.3	-	-	-
4	-0.80	300	379	31.3	68.7	503	0.88	25
4	-0.90	300	625	25.7	74.3	415	0.98	-
4	-1.00	300	720	23.0	77.0	-	-	21
4	-1.10	300	836	22.0	78.0	305	0.72	-
4	-1.20	300	775	22.5	77.5	245	0.69	-
5	-0.70	300	321	27.4	72.6	-	-	-
5	-0.80	300	531	23.3	76.7	732	0.71	39
5	-0.90	300	565	21.4	78.6	544	0.81	-
5	-1.00	300	654	20.6	79.4	496	1.16	-
5	-1.10	300	628	20.7	79.3	-	-	-

into Fe-Co deposition solutions. CVs were performed on a solution containing 0.1 M Fe(II), 0.03 M Co(II), and 0.1 Mn(II), as well as a solution containing 0.2 M Fe(II), 0.03 M Co(II), and 0.25 Mn(II), and are presented in Figure 4–5. No cathodic deposition peaks corresponding to individual elements are observed, however a large anodic peak indicates that metal deposition occurred. Galvanostatic depositions of 0.8 C·cm<sup>-2</sup> total charge in the

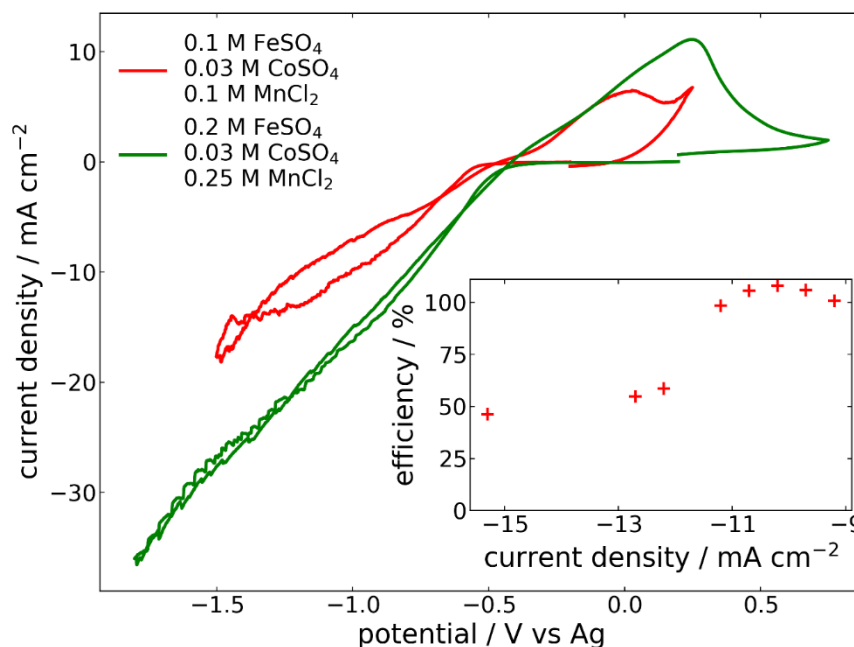


Figure 4-5. Cyclic voltammograms at 80 °C with a scan rate of 5 mV·s<sup>-1</sup> on a Pt RDE in ChCl-U solutions containing Fe, Co, and Mn ions. Inset: Current efficiencies of 0.8 C·cm<sup>-2</sup> galvanostatic depositions at identical conditions to the red CV curve.

solution containing 0.1 M Fe(II), 0.03 M Co(II), and 0.1 Mn(II) indicate that all three metals deposit simultaneously at current densities greater than -9 mA·cm<sup>-2</sup>, corresponding to a potential of -0.9 V. The current efficiency of metal deposition is near 100% at current densities up to -11 mA·cm<sup>-2</sup>; current densities greater than 12 mA·cm<sup>-2</sup> are accompanied by a significant side reaction. This current density corresponds to a potential of -1.2 V, also the potential at which the CVs of the Fe, Co, and FeCo solutions began to incur significant side reaction peaks (Figures 4-1 and 4-2).

A series of thick galvanostatic depositions (26 C·cm<sup>-2</sup> total charge) was performed in the solution containing 0.1 M Fe(II), 0.03 M Co(II), and 0.1 Mn(II). This ratio of Fe to Co was chosen with the intention to obtain deposits with an Fe to Co ratio of 0.65 to 0.35. These deposits had much less deposited mass than expected based on the previously determined current efficiencies taken from shorter depositions. This phenomenon can also be seen in Mn

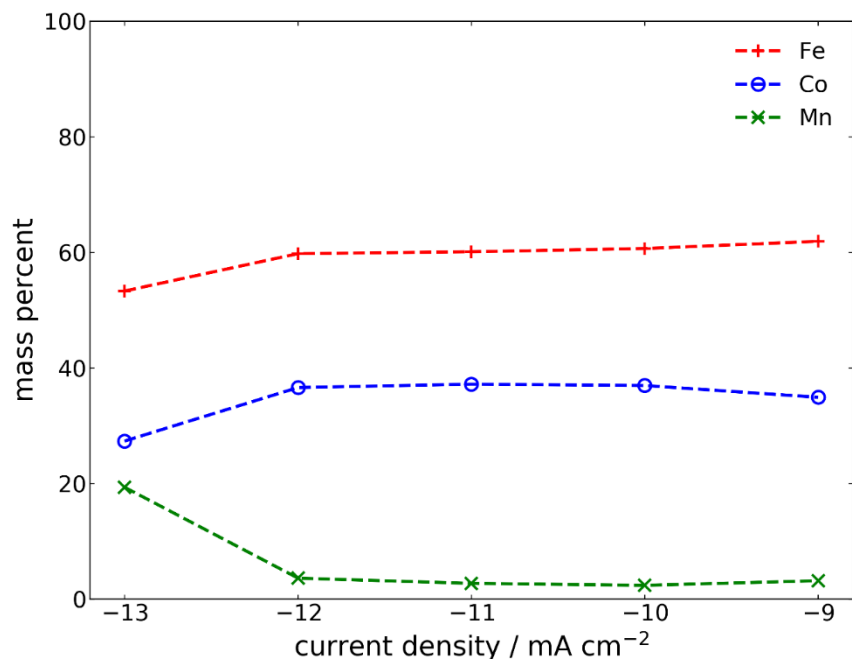


Figure 4–6. Compositions of FeCoMn films grown galvanostatically on a Cu substrate from a solution of ChCl-Urea containing 0.1 M FeSO<sub>4</sub>, 0.03 M CoSO<sub>4</sub>, and 0.1 M MnCl<sub>2</sub> at 80 °C and 1000 RPM.

deposition,<sup>23</sup> and although the precise cause is unknown, it is likely due to a passivating film forming after a certain amount of time, inhibiting further deposition. Regardless, the compositions of the films are presented in Figure 4–6. At current densities from 9 to 12 mA·cm<sup>-2</sup>, the composition of the films is independent of growth current. A constant amount of Mn near 3% is incorporated into the deposit at these conditions, which correspond to potentials from -0.9 V to -1.15 V. These potentials are all less negative than the onset potential of deposition of pure Mn in this solvent, which is reported to be -1.2 V.<sup>23</sup> Underpotential deposition (UPD) phenomena are not unusual for alloy deposition systems because alloys can have negative Gibbs energies of formation. This case is interesting because the amount of Mn incorporated at UPD conditions is limited and constant at only about 3%. The film deposited at -13 mA·cm<sup>-2</sup> has significantly more Mn, which is expected

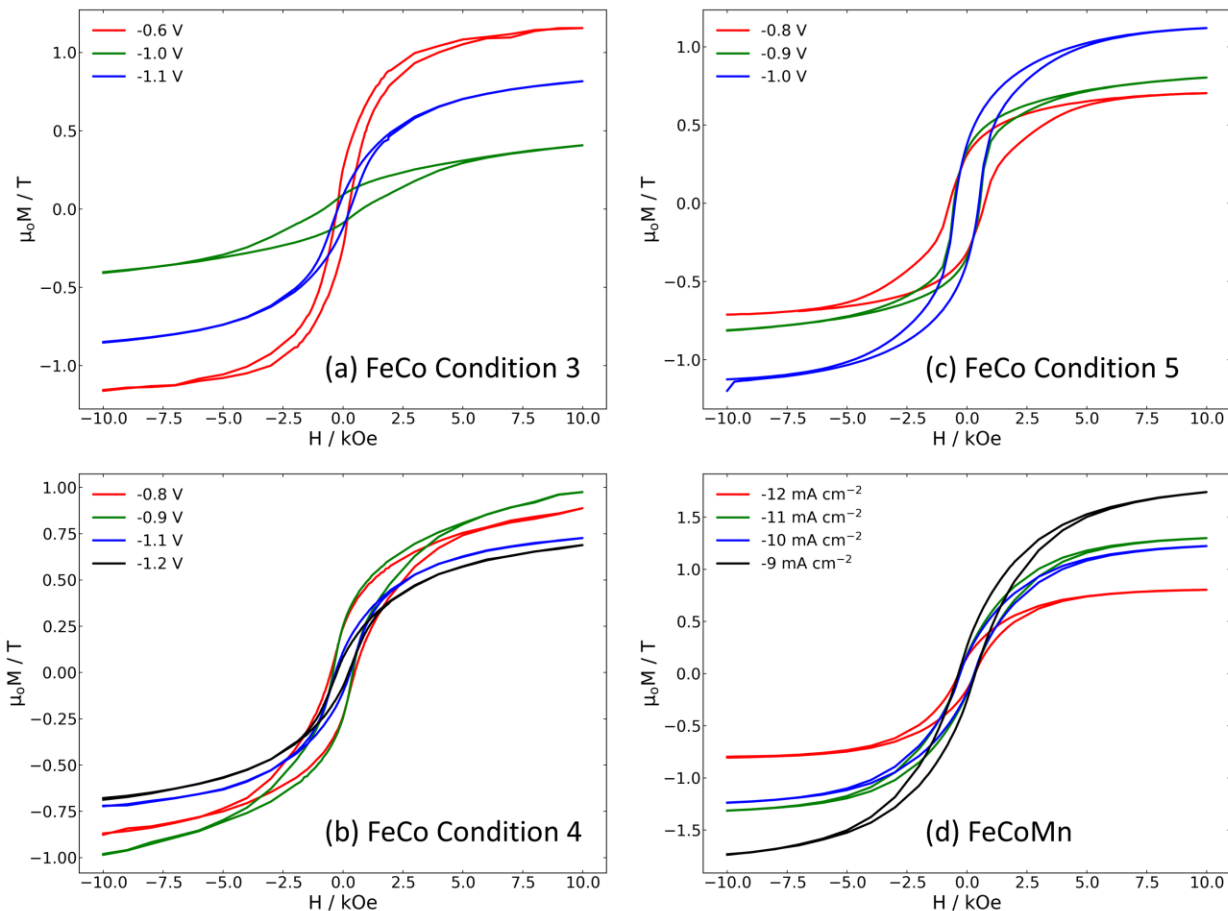


Figure 4-7. In-plane hysteresis loops of ferromagnetic samples of (a-c) FeCo deposited at the indicated potential and conditions as described in Table 4-1 and (d) FeCoMn deposited galvanostatically under various current densities.

as this current corresponds to a potential of -1.23 V, slightly overpotential to the onset of bulk Mn deposition.

The magnetic properties of FeCo films grown potentiostatically were obtained from M-H hysteresis loops presented in Figure 4-7 (a). The saturation magnetization was calculated using the film thickness obtained from XRF measurements. Many samples, particularly very thin samples, did not exhibit the well-defined hysteresis loop expected of ferromagnetic materials, and these cases have been omitted from Figure 4-7. Values of the vacuum permeability  $\mu_0$  times  $M_s$  as well as  $H_c$  of the samples exhibiting well-defined ferromagnetism have been reported in Table 4-2. It is seen that these samples have a wide

Table 4–3. Properties of FeCoMn alloy films obtained from galvanostatic depositions in a solution of ChCl-Urea containing 0.1 M FeSO<sub>4</sub>, 0.03 M CoSO<sub>4</sub>, and 0.1 M MnCl<sub>2</sub> at 80 °C and 1000 RPM.

<i>i</i> mA·cm <sup>-2</sup>	Thickness nm	Co %	Fe %	Mn %	<i>H<sub>c</sub></i> Oe	μ <sub>o</sub> <i>M<sub>s</sub></i> T	<i>D</i> Nm
-9	514	34.9	61.9	3.2	350	1.74	-
-10	3392	37.0	60.7	2.4	298	1.23	14
-11	3739	37.2	60.1	2.7	290	1.31	36
-12	1337	36.6	59.8	3.6	334	0.80	-
-13	97	27.3	53.3	19.4	-	-	-

variation in their magnetizations and coercivities, but that the magnetizations are generally low compared to FeCo films obtained by aqueous electrodeposition.<sup>35</sup> Likewise, Figure 4–7 (b) shows M-H loops for the FeCoMn films deposited galvanostatically, and their properties are tabulated in Table 4–3. Although their magnetizations are generally greater than the FeCo films, wide variability in the values are observed due to impurities in the deposits and variations in the film compositions. Coercivities are consistent in these samples, at around 300 Oe. For both binary and tertiary alloy films, magnetizations generally decrease as the Fe content diverges from 65%, the composition reported as exhibiting the maximum magnetization in Fe-Co alloy.<sup>36</sup> Even at compositions near 65% Fe, magnetizations of FeCo and FeCoMn films deposited from ChCl-U are reduced compared to bulk FeCo. The reduced magnetizations among both alloy types versus expected bulk values are likely explained by high impurity content within the films. Indeed, EDS measurements were performed on one FeCoMn sample and do indicate the presence of a significant amount of oxygen and carbon in the film, however no nitrogen or chlorine was detected. These impurities are expected to form non-magnetic species with iron group metals, which dilute magnetism within the film.

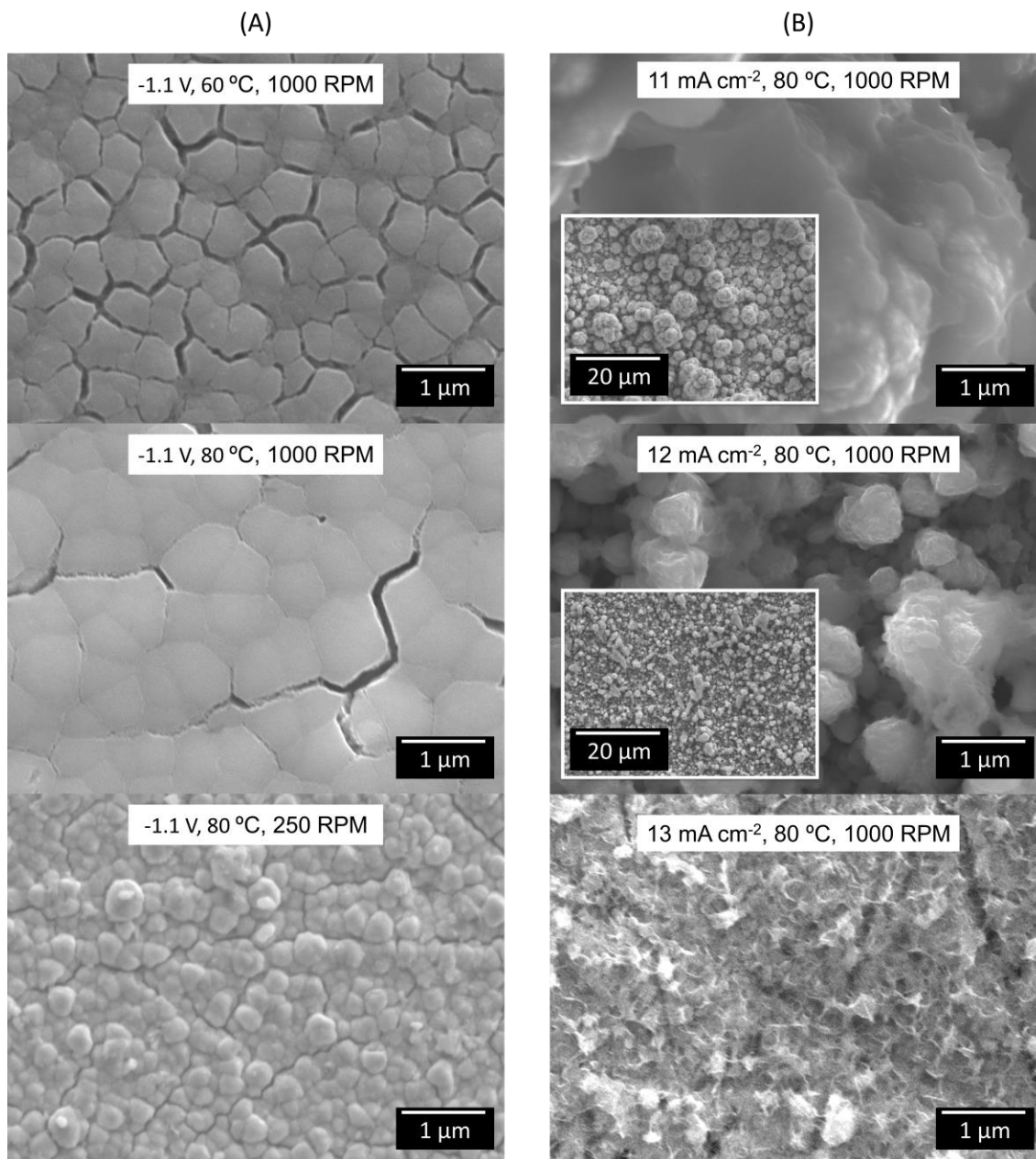


Figure 4–8. Morphologies of (A) FeCo films deposited under various conditions at -1.1 V and (B) FeCoMn films deposited under various current densities.

Magnetic properties depend greatly on film morphology and crystal structure, which can often be improved with the use of additives to the deposition bath, or other variations in deposition conditions. SEM images have been taken of the deposited FeCo and FeCoMn films, and representative images are presented in Figure 4–8. FeCo films were generally smoother, however significant cracking was observed on thicker films due to

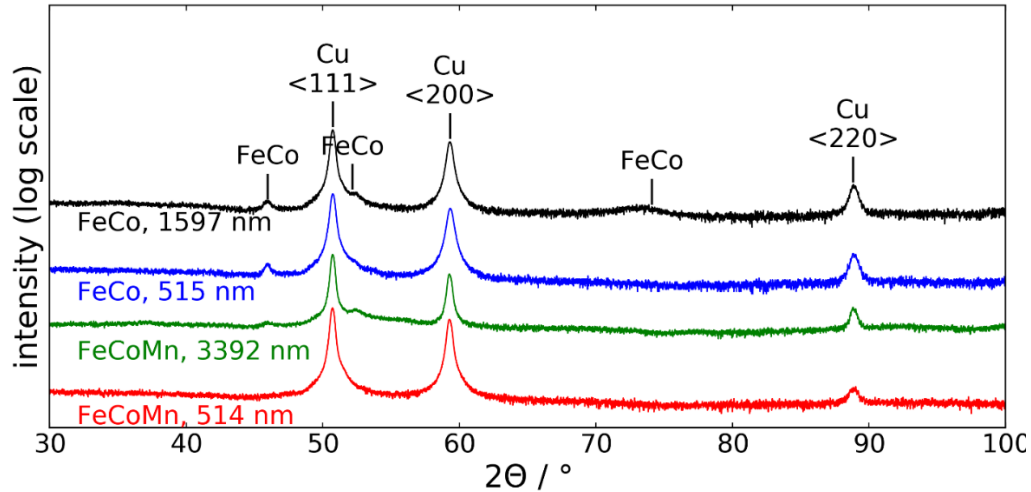


Figure 4–9. XRD diffractograms of selected FeCo and FeCoMn films from a  $\text{Co } \alpha$  x-ray source. Intensity is displayed on a log scale.

stresses. Elevated temperatures resulted in fewer cracks in the deposited film, even if a thicker film was deposited. Upon reduction in the rotation rate from 1000 RPM to 250 RPM, the film morphology appears to change from flat, uniform growth to a more 3-dimensional growth. The CV results in Figure 4–2 (a) show that reducing the rotation rate from 1000 to 250 RPM causes a side reaction with a gaseous product to occur. This gaseous product may be responsible for the more 3-dimensional growth that is observed at slower rotation rates in Figure 4–8 (a), as it has been observed that hydrodynamic disturbances caused by evolving gas in the boundary layer can lead to outward growth.<sup>37</sup> FeCoMn films grown at 80 °C and 1000 RPM at various current densities had significantly different morphologies, exhibiting much rougher films with large 3-dimensional growth when deposited at current densities up to  $11 \text{ mA}\cdot\text{cm}^{-2}$ . At  $12 \text{ mA}\cdot\text{cm}^{-2}$  the growth features became smaller. At  $13 \text{ mA}\cdot\text{cm}^{-2}$ , the deposition potential was great enough to deposit Mn at overpotential, resulting in a much higher Mn content in the film. In this case, the morphology of the film changes, and appears similar to morphologies observed in pure Mn films deposited from this  $\text{ChCl-U}$ .<sup>23</sup>

The crystal structure of the deposited FeCo and FeCoMn films was studied by XRD, and representative diffractograms are presented in Figure 4–9. Strong peaks from the copper substrate are observed in all cases. In both types of alloys, the presence of peaks corresponding to the metal deposit seems to be dependent on film thickness, suggesting that non-equilibrium metal condensation during electrodeposition is not conducive to crystallite formation until a relatively thick deposit is obtained. Some of the thicker deposits did exhibit a weak peak at 45.8°, believed to emanate from the FeCo lattice. These peaks have been used to calculate mean FeCo grain size,  $D$ , according to the well-known Scherrer formula,  $D = K\lambda/\beta\cos\theta$ , where the crystallite shape factor  $K$  is taken as 0.9, the x-ray wavelength  $\lambda$  is 0.179 nm,  $\beta$  is the full width of the peak at half of the maximum value, in radians, and  $\theta$  is the diffraction angle.  $\beta$  has been corrected for an instrumental broadening of 0.3°. For FeCo and FeCoMn deposits where a peak was observed at 45.8°, the mean grain size is given in Tables 4–2 and 4–3. The films without any detectable peaks from the FeCo lattice are taken to be amorphous, although it is seen that most crystallites are less than 100 nm. It can be concluded that electrodeposition of FeCo under the conditions tested here are not conducive to large crystal formation. Annealing the samples under vacuum at temperatures up to 200 °C for 1 hour did not lead to enhanced crystallization in any case.

High impurity incorporation into deposits is a possibility during electrodeposition from DES. Indeed, high impurity content in the FeCo and FeCoMn may explain both the poor crystallinity, the lack of grain growth during annealing, and the high coercivity and highly variable magnetization of the films grown from this ChCl-U solvent. To test this hypothesis, EDS was performed on FeCo samples deposited under condition 3 (Table 4–1)

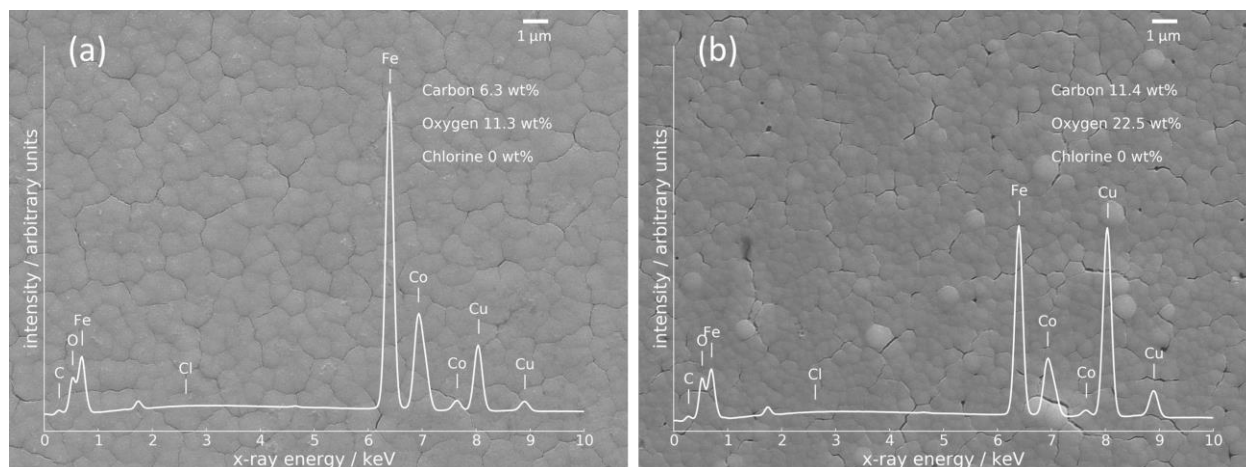


Figure 4–10. EDS spectra and determined impurity compositions of FeCo films deposited under Condition 3 as described in Table 4–1 at (a) -0.8 V and (b) -1.0 V, overlaid on top-down SEM micrographs of the films.

at -0.8 V and at -1.0 V, with results shown in Figure 4–10. These measurements reveal that both samples contain significant amounts of both carbon and oxygen, however no chlorine or nitrogen were detected. It is not known to what extent the detected oxygen is a result of incorporation during deposition, surface oxidation of the copper substrate, surface oxidation after deposition, or a combination thereof, however a relatively large amount of carbon (6.3 wt% and 11.4 wt%, respectively) found in both deposits indicates that impurities are certainly incorporated into the deposit by some mechanism during the electrodeposition process. The sample deposited at a greater overpotential sees nearly double the incorporation of both C and O impurities. Since the current efficiency is very high and is not seen (in Figure 4–2) to drop significantly between electrodeposition at -0.8 V and -1.0 V, impurities are likely incorporated through a physical adsorption process rather than an electrochemical process involving either the solvent or its decomposition products. Despite the varying degree of impurity incorporation, the surface morphology between the two deposits is not seen to change. The amount of C and O

incorporated into these deposits could certainly help to explain the poor crystallinity and magnetic properties of these films.

## **Conclusion**

Preliminary results on the electrochemical behavior of Fe and Co in ChCl-U have been reported. It is seen that this solvent brings the deposition potential of Fe and Co closer together than in aqueous solution, leading to easy alloy codeposition, and enabling easy control of deposit composition with the solution concentration. Ferromagnetic FeCo alloy films have been electrodeposited successfully, and various deposition conditions have been tested to determine the effect of temperature, mass transport, metal ion concentration in deposition solution, and potential on the resultant films. Manganese has also been incorporated by an underpotential deposition mechanism to form tertiary FeCoMn alloys. Large amounts of C and O impurities incorporated from the deposition bath hamper the crystallization of the alloy films. The magnetic properties of the deposited films have been determined; however, the magnetization is lower than generally expected for pure bulk FeCo or FeCoMn alloy, likely due to impurities and cracks in the film.

## **Acknowledgements**

The Research Grant Council (RGC) at the University of Alabama (UA) is acknowledged for support through a grant RG-14741. The authors would like to thank the University of Alabama Central Analytical Facility, College of Engineering Mechanical Shop, and Chemistry Glass Shop for their resources.

## **References**

1. Zhu, J.-G.; Zhu, X.; Tang, Y., Microwave Assisted Magnetic Recording. *IEEE Transactions on Magnetics* **2008**, *44* (1), 125-131.

2. Andricacos, P. C.; Robertson, N., Future directions in electroplated materials for thin-film recording heads. *IBM Journal of Research and Development* **1998**, *42* (5), 671-680.
3. Liao, S. H., Thin film core of Co-Fe-B alloy. Google Patents: 1992.
4. Hironaka, K.; Uedaira, S., Soft magnetic properties of Co-Fe-P and Co-Fe-Sn-P amorphous films formed by electroplating. *IEEE Transactions on Magnetics* **1990**, *26* (5), 2421-2423.
5. Liao, S.; Roberts, G.; Darr, E. In *Electrodeposited high Be CoFeCr thin films for high frequency recording applications*, Magnetics Conference, 1992. Digests of Intermag'92., International, IEEE: 1992; pp 348-348.
6. Liu, X.; Evans, P.; Zangari, G., Electrodeposited Co-Fe and Co-Fe-Ni Alloy Films For Magnetic Recording Write Heads. *IEEE TRANSACTIONS ON MAGNETICS* **2000**, *36* (5), 3479-3481.
7. Reddy, B. V.; Deevi, S. C.; Khanna, S. N., Magnetic properties of Al, V, Mn, and Ru impurities in Fe-Co alloys. *Journal of Applied Physics* **2003**, *93* (5), 2823-2827.
8. Liao, S., High moment CoFe thin films by electrodeposition. *IEEE Transactions on Magnetics* **1987**, *23* (5), 2981-2983.
9. Liu, X.; Zangari, G.; Shen, L., Electrodeposition of soft, high moment Co-Fe-Ni thin films. *Journal of Applied Physics* **2000**, *87* (9), 5410-5412.
10. Guo, J.; Guo, X.; Wang, S.; Zhang, Z.; Dong, J.; Peng, L.; Ding, W., Effects of glycine and current density on the mechanism of electrodeposition, composition and properties of Ni-Mn films prepared in ionic liquid. *Applied Surface Science* **2016**, *365*, 31-37.
11. Ganesan, S.; Prabhu, G.; Popov, B. N., Electrodeposition and characterization of Zn-Mn coatings for corrosion protection. *Surface and Coatings Technology* **2014**, *238*, 143-151.
12. Bernasconi, R.; Panzeri, G.; Accogli, A.; Liberale, F.; Nobili, L.; Magagnin, L., Electrodeposition from Deep Eutectic Solvents. In *Progress and Developments in Ionic Liquids*, Handy, S., Ed. InTech: Rijeka, 2017; p Ch. 11.

13. Panzeri, G.; Tresoldi, M.; Rinaldi, C.; Magagnin, L., Electrodeposition of Magnetic SmCo Films from Deep Eutectic Solvents and Choline Chloride-Ethylene Glycol Mixtures. *Journal of The Electrochemical Society* **2017**, *164* (13), D930-D933.
14. Endres, F.; Abbott, A. P.; MacFarlane, D. R., *Electrodeposition from Ionic Liquids*. Wiley-VCH: 2008.
15. Abbott, A. P.; Harris, R. C.; Hsieh, Y. T.; Ryder, K. S.; Sun, I. W., Aluminium electrodeposition under ambient conditions. *Physical Chemistry Chemical Physics* **2014**, *16* (28), 14675-14681.
16. Abbott, A. P.; El Ttaib, K.; Frisch, G.; McKenzie, K. J.; Ryder, K. S., Electrodeposition of copper composites from deep eutectic solvents based on choline chloride. *Physical Chemistry Chemical Physics* **2009**, *11* (21), 4269-4277.
17. Golgovici, F.; Catranguiu, A.-S.; Stoian, A. B.; Anicai, L.; Visan, T., Preparation of Copper Telluride Films by Co-Reduction of Cu(I) and Te(IV) Ions in Choline Chloride: Ethylene Glycol Ionic Liquid. *Journal of Electronic Materials* **2016**, *45* (7), 3629-3639.
18. Golgovici, F.; Visan, T., Electrochemical deposition of BiTe films from choline chloride-malonic acid mixture as ionic liquid. *Chalcogenide Lett.* **2012**, *9* (10), 427-434.
19. Yang, H. Y.; Guo, X. W.; Chen, X. B.; Wang, S. H.; Wu, G. H.; Ding, W. J.; Birbilis, N., On the electrodeposition of nickel-zinc alloys from a eutectic-based ionic liquid. *Electrochimica Acta* **2012**, *63*, 131-138.
20. Endres, F., Ionic Liquids: Solvents for the Electrodeposition of Metals and Semiconductors. *ChemPhysChem* **2002**, *3* (2), 144-154.
21. Shamsuri, A. A.; Abdullah, D. K., IONIC LIQUIDS: PREPARATIONS AND LIMITATIONS. *Makara Sains* **2010**, *14* (2), 101-106.
22. Simka, W.; Puszczczyk, D.; Nawrat, G., Electrodeposition of metals from non-aqueous solutions. *Electrochimica Acta* **2009**, *54* (23), 5307-5319.
23. Sides, W. D.; Huang, Q., Electrodeposition of manganese thin films on a rotating disk electrode from choline chloride/urea based ionic liquids. *Electrochimica Acta* **2018**, *266*, 185-192.

24. Osaka, T.; Takai, M.; Hayashi, K.; Sogawa, Y.; Ohashi, K.; Yasue, Y.; Saito, M.; Yamada, K., New soft magnetic CoNiFe plated films with high  $B_s = 2.0\text{-}2.1$  T. *IEEE transactions on magnetics* **1998**, *34* (4), 1432-1434.
25. Yadav, A.; Pandey, S., Densities and Viscosities of (Choline Chloride + Urea) Deep Eutectic Solvent and Its Aqueous Mixtures in the Temperature Range 293.15 K to 363.15 K. *Journal of Chemical & Engineering Data* **2014**, *59* (7), 2221-2229.
26. Du, C.; Zhao, B.; Chen, X.-B.; Birbilis, N.; Yang, H., Effect of water presence on choline chloride-2urea ionic liquid and coating platings from the hydrated ionic liquid. **2016**, *6*, 29225.
27. Vanýsek, P., Electrochemical Series. In *CRC Handbook of Chemistry and Physics*, 96th ed.; Haynes, W. M., Ed. CRC Press: Boca Raton, FL, 2015; pp 5.80-5.89.
28. Pourbaix, M., Atlas of electrochemical equilibria in aqueous solution. *NACE* **1974**, 307.
29. Abbott, A. P.; Frisch, G.; Gurman, S. J.; Hillman, A. R.; Hartley, J.; Holyoak, F.; Ryder, K. S., Ionometallurgy: designer redox properties for metal processing. *Chemical Communications* **2011**, *47* (36), 10031-10033.
30. Golgovici, F.; Cojocaru, A.; Nedelcu, M.; Visan, T., VOLTAMMETRIC AND IMPEDANCE STUDIES OF ELECTRODEPOSITION OF Te AND ITS BINARY COMPOUNDS WITH Bi AND Sb USING CHOLINE CHLORIDE - UREA BASED ELECTROLYTE. *Chalcogenide Lett.* **2009**, *6* (8), 323-333.
31. Lo, N.-C.; Chung, P.-C.; Chuang, W.-J.; Hsu, S. C. N.; Sun, I.-W.; Chen, P.-Y., Voltammetric Study and Electrodeposition of Ni(II)/Fe(II) in the Ionic Liquid 1-Butyl-1-Methylpyrrolidinium Dicyanamide. *Journal of The Electrochemical Society* **2016**, *163* (2), D9-D16.
32. Badea, M. L. M.; Cojocaru, A.; Anicai, L., ELECTRODE PROCESSES IN IONIC LIQUID SOLVENTS AS MIXTURES OF CHOLINE CHLORIDE WITH UREA, ETHYLENE GLYCOL OR MALONIC ACID. *UPB Sci. Bull. Series B* **2014**, *76*, 21-32.
33. Green, T. A.; Valverde, P.; Roy, S., Anodic Reactions and the Corrosion of Copper in Deep Eutectic Solvents. *Journal of The Electrochemical Society* **2018**, *165* (9), D313-D320.

34. Levich, V. G., *Physicochemical hydrodynamics*. Englewood Cliffs, N.J., Prentice-Hall: 1962.
35. Cooper, E. I.; Bonhôte, C.; Heidmann, J.; Hsu, Y.; Kern, P.; Lam, J. W.; Ramasubramanian, M.; Robertson, N.; Romankiw, L. T.; Xu, H., Recent developments in high-moment electroplated materials for recording heads. *IBM Journal of Research and Development* **2005**, *49* (1), 103-126.
36. Bozorth, R. M., Ferromagnetism. *Ferromagnetism*, by Richard M. Bozorth, pp. 992. ISBN 0-7803-1032-2. Wiley-VCH, August 1993. **1993**, 992.
37. Oppedisano, D. K.; Jones, L. A.; Junk, T.; Bhargava, S. K., Ruthenium Electrodeposition from Aqueous Solution at High Cathodic Overpotential. *Journal of The Electrochemical Society* **2014**, *161* (10), D489-D494.

## **CHAPTER 5. GRAIN GROWTH AND SUPERCONDUCTIVITY OF RHENIUM ELECTROPOSITED FROM WATER-IN-SALT ELECTROLYTES\***

### **Summary**

The superconductivity and grain growth of rhenium electrodeposited from a water-in-salt electrolyte has been studied. The use of water-in-salt electrolytes has been shown to decrease the rate of hydrogen evolution during cathodic electrodeposition of Re. Films are deposited with a highly disordered atomic structure, and as-deposited films exhibit superconductivity up to a temperature of 5.8 K. The effects of annealing on the film's crystal grain structure, impurity content, and superconductivity is examined. A reduction of the critical temperature of superconductivity is found to accompany crystal grain growth, however film thicknesses of less than 300 nm inhibit crystal grain growth, leading to a retention of the critical temperature upon annealing these thin films. A reduction of impurities in Re films is found to accompany annealing, and significant grain growth is found to proceed rapidly at temperatures of 220 °C in inert atmospheres, however the presence of hydrogen in the annealing atmosphere reduces the temperature necessary for grain growth.

### **Introduction**

Low temperature superconducting materials are becoming increasingly important in the electronics industry, particularly as quantum computing is scaled to increasing qubit

---

\* This chapter is being prepared for publication. W.D. Sides, E. Hassani, T.S. Oh, D.P. Pappas, Y. Hu, Q. Huang

counts and as Josephson junction based devices continue to be explored. These devices require superconducting materials for implementing logic circuits, and quantum computing systems additionally require superconducting materials to eliminate ohmic heating so thermal perturbation may be avoided and sub-Kelvin temperatures may be more sustainable within the operating environment. Additionally, materials with a superconducting critical temperature ( $T_c$ ) above the boiling point of helium, 4.2 K, become practical for a much wider set of uses in the scientific, industrial, and medical industries. Currently, superconductors made of niobium or its alloys with Sn or Ti are most commonly used, however are prone to oxidation and difficult to solder. Fabrication is typically performed either by billet extrusion and drawing for wiring, or by vacuum deposition methods for microdevices.<sup>1</sup> On the other hand, the superconducting metal rhenium can be much more convenient to work with. It is ductile and can be soldered or ultrasonically wire-bonded to. Its extremely high melting point of 3186 °C suggests a high resistance to electromigration and reliability in circuitry.<sup>2</sup> Re does not interdiffuse easily with many metals common in circuitry.<sup>3</sup> Moreover, Re can be electrodeposited from aqueous solutions – a process compatible with other electronics fabrication processes – and the resulting films have  $T_c$  of nearly 6 K.<sup>4-5</sup> This is above the boiling point of helium and also well above the intrinsic  $T_c$  of Re metal, which is 1.7 K.

The electrodeposition of Re occurs at a significant overpotential to hydrogen evolution. Hydrogen bubbles continuously form at the cathode during the electrodeposition process and pose a challenge for the reliable application of electroplating methods to the fabrication of functional Re films. Defects due to hydrogen embrittlement or hydrogen outgassing during deposition are manifested as cracks in the final film which

would likely be detrimental to a device's performance. Our early work has shown that it is possible to overcome this challenge by electrodepositing rhenium from a solution containing an ultra-high concentration of lithium chloride.<sup>6</sup> This type of solution is known as a water-in-salt electrolyte,<sup>7-11</sup> and is able to suppress hydrogen evolution during electrodeposition at hydrogen overpotentials.

The atomic structure of rhenium films has been closely related to their superconductivity, with disordered samples exhibiting higher  $T_c$  than highly crystalline ones.<sup>12-13</sup> Re films can crystallize at relatively mild temperatures, and their  $T_c$  can be significantly reduced as a result. This work characterized rhenium thin films grown via electrodeposition from a water-in-salt electrolyte, and evaluates the conditions under which these films experience crystal grain growth, as well as the effect grain growth has on the  $T_c$  of the material. Attention is paid to impurities incorporated into the film while electroplating from this electrolyte. Electrochemical studies of Re electrodeposition from water-in-salt electrolytes are also provided, and the effect of the hydrophobic cation tetrabutyl ammonium (TBA) has been investigated to achieve further suppression of hydrogen evolution.

## Methods

All electrochemical studies and electrodeposition were performed in solutions made up of 18.2 M $\Omega$ -cm water, 25 mM ammonium perrhenate(VII) (99%) sourced from Alfa Aesar, and 0.1 M ACS grade sulfuric acid. Water-in-salt electrolytes also contained 5 M lithium chloride (98%) from Alfa Aesar. Tetrabutylammonium hydrogen sulfate (98%) was sourced from Acros Organics. All electrochemical work was performed in a 3-compartment cell with a platinum foil counter electrode separated from the cathode by a glass frit and a

saturated calomel reference electrode (SCE) fixed in position through a Luggin capillary. All potentials reported in this work are with respect to the SCE. Electrochemical studies were performed on a 5 mm diameter Pt rotating disk electrode (RDE) supplied by Pine Research. A rotation rate of 400 RPM was maintained throughout all work to provide adequate agitation for any formed hydrogen bubbles to be rapidly swept away. Voltammetric sweeps were performed at a rate of  $100 \text{ mV}\cdot\text{s}^{-1}$ . Partial currents were measured by electroplating rhenium for 60 s, followed by immediate anodic stripping at 0.7 V in the same solution. The integrated stripping charge was used to calculate the amount of Re deposited using Faraday's law, assuming the Re cathodically deposits and anodically strips from/to the same oxidation state (VII), which will be briefly discussed in the following sections. This plating time was found to be suitably long to give a good signal-to-noise ratio and to allow neglect of any substrate interactions. Electrodeposited samples were made using pieces of a silicon wafer with gold strips as seed layers. These substrates were prepared by first thermally depositing a 50 nm layer of  $\text{SiO}_2$  onto a Si wafer. The wafer was then patterned using lithography to create a 1 mm by 10 mm strip connected to a 3 mm by 5 mm contact pad. A 10 nm layer of Ti followed by a 100 nm layer of Au was evaporated. The photoresist was lifted off, leaving the patterned substrates. These substrates were mounted onto a chuck rotating in the same way as the RDE. Electrical connection was made through a front contact pin to the pad. After deposition, a 20 nm layer of Au was sputtered onto the deposits to provide protection against ambient oxidation and humidity.

An Autolab 302N potentiostat with a frequency analyzer was used for all electrochemical work. Solution resistance was determined through electrochemical impedance spectroscopy, wherein a sinusoidal potential was applied with an RMS

amplitude of 10 mV and the frequency was sampled from 0.1 Hz to 100 kHz. The solution resistance was used to correct for ohmic voltage drop in results where indicated. Film thickness was measured using a KLA Alpha-Step D-500 stylus profilometer. Measurements spanned the entire width of the strip and were averaged over at least 3 points along the length of the strip. Sample resistance measurements were performed using a Quantum Design PPMS DynaCool, capable of reaching temperatures down to 1.8 K. A linear four-point probe method was used with contact made through aluminum wires wire-bonded to the samples. Current was held constant at 1 mA and probes were separated by approximately 2 mm. *Ex-situ* x-ray diffraction (XRD) was performed on a Bruker D8 Discover with GADDS and a Co K $\alpha$  x-ray source. *In-situ* XRD was performed during indicated annealing experiments using a home built x-ray diffractometer with a Cu K $\alpha$  x-ray source and a sample stage, where the ambient atmosphere and temperature are precisely controlled. The temperature ramp rate was 1 °C·min<sup>-1</sup>, and two 10 s diffractogram snapshots were taken every 10 °C. No correction was made for the temperature increase during the snapshots, which was less than 0.2 °C. Impurity content was measured with time-of-flight secondary ion mass spectrometry (SIMS) using an IONTOF TOF-SIMS IV equipped with a Bi cluster liquid metal ion source, which generated a pulsed 25 keV Bi<sub>3</sub><sup>+</sup> primary ion beam and sampled over an area of 65  $\mu$ m by 65  $\mu$ m. To obtain depth profiles, the sample was sputtered with a 3 keV Cs<sup>+</sup> ion beam over an area larger than the SIMS measurement area. Depth profiles were obtained by alternating between sputtering for 2 s at a rate of 0.9 nm·s<sup>-1</sup> and SIMS analysis for 1 s. The sputtering rate was calibrated with AFM profilometer measurement over the final crater.

## Results and Discussion

### Electrochemical behavior of rhenium deposition electrolytes

The use of water-in-salt electrolytes to reduce hydrogen evolution during the electrodeposition of rhenium has been documented in some early publications.<sup>5-6</sup> A decrease in proton reduction current, achieved by limiting the proton diffusion rate, has been shown when high concentrations of LiCl of 5 to 10 M are dissolved in solution.<sup>14</sup> This effect alleviates hydrogen embrittlement in growing Re films and achieves the elimination of pinholes and cracks in thin film deposits. Here a study is presented quantifying the effects that the addition of 5 M LiCl has on the Re deposition rate and proton reduction rate in a Re plating electrolyte consisting of 25 mM  $\text{NH}_4\text{ReO}_4$  and 0.1 M  $\text{H}_2\text{SO}_4$ . Figure 5-1 (a) presents the cathodic sweep of cyclic voltammograms (CVs) of the rhenium electrolyte both with 5 M LiCl (green line) and without LiCl (red line). Potentials were corrected for ohmic drop prior to plotting. As the potential is swept away from an open-circuit value in the cathodic direction, the proton reduction reaction occurs with fast kinetics beginning at -0.28 V and -0.21 V vs SCE in the additive-free and 5 M LiCl electrolytes respectively. This shift in the onset potential of proton reduction is notable and indicates that protons, complexed as hydronium ions, are present in a different chemical state in the water-in-salt electrolyte. The positive direction of this shift indicates the hydronium ions are more easily reduced to hydrogen gas. The  $\text{H}_2\text{O}$  to LiCl molar ratio in a 5 M LiCl solution is 9.6,<sup>5</sup> less than the amount necessary to completely fill the primary solvation sheaths of all  $\text{Li}^+$  and  $\text{Cl}^-$  ions. Studies have demonstrated that  $\text{Li}^+$  and  $\text{Cl}^-$  in concentrated solutions have water coordination numbers of 4.1 and 7.8, respectively.<sup>15-16</sup> These electrolytes cannot be assumed to behave similarly to dilute electrolytes – every water molecule is expected to

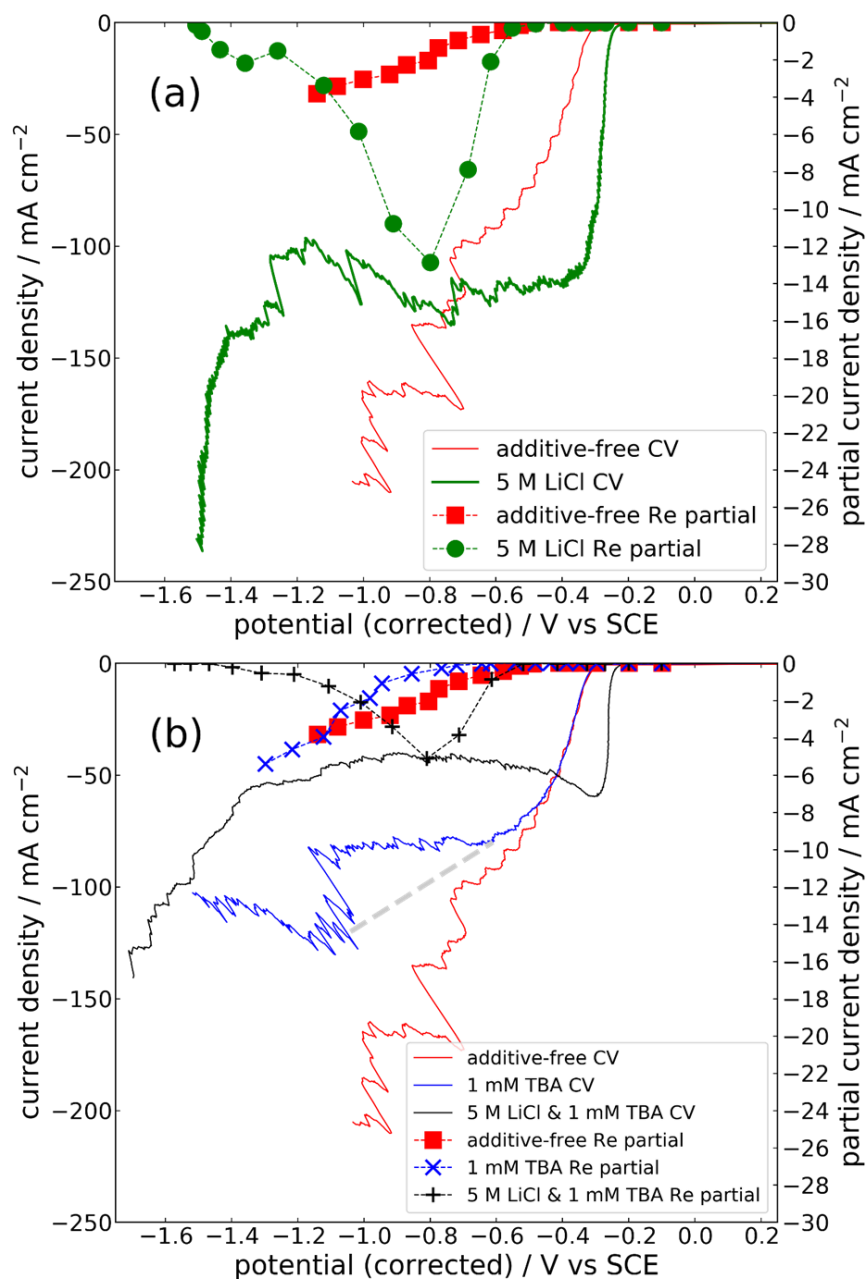


Figure 5-1. (a) Cyclic voltammograms showing partial currents (dashed lines with markers) and total currents (solid lines) of rhenium deposition on a Pt RDE at 400 RPM with and without 5 M LiCl; (b) Effects of TBA on the CVs and partial currents of rhenium deposition.

experience interactions with solute ions. In this case, the Lewis acidity of the Li<sup>+</sup> ions either in the solution or adsorbed on the electrode surface are believed to weaken the O-H<sup>+</sup> bonds

in hydronium ions, promoting the acidity of hydronium and making proton reduction more thermodynamically favorable.

Although the thermodynamics and reaction kinetics of hydrogen evolution seem to be shifted favorably in the water-in-salt electrolyte, the CV experiments reveal a mass transport limitation of the proton reduction reaction which establishes a limiting current at -0.35 V, at which point the current does not significantly increase until water reduction begins at -1.4 V. Mass transport of protons to the electrode surface is limited in the presence of concentrated LiCl by the disruption of the extensive hydrogen-bonding network which normally allows for fast proton diffusion in water through the Grotthuss mechanism.<sup>17-18</sup> Due to this mass transport limitation, the current corresponding to hydrogen evolution is limited to  $120 \text{ mA}\cdot\text{cm}^{-2}$  throughout the potential region where Re deposition occurs. In the electrolyte without LiCl, no such limitation of hydrogen evolution occurs, so despite the less favorable reaction kinetics and thermodynamics, LiCl free electrolytes exhibit greater hydrogen evolution beyond -0.7 V.

Rhenium deposition begins at -0.53 V. Concerning this reaction, a stark difference is also observed between the traditional electrolyte and the water-in-salt electrolyte. The onset potential does not change, indicating that Re is present in the same chemical state in both solutions. However, the kinetics of the Re deposition reaction are much faster in the water-in-salt electrolyte. Re deposits over 6 times faster in the water-in-salt electrolyte at -0.8 V, where the total current, including hydrogen evolution, is equal between the two solutions. In other words, this water-in-salt electrolyte can achieve over an 80% reduction in hydrogen evolved during rhenium plating on a thickness basis. Partial currents are calculated based on an assumption that Re oxidizes to the same oxidation state (VII) from

which it was initially reduced. If it were to have oxidized to a less positive state, the partial currents calculated would be an under approximation. However, potentiostatic rhenium depositions on Au strip substrates used for fabricating samples for material characterization later in this study allow for a direct thickness measurement with a profilometer. By using Faraday's laws of electrolysis, the Re deposition partial current was calculated and is exhibited in Figure S 5-1, which is approximately equal to the values obtained from anodic stripping. From these calculations, it is confirmed that the stripping analysis method does not give a significant underapproximation of the partial current, suggesting that Re does oxidize primarily to Re(VII).

It is interesting to note that in the presence of concentrated LiCl, there is a gradual reduction in the Re deposition rate once cathodic potentials are held below -0.9 V, and once the potential is held at -1.5 or beyond, no Re deposit is found on the electrode. No such behavior is observed in the solution lacking LiCl. The phenomena resulting in decreased Re deposition at more negative potentials in LiCl containing solutions are not fully understood, but may include a number of causes. Our group has recently discovered that copper deposition in a similar water-in-salt electrolyte comes to a halt upon reaching the onset potential of water reduction,<sup>14</sup> and has attributed this to the formation of insoluble and non-conducting lithium hydroxides on the cathode surface.<sup>19</sup> While this mechanism likely explains the halting of Re deposition we have observed at -1.5 V, it does not seem to adequately explain the gradual decrease in the Re deposition rate beginning at -0.8 V, as water reduction is not occurring here and so there should not be sufficient quantities of hydroxide near the cathode to form a passivating layer. Our group has also previously noted a similar behavior for Re deposition in water-in-salt electrolyte, and has attributed it

to the formation of the soluble rhenide ion at sufficiently negative potentials, decreasing the amount of metallic rhenium deposited during potentiostatic holds beyond a potential of -0.8 V.<sup>6</sup> Here we note that a decrease in the rhenium partial current prior to water reduction occurs only in the presence of concentrated Li<sup>+</sup> and Cl<sup>-</sup>, indicating that one of these species is required to attain a negative oxidation state of rhenium. We therefore postulate the formation of a soluble rhenide complexed with, at a minimum, the lithium cation. The existence of an aqueous rhenide has been the subject of an interesting debate in the past, and although aqueous Re(-I) is not generally considered stable, such negative potentials could favor its formation as an intermediate to an alkali metal rhenium hydride.<sup>20-23</sup> Further studies would certainly be necessary to elucidate the existence and nature of this ion, or any other causes of diminished Re deposition in the -0.8 to -1.5 V range.

In the vein of further reducing hydrogen evolution during the electrodeposition of Re, the use of the hydrophobic cation TBA has been evaluated. TBA has been observed to adsorb onto negatively biased electrode surfaces and, due to its hydrophobic nature, block water molecules from subsequently accessing the surface.<sup>19</sup> Upon the addition of 1 mM TBA to the Re plating solution, a decrease in both the total current and the Re partial current is observed during potential sweep experiments as shown in Figure 5-1 (b). While the TBA cation suppresses the hydrogen evolution, it proportionally suppresses the Re deposition reaction. Upon first glance, it appears as though a proton reduction limiting current of 80 mA·cm<sup>-2</sup> is established at -0.61 V induced solely by the blocking effects of 1 mM TBA. This behavior would be unexpected for an interface effect as proposed here. Further inspection reveals that the horizontal portion of the CV between -0.61 V and -1 V is

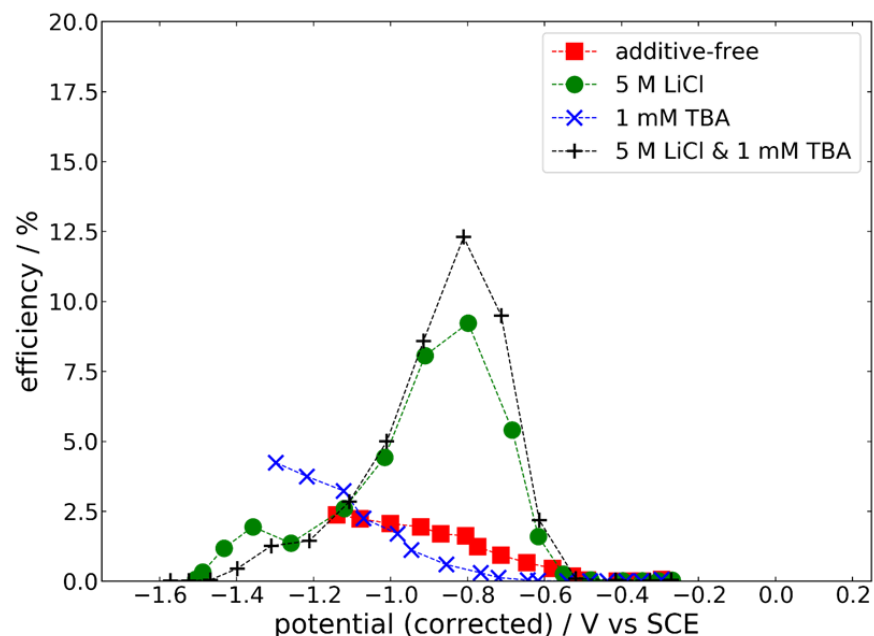


Figure 5-2. Current efficiencies of rhenium deposition with various solution additives. likely not due to a limiting current, but rather is an artefact of hydrogen bubbles forming and effectively reducing the surface area of the working electrode. The jump to higher current density at -1.05 V results from such a bubble becoming displaced by the rotation. If the peak current measured at this point is used to interpolate a typical kinetics-controlled current-potential dependence, as shown by the dashed grey line in Figure 5-1 (b), it becomes clear that there is a potential dependent slow-down in the kinetics of the proton reduction reaction that becomes stronger as the electrode potential becomes more negative. This is consistent with the expectation that the TBA cation adsorbs more strongly to the electrode surface at more negative potentials.

Notably, in combining the hydrogen evolution suppressing effects of TBA with the proton mass transport limiting effects of LiCl, the result is up to an 80% decrease in total current versus the additive-free Re plating solution, with the decrease caused overwhelmingly by a reduction in hydrogen evolution current. As seen in Figure 5-2, the

maximum current efficiency attainable in a water-in-salt electrolyte is 3 percentage points higher when TBA is utilized. Therefore, it becomes possible to deposit Re at an efficiency of over 12% in our electrolyte, a 5X improvement over the additive-free electrolyte.

### **Superconductivity and grain structure of electrodeposited rhenium**

The  $T_c$  of superconducting films is critical for implementation in devices. Films with greater  $T_c$  values are generally favored as they exhibit superconductivity at more achievable temperatures. Films with a  $T_c$  above 4.2 K can be superconductive using liquid helium cryogenic systems, although films with a lower  $T_c$  are still useful in quantum computing as these systems operate well below 4.2 K. Films of varying thicknesses from 90 to 850 nm were cathodically electrodeposited from water-in-salt electrolytes. The resistive  $T_c$  of these films, seen in Figure 5–3 (a), ranged from 4 K to 5.6 K, with typical transition widths of 0.2 to 0.4 K. Although crystalline Re has a  $T_c$  of 1.7 K,<sup>12, 24-25</sup> electrodeposited Re has been found by Pappas *et al.* to have a  $T_c$  of up to 6 K when fabricated as stacked multilayers with Au,<sup>4</sup> and we have achieved similar values for single Re layers, over a wide range of thicknesses, deposited from a water-in-salt electrolyte. We attribute the elevated  $T_c$  values to the highly disordered atomic structure of electrodeposited Re films. Indeed, amorphous films of Re have been reported to have a  $T_c$  of up to 7 K.<sup>13</sup> Electrodeposition is a non-equilibrium process and therefore often deposits films in a metastable, disordered fashion. The crystal nature of our films has been studied by XRD, presented in Figure 5–4. Regardless of the thickness, the as-deposited films do not exhibit any XRD peaks corresponding to Re crystal structure. The peaks observed can be assigned to the crystal structure of Au from the seed and cap. This indicates that Re is present in our films in a

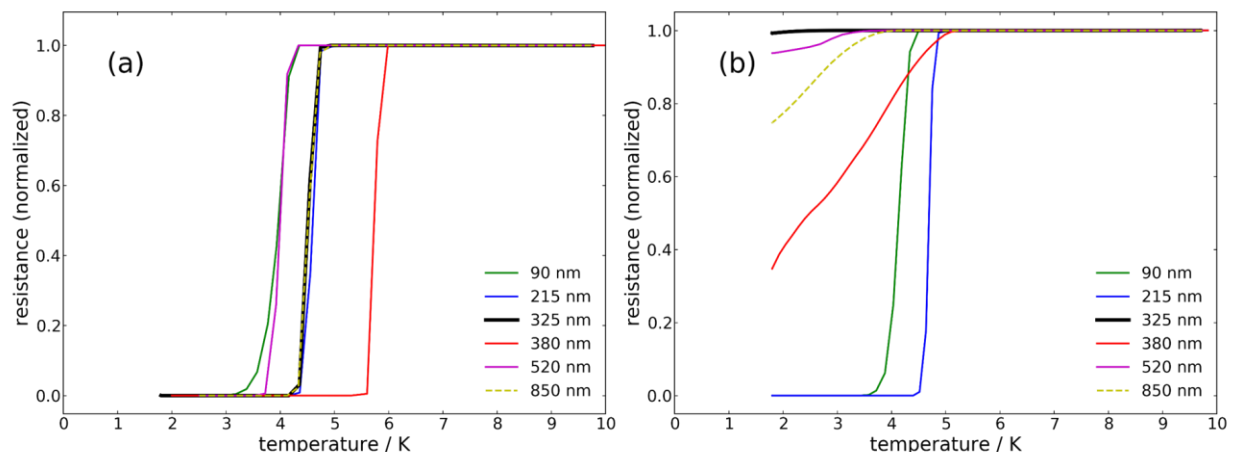


Figure 5–3. Resistances of Re films (a) as-deposited from water-in-salt electrolyte and (b) after annealing at 200-225 °C under vacuum.

nano-crystalline or amorphous state. No differences in the diffractograms were observed after several weeks, suggesting the Re thin films do not crystallize at room temperature.

To further elucidate any correlation between crystallinity and superconductivity, annealing was performed for 30 min in a vacuum furnace operated at 200 °C. It should be noted that the temperature controller in this furnace allowed an initial temperature overshoot of up to 25 °C, meaning that annealing temperatures briefly reached up to 225 °C before stabilizing to 200 °C. The crystallization behavior was seen to be highly dependent on the film thickness, as seen in Figure 5–4. Films 325 nm thick and thicker experienced significant grain growth in all directions, however it is seen by comparing the relative peak intensities to those for a powder sample (Figure S 5–2) that the grain growth significantly favors the *c* direction. The thinner films experienced very little grain growth. The little crystal structure observed in the annealed 90 and 215 nm films was exclusively in the *c* direction. This indicates that grain growth of Re films can be largely inhibited due to pinning by the adjacent metal layers if the Re layer is kept sufficiently thin. Similar behavior is well-known for electrodeposited copper, where films with thicknesses of

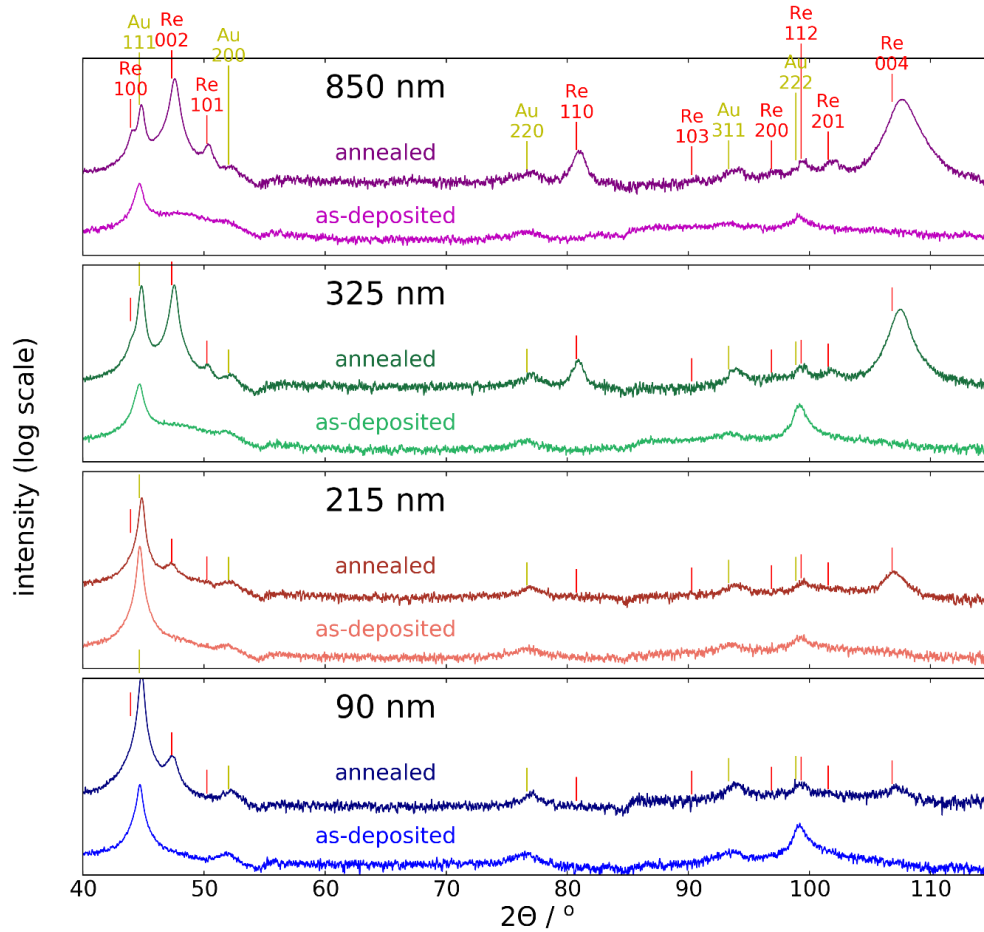


Figure 5-4. X-ray diffractograms of selected Re films as-deposited and after vacuum annealing at 200 °C for 30 minutes.

250 nm or less, or constrained within trenches of similar dimensions, are found to undergo significantly more sluggish crystal grain growth during annealing.<sup>26-27</sup> Upon measuring the  $T_c$  of the annealed Re films, presented in Figure 5-3 (b), it was confirmed that atomic structure was highly correlated to superconductivity. After annealing, the films that were 325 nm or thicker, which had been observed by XRD to have undergone significant grain growth, no longer exhibited superconductivity above 1.8 K, the minimum temperature our measurements were capable of achieving. In contrast, the 90 and 215 nm films which remained highly disordered upon annealing exhibited virtually no change in the  $T_c$  upon

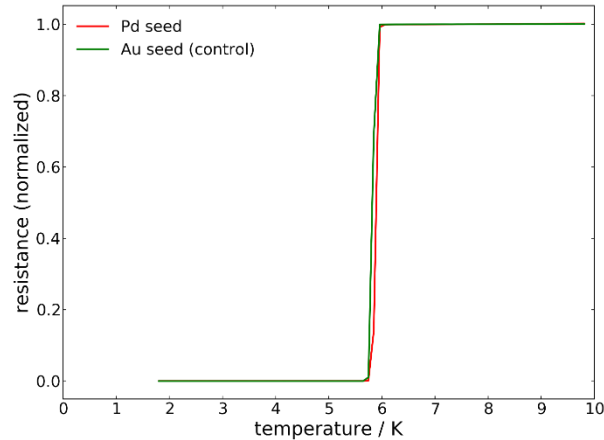


Figure 5–5. Resistances of Re films deposited on Au or Pd seed layers.

annealing, indicating that the disordered atomic structure is responsible for the elevated  $T_c$  observed in electrodeposited Re. Further, this indicates that  $c$  direction grain growth may not impede superconductivity, however grain growth in the  $a$  and  $b$  directions significantly reduces the  $T_c$ . The beneficial effect of maintaining film thicknesses less than some critical value between 215 and 325 nm points to a possible strategy of using layers of thin electrodeposited Re as a means to stabilize the disordered atomic structure of superconducting Re lines.

To ensure the elevated  $T_c$  observed is not due to an effect of the interface between the Au and Re layers, a sample was deposited onto the same strip patterned substrate, but with a Pd seed as opposed to Au, with no protective Au layer deposited. Figure 5–5 shows that this sample, having a 440 nm layer of Re, and a 680 nm sample deposited in the same batch on the Au substrate as a control, have identical  $T_c$  values. It can therefore be concluded that the superconductivity of our films arises from the bulk of the Re deposit, and is not affected by the interface with other metal layers.

The temperature at which crystallization of Re occurs was determined more precisely by taking *in-situ* XRD measurements during annealing as the temperature was

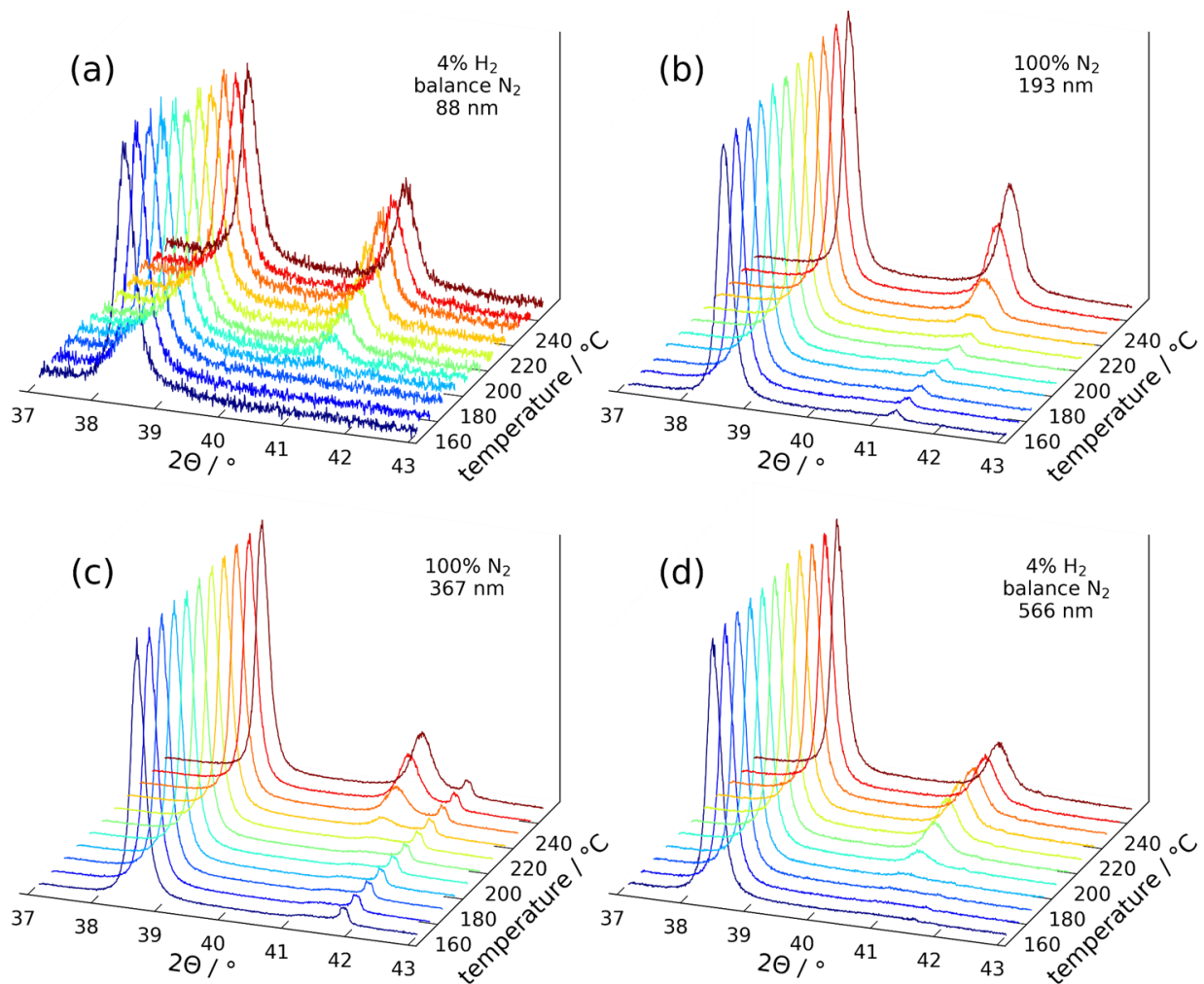


Figure 5-6. X-ray diffractograms of Re films of the indicated thicknesses taken *in-situ* during annealing in various atmospheres as indicated, plotted on a linear scale. Peaks at 38.2° correspond to the Au (111) lattice, and peaks at 40.5° correspond to the Re (002) lattice. The higher angle peak in (c) is believed to result from surface contamination.

slowly ramped up. The effects the annealing atmosphere had on the annealing process were also studied. The resulting diffractograms are plotted in Figure 5-6. A narrow  $2\theta$  range was selected that covers only the Au(111) peak and the Re(002) peak, as these peaks appear in annealed samples of every thickness previously studied. In both the 193 and 367 nm films, which were annealed in 100% N<sub>2</sub>, (Figure 5-6 (b) and (c), respectively), the Re(002) peak does not emerge until the temperature reaches 220 °C. A small peak of constant height observed across all temperatures in Figure 5-6 (c) was believed to result

from surface contamination. The films annealed with 4% H<sub>2</sub> (Figure 5–6 (a) and (d), 88 and 566 nm, respectively) had emergent Re(002) peaks much earlier at 190 °C. The difference in grain growth behavior may be attributable to hydrogen gas acting to reduce oxides present along the grain boundaries. If oxides are present along the grain boundaries, they could pin the grains and inhibit growth until higher temperatures. Hydrogen could act to reduce these oxides, allowing the crystal grains to grow at lower temperatures.

### **Impurity analysis of water-in-salt deposited Re**

When electrodepositing metals from a high-chloride solution, the incorporation of chloride into the deposit becomes a concern due to the ion's strong affinity for adsorption onto metal surfaces. In some cases, chloride and other impurities incorporated into metal films have an inhibiting effect on crystal grain growth within the film.<sup>27</sup> As previously discussed, inhibition of grain growth in Re films is beneficial for superconductor applications where maintaining a high  $T_c$  is desired. On the other hand, alkali metal contamination is a major concern in semiconductor devices and fabrication facilities. Although the use of water-in-salt electrolyte did not affect the  $T_c$  of our as-deposited films when compared to films deposited from a traditional Re electrolyte, the impurity content was studied to determine which impurities were incorporated into the deposit and how annealing affects them. Depth profiling SIMS was performed on samples containing approximately 500 nm thick Re films deposited from water-in-salt electrolyte, both before and after annealing at 200 °C for 30 minutes. Results, shown in Figure 5–7, have been scaled using the intensity of silicon in the silicon layer as a reference to avoid variation of the detector yield across samples. Although SIMS results are not quantitative, these measurements provide a good understanding of the changes in impurity content during the

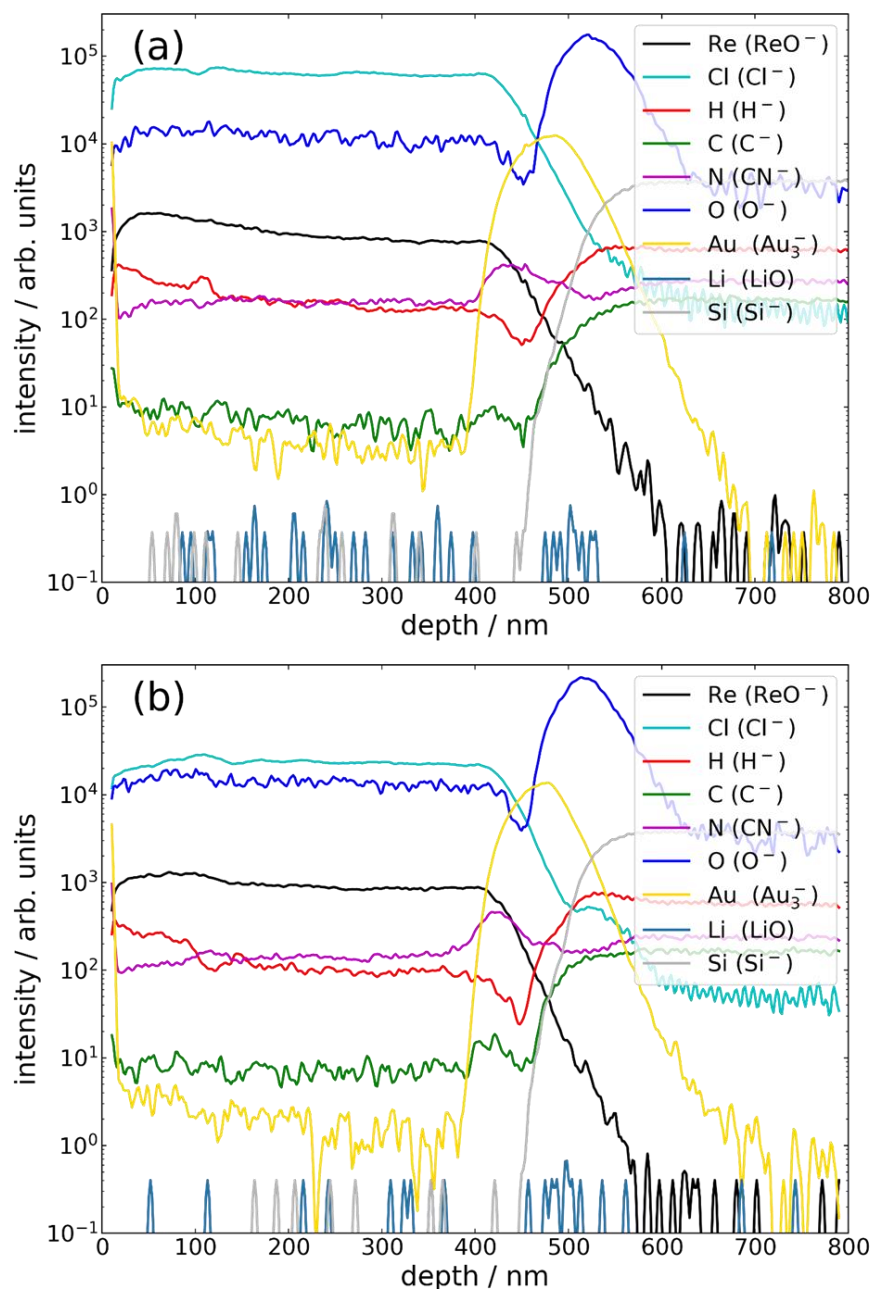


Figure 5-7. SIMS depth profiles showing impurity content of Re films electrodeposited from water-in-salt electrolyte (a) as-deposited and (b) annealed for 30 min at 200 °C. Lower depth values correspond to the Re film, and higher depth values the Au seed/Si substrate.

annealing and crystallization process. SIMS indicated the presence of Cl, O, H, and N within the deposited Re layer, with a less significant amount of C. Upon annealing at 200 °C for 30 minutes in a  $\text{N}_2$  atmosphere, however, a significant reduction in most impurities was

observed, as summarized in Table 5–1. The chlorine content was reduced by 63 %, while the hydrogen content was reduced by 28 %. On the other hand, the oxygen content was found to very slightly increase during annealing. Lithium was not detected above measurement noise levels in either sample.

Table 5–1. Change in SIMS detection intensity of impurity elements in Re upon annealing.

Element	Change upon Annealing
Carbon	no change
Chlorine	-63%
Hydrogen	-28%
Nitrogen	-13%
Oxygen	+16%

## Conclusion

The use of water-in-salt electrolytes for electrodepositing Re has been shown to reduce simultaneous hydrogen evolution, enabling deposition at higher rates and current efficiencies. The additive tetrabutylammonium has been shown to further reduce the hydrogen evolution rate during Re electrodeposition, however, to also suppress the Re deposition rate. A variety of thicknesses of Re thin films have been deposited, which exhibit superconductivity up to 5.6 K. This elevated  $T_c$  value has been attributed to the disordered atomic structure of the deposits achieved by electrodeposition. Grain growth has been shown to deteriorate the  $T_c$  of Re films, however grain growth during annealing can be inhibited if the Re layers are sufficiently thin. Hydrogen present in the annealing atmosphere has been shown to accelerate grain growth, allowing crystallization to occur at reduced temperatures. Chlorine and hydrogen are incorporated as impurities into Re films during deposition, however their content in films is reduced by annealing.

## Acknowledgements

The Center for Materials for Information Technology at The University of Alabama, the Central Analytical Facility, and Dr. Jair Lizarazo-Adarme are acknowledged for instrument training and support.

## References

1. Ozeryansky, G., Method of production for multifilament niobium-tin superconductors. Google Patents: 1992.
2. Adelman, C.; Gong Wen, L.; Peter, A.; Kong Siew, Y.; Croes, K.; Swerts, J.; Popovici, M.; Sankaran, K.; Pourtois, G.; Van Elshocht, S.; Bömmels, J.; Tokei, Z., *Alternative metals for advanced interconnects*. 2014; p 173-176.
3. Ghasemi, R.; Valefi, Z., Electrodeposition of rhenium-base layer as a diffusion barrier between the NiCoCrAlY coating and a Ni-based superalloy. *Journal of Alloys and Compounds* **2018**, *732*, 470-485.
4. Pappas, D. P.; David, D. E.; Lake, R. E.; Bal, M.; Goldfarb, R. B.; Hite, D. A.; Kim, E.; Ku, H. S.; Long, J. L.; McRae, C. R. H.; Pappas, L. D.; Roshko, A.; Wen, J. G.; Plourde, B. L. T.; Arslan, I.; Wu, X., Enhanced superconducting transition temperature in electroplated rhenium. *Applied Physics Letters* **2018**, *112* (18), 182601.
5. Huang, Q.; Hu, Y., Electrodeposition of Superconducting Rhenium with Water-in-Salt Electrolyte. *Journal of The Electrochemical Society* **2018**, *165* (16), D796-D801.
6. Huang, Q.; Lyons, T. W., Electrodeposition of rhenium with suppressed hydrogen evolution from water-in-salt electrolyte. *Electrochemistry Communications* **2018**, *93*, 53-56.
7. Dubouis, N.; Lemaire, P.; Mirvaux, B.; Salager, E.; Deschamps, M.; Grimaud, A., The role of the hydrogen evolution reaction in the solid–electrolyte interphase formation mechanism for “Water-in-Salt” electrolytes. *Energy & Environmental Science* **2018**, *11* (12), 3491-3499.
8. Bin, D.; Wang, F.; Tamirat, A. G.; Suo, L.; Wang, Y.; Wang, C.; Xia, Y., Progress in Aqueous Rechargeable Sodium-Ion Batteries. *Advanced Energy Materials* **2018**, *8* (17), 1703008.

9. Kühnel, R.-S.; Reber, D.; Remhof, A.; Figi, R.; Bleiner, D.; Battaglia, C., "Water-in-salt" electrolytes enable the use of cost-effective aluminum current collectors for aqueous high-voltage batteries. *Chemical Communications* **2016**, 52 (68), 10435-10438.
10. Suo, L.; Borodin, O.; Gao, T.; Olguin, M.; Ho, J.; Fan, X.; Luo, C.; Wang, C.; Xu, K., "Water-in-salt" electrolyte enables high-voltage aqueous lithium-ion chemistries. *Science* **2015**, 350 (6263), 938.
11. Suo, L.; Hu, Y.-S.; Li, H.; Armand, M.; Chen, L., A new class of Solvent-in-Salt electrolyte for high-energy rechargeable metallic lithium batteries. *Nat. Commun.* **2013**, 4, 1481.
12. Hulm, J. K.; Goodman, B. B., Superconducting Properties of Rhenium, Ruthenium, and Osmium. *Physical Review* **1957**, 106 (4), 659-671.
13. ul. Haq, A.; Meyer, O., Superconducting and electrical properties of rhenium nitride and amorphous rhenium prepared by ion implantation. *Journal of Low Temperature Physics* **1983**, 50 (1), 123-133.
14. De, S.; White, J.; Brusuelas, T.; Patton, C.; Koh, A.; Huang, Q., Electrochemical Behavior of Protons and Cupric Ions in Water in Salt Electrolytes with Alkaline Metal Chloride. *in preparation* **2019**.
15. Bouazizi, S.; Nasr, S.; Jaïdane, N.; Bellissent-Funel, M.-C., Local Order in Aqueous NaCl Solutions and Pure Water: X-ray Scattering and Molecular Dynamics Simulations Study. *The Journal of Physical Chemistry B* **2006**, 110 (46), 23515-23523.
16. Yamaguchi, T.; Ohzono, H.; Yamagami, M.; Yamanaka, K.; Yoshida, K.; Wakita, H., Ion hydration in aqueous solutions of lithium chloride, nickel chloride, and caesium chloride in ambient to supercritical water. *J. Mol. Liq.* **2010**, 153, 2-8.
17. Sun, Q., Raman spectroscopic study of the effects of dissolved NaCl on water structure. *Vibrational Spectroscopy* **2012**, 62, 110-114.
18. de Grotthuss, T., *Mémoire sur la décomposition de l'eau et des corps qu'elle tient en dissolution à l'aide de l'électricité galvanique.* 1805.

19. Dubouis, N.; Serva, A.; Salager, E.; Deschamps, M.; Salanne, M.; Grimaud, A., The Fate of Water at the Electrochemical Interfaces: Electrochemical Behavior of Free Water Versus Coordinating Water. *The journal of physical chemistry letters* **2018**, *9* (23), 6683-6688.
20. Fergusson, J. E., Recent advances in the coordination chemistry of rhenium. *Coordination Chemistry Reviews* **1966**, *1* (4), 459-503.
21. Abrahams, S.; Ginsberg, A.; Knox, K., Transition metal-hydrogen compounds. II. The crystal and molecular structure of potassium rhenium hydride, K<sub>2</sub>ReH<sub>9</sub>. *Inorganic Chemistry* **1964**, *3* (4), 558-567.
22. Woolf, A., An outline of rhenium chemistry. *Quarterly Reviews, Chemical Society* **1961**, *15* (3), 372-391.
23. Cobble, J., On the structure of the rhenide ion. *The Journal of Physical Chemistry* **1957**, *61* (6), 727-729.
24. Daunt, J. G.; Smith, T. S., Superconductivity of Rhenium. *Physical Review* **1952**, *88* (2), 309-311.
25. Eisenstein, J., Superconducting Elements. *Reviews of Modern Physics* **1954**, *26* (3), 277-291.
26. Harper, J.; Cabral Jr, C.; Andricacos, P.; Gignac, L.; Noyan, I.; Rodbell, K.; Hu, C., Mechanisms for microstructure evolution in electroplated copper thin films near room temperature. *Journal of applied physics* **1999**, *86* (5), 2516-2525.
27. Reid, J., Damascene Copper Electroplating. In *Handbook of Semiconductor Manufacturing Technology*, 2nd ed.; Doering, R.; Nishi, Y., Eds. CRC Press: Boca Raton, FL, 2008; pp 16.01-16.47.

## Supplementary Information

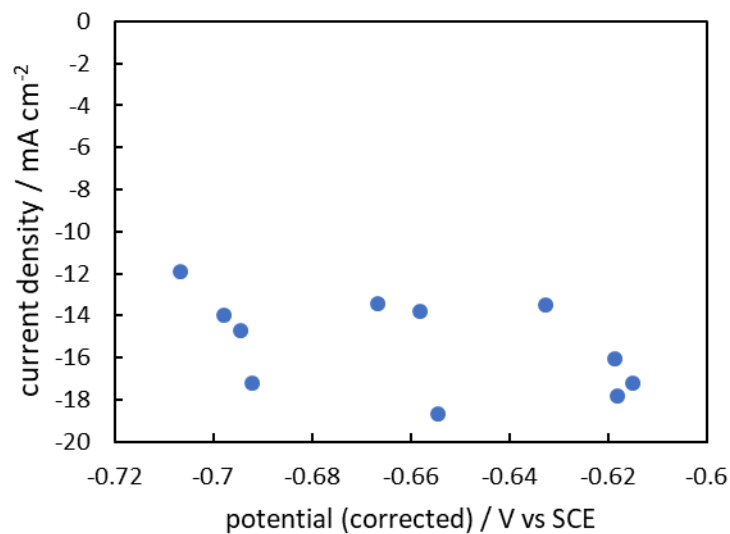


Figure S 5–1. Rhenium deposition partial current densities from potentiostatic Re depositions on Au strip substrates used throughout this study for material characterization. Partial currents calculated from the measured film thickness using Faraday's law and assuming a Re density of  $21.02 \text{ g}\cdot\text{cm}^{-3}$ .

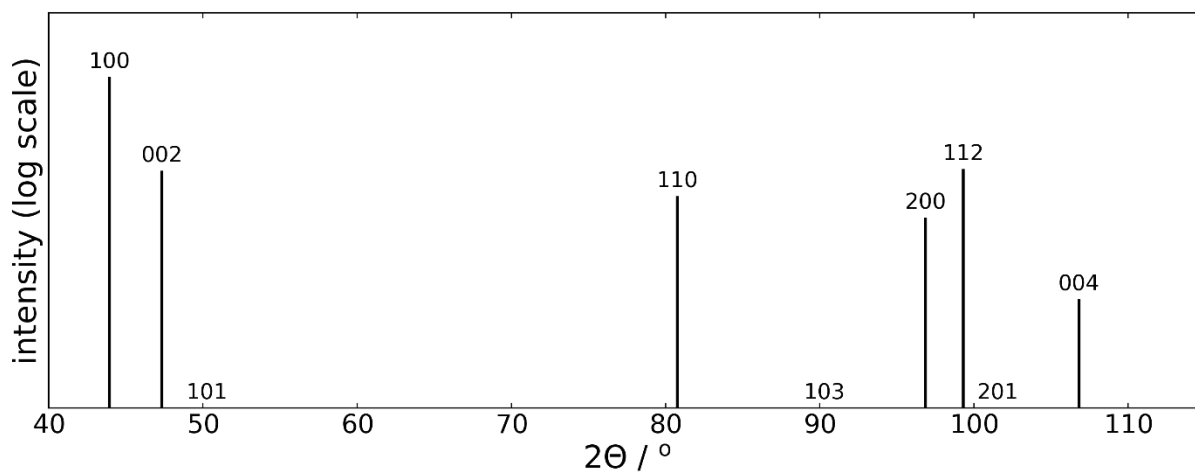


Figure S 5–2. Calculated x-ray diffractogram of an ideal Re powder sample showing peak locations

## **CHAPTER 6. RUTHENIUM ELECTRODEPOSITION FROM WATER-IN-SALT ELECTROLYTES FOR INTERCONNECT APPLICATIONS AND THE INFLUENCE OF TETRABUYTLAMMONIUM\***

### **Summary**

The use of water-in-salt electrolytes is evaluated for the electrodeposition of metallic ruthenium. The mechanisms of proton reduction inhibition by concentrated LiCl and dilute tetrabutylammonium is evaluated. Concentrated LiCl is found to disrupt the hydrogen bonding network within the solution bulk, whereas TBA is found to adsorb onto the electrode surface, blocking proton access. Ruthenium exists as a different complexed species in water-in-salt electrolytes versus dilute aqueous electrolytes, leading to a -300 mV shift in the deposition onset potential. Greater current efficiencies of Ru deposition can be obtained when depositing at proton overpotentials by the use of water-in-salt electrolytes, and TBA can offer further improvements. The grain structure and resistivities of Ru thin films are studied.

### **Introduction**

As microchip interconnect dimensions continue to scale down, the use of electroplated copper as the interconnect material faces challenges due to its exponentially increasing resistance as trench dimensions narrow. This limitation has resulted in a need to develop damascene processes suitable for metallization with alternate metals that perform better in small trench dimensions. Ruthenium has been identified as a promising candidate

---

\*This chapter is being prepared for publication. W.D. Sides, Q. Huang.

to fill this need.<sup>1</sup> Its shorter electron inelastic mean free path versus copper indicates it will not be as susceptible to resistance increases as dimensions narrow.<sup>2-3</sup> Additionally, Ru has been shown to have superior robustness against both oxidation and electromigration, one of the primary modes of interconnect failure.<sup>4</sup> Perhaps equally as importantly, Ru is stable when in direct contact with the dielectric surrounding the trench, eliminating the need for the diffusion barrier typically implemented in copper interconnects. Barrierless Ru interconnects allow the entire cross section of the trench to be occupied by conductor, providing a much more efficient use of space, particularly as trench widths come well within an order of magnitude of the typical diffusion barrier width.<sup>5</sup> Recently, explorations into the use of ruthenium for interconnect applications have primarily employed chemical vapor deposition methods.<sup>4</sup> While results have indeed demonstrated excellent potential, the use of CVD presents challenges in terms of achievable film purity and growth rates.

A Ru electrodeposition process analogous to the ubiquitous process for copper damascene metallization would certainly be a significant achievement toward enabling the deployment of Ru based interconnect technology. Electrochemical deposition of Ru has proven challenging, owing to its high nobility. As such, suitable complexing agents are needed to stabilize the Ru(III) cation in solution. The electrodeposition of such complexed ions requires highly negative cathodic potentials, resulting in operation at an overpotential to hydrogen evolution.<sup>6</sup> The resulting low current efficiency inevitably causes hydrogen embrittlement and can cause cracking to occur in films. Commercial Ru electroplating methods also call for bath temperatures to be elevated to up to 80 °C to improve current efficiencies<sup>7</sup> – an impractical condition for most wafer fabrication tools.

Water-in-salt electrolytes (WiSE) have recently emerged as a promising tool to decrease the amount of hydrogen evolved during metal electrodeposition at overpotentials to proton reduction.<sup>8-10</sup> Recently receiving significant attention from the lithium ion battery field as a solvent to enable high voltage aqueous batteries, WiSE contain extremely high concentrations of salt, such as LiCl.<sup>11-14</sup> The concentration of salt is high enough that every water molecule is contained within the primary solvation sheath of a solute ion, hence the name water-in-salt. The use of WiSE allows the formation of a mass transport limiting current of the hydrogen evolution reaction (HER), which enables metal deposition at potentials significantly negative to the onset of the HER while maintaining reasonable current efficiencies. Our group has shown that this is due to a significant decrease of the proton diffusion coefficient in WiSE.<sup>8</sup> Concentrated alkaline metal cations disrupt the extensive hydrogen bond network which, in dilute solutions, allows for extremely fast proton diffusion.<sup>15</sup> Here, we describe efforts to implement a WiSE for the electrodeposition of ruthenium. The electrochemical behavior of the system is studied, and electroplated Ru films are characterized with an emphasis on crystal structure and resistivity of the deposited films.

The hydrophobic cation tetrabutylammonium (TBA) has been shown to block water molecules from accessing the cathode surface in organic solvents, preventing water reduction.<sup>16</sup> Chapter 5 has demonstrated the ability of TBA to suppress the HER during metal deposition at hydrogen overpotentials, in both WiSE and dilute electrolytes.<sup>17</sup> This chapter will attempt to elucidate the mechanism of suppression and examine its effects on Ru deposition.

## Methods

All electrolytes were made up of 18.2 MΩ·cm water and 0.1 M ACS grade H<sub>2</sub>SO<sub>4</sub>. WiSE also contained 5 M LiCl (98%) from Alfa Aesar. Tetrabutylammonium hydrogen sulfate (98%) was sourced from Acros Organics. Electrolytes for metal deposition contained 25 mM hydrated RuCl<sub>3</sub> sourced from Oakwood Chemical. All electrochemical work was performed in a 3-compartment cell consisting of a platinum foil counter electrode separated from the cathode by a glass frit and a saturated calomel reference electrode (SCE) fixed in position through a Luggin capillary. All potentials reported in this work are with respect to the SCE. The total solution volume within the cell was 100 mL. CV studies and potentiostatic depositions for partial current and current efficiency measurements were performed on a 5 mm diameter Pt rotating disk electrode (RDE). Voltammetric sweeps were performed at 100 mV·s<sup>-1</sup>. For the TBA injection study, a Pt electrode was prepared by masking Pt foil with platers tape, exposing a 6 mm diameter circular Pt surface. This was mounted into the cell vertically and vigorous N<sub>2</sub> bubbling within the cathode compartment provided rapid removal of H<sub>2</sub> bubbles from the electrode surface. A solution of 100 mM TBA was injected into the cell in the appropriate amounts. Ruthenium partial currents and efficiencies were measured by electroplating Ru for 60 s at 400 RPM, followed immediately by rinsing with DI water and immersion into a 0.1 M KOH solution at an applied potential of 0.45 V. The integrated stripping charge was used to calculate the amount of Ru deposited using Faraday's law, assuming the Ru cathodically deposits and anodically strips from/to the same oxidation state. Thin film Ru samples were made using pieces of a silicon wafer with Pd strips as seed layers. These substrates were prepared by first thermally depositing a 50 nm layer of SiO<sub>2</sub> onto a Si wafer. The wafer was

then patterned using lithography to create a 1 mm by 10 mm strip connected to a 3 mm by 5 mm contact pad. A 10 nm layer of Ti followed by a 110 nm layer of Pd was evaporated. The photoresist was lifted off, leaving the patterned substrates. These substrates were mounted onto a chuck rotating in the same way as the RDE. Electrical connection was made through a front contact pin to the pad. The Pd seed resistance was measured directly and the resistivity was calculated as  $1.46 * 10^{-7} \Omega \cdot m$  ( $\sigma = 0.04 * 10^{-7} \Omega \cdot m$ ), where  $\sigma$  is the standard deviation.

Raman spectroscopy was performed on a Horiba LabRAM HR with a 532 nm laser. An Autolab 302N potentiostat with a frequency analyzer was used for all electrochemical work. Solution resistance was determined through electrochemical impedance spectroscopy, wherein a sinusoidal potential was applied with an RMS amplitude of 10 mV and the frequency was sampled from 0.1 Hz to 100 kHz. The solution resistance was used to correct for ohmic voltage drop in results where indicated. Thin film strip samples were cleaved from the contact pad after deposition. Film thickness was measured using a KLA Alpha-Step D-500 stylus profilometer. Measurements spanned the entire width of the strip length and were averaged over at least 3 points in the central third of the strip length. Resistances were measured using a linear four-point probe that spanned 6 mm along the centerline of the strip. The spacing between the probes was 2 mm, and the strip width was 1 mm, so a uniform current distribution was assumed, and no shape correction factors were used. X-ray diffraction (XRD) measurements were performed on a Bruker D8 Discover with GADDS and a Co K $\alpha$  x-ray source. Annealing was performed in a home-built vacuum furnace.

## Results and Discussion

### Tetrabutylammonium additive and water-in-salt electrolyte

Recently published work from our group has thoroughly investigated the mechanism of HER suppression by concentrated LiCl, and concluded that it is primarily due to an order-of-magnitude decrease in the proton diffusion coefficient arising from a disruption of the extensive hydrogen bond network within water, primarily attributable to the alkali metal cation.<sup>8</sup> No significant change is imparted on the diffusion coefficient of metal cations by the introduction of LiCl. The hydrogen bonding state of water molecules in solution can be conveniently observed by Raman spectroscopy.<sup>18-21</sup> The OH stretch band of water molecules gives rise to a broad peak at around 3400 cm<sup>-1</sup>. Although there is some controversy over the exact nature of this peak,<sup>22</sup> it is generally understood that it can be deconvoluted into 5 gaussian peaks corresponding to the primary hydrogen bonding states of water molecules. These hydrogen bonding states include DAA (single donor, dual acceptor), DDAA (dual donor, dual acceptor), DA (single donor, single acceptor), DDA (dual donor, single acceptor), and free (non-hydrogen bonding) molecules, and are centered respectively at 3063 cm<sup>-1</sup>, 3225 cm<sup>-1</sup>, 3424 cm<sup>-1</sup>, 3595 cm<sup>-1</sup>, and 3637 cm<sup>-1</sup> based on fittings of our measured spectra and in close agreement with literature. By comparing the size of these fitted peaks, it is simple to examine differences in the hydrogen bonding network under different conditions. Figure 6-1 (a) shows the Raman spectrum of DI water under ambient conditions, as well as spectra of a 4 M and an 8 M LiCl solution. Significant changes of the OH stretch band are observed. Deconvolution of the peaks, shown in Figure 6-1 (b) – (d), reveals a significant shift away from the DAA, DDA, and tetrahedrally bonded DDAA states and toward the DA state as the LiCl concentration is increased to 8 M. This shift away

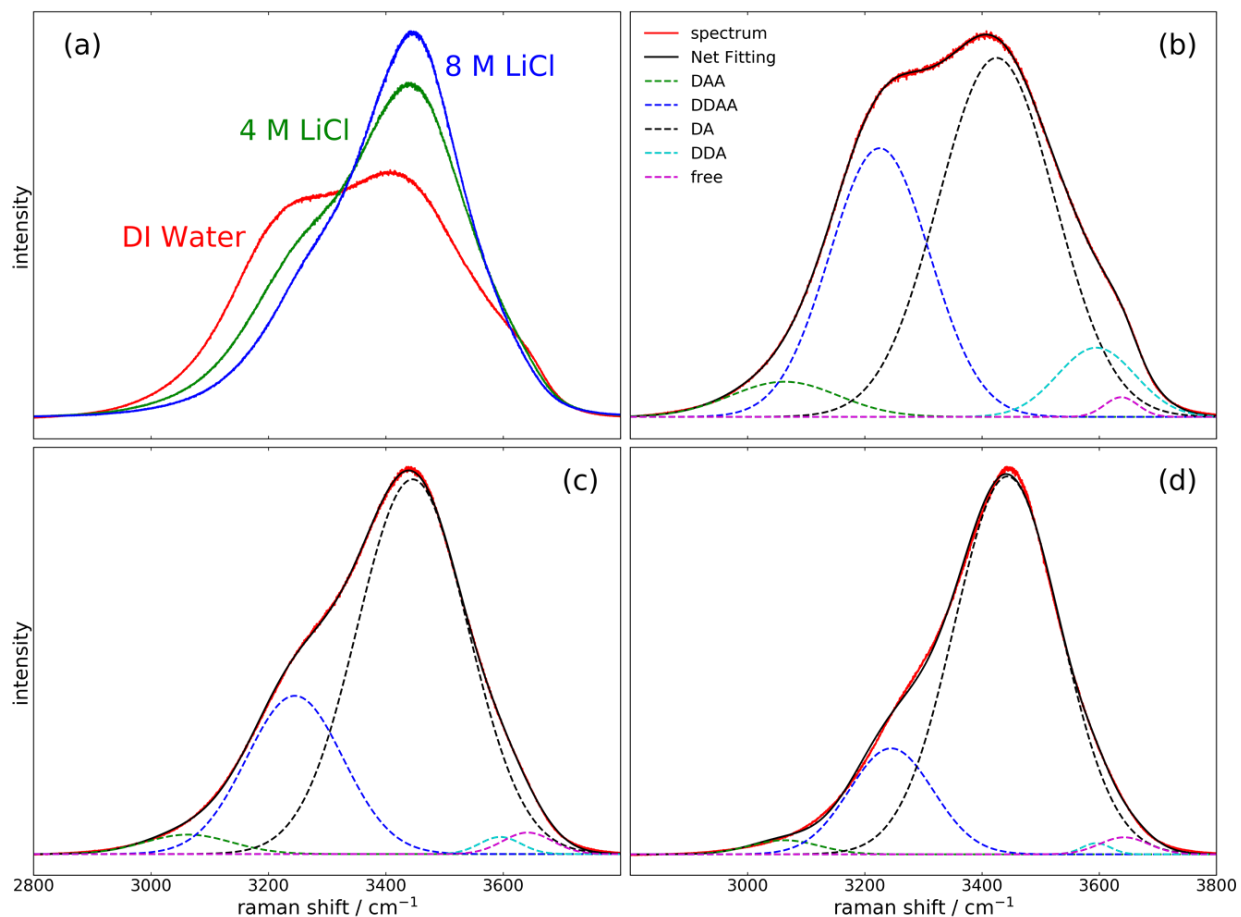


Figure 6-1. (a) Raman spectra of water with various amounts of LiCl, and (b) - (d) deconvolutions of the peaks for DI Water, 4 M LiCl, and 8 M LiCl, respectively.

from higher bonding states toward lower bonding states confirms that concentrated LiCl significantly disrupts the hydrogen bonding network, preventing fast proton diffusivity via the Grotthuss mechanism.

Proton reduction kinetics can be further suppressed by the addition of TBA to plating baths.<sup>17</sup> TBA is a hydrophobic cation that is thought to adsorb and block water molecule access to the cathode surface, and has been observed to prevent water reduction.<sup>16</sup> Stationary CVs of 0.1 M H<sub>2</sub>SO<sub>4</sub> have been performed to study the effects of additions of TBA on proton reduction. The cathodic direction sweeps of these CVs are shown in Figure 6-2 (a). Without TBA, proton reduction onsets at -0.25 V and the rate

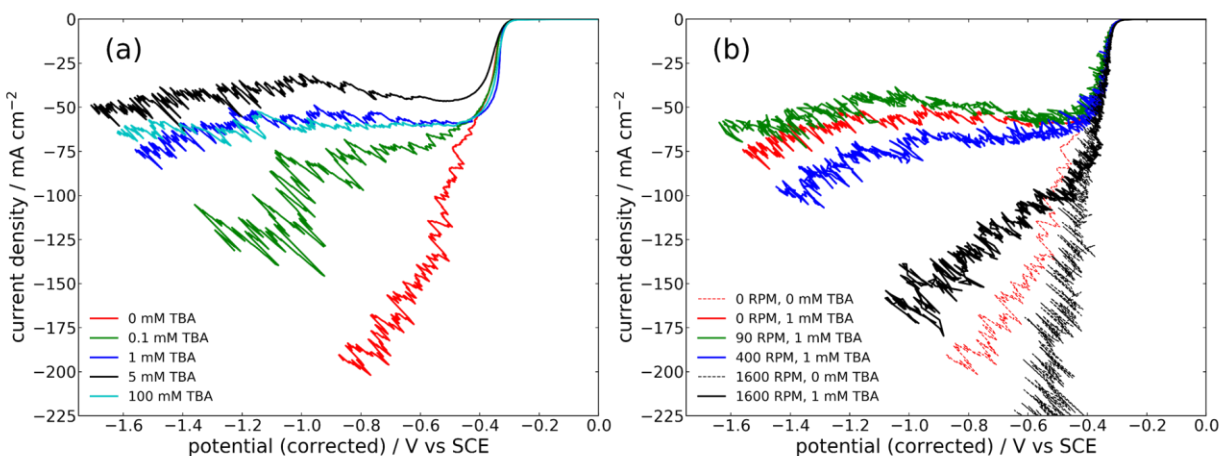


Figure 6–2. CVs of 0.1 M H<sub>2</sub>SO<sub>4</sub> with (a) various concentrations of TBA in quiescent conditions, and (b) with and without 1 mM TBA at various rotation rates.

exponentially increases, seemingly without mass transport limitations, as the applied potential is swept to -2 V. When corrected for solution IR drop, the electrode potential is limited to -0.8 V, although when considering apparent deviations from Butler-Volmer kinetics due to H<sub>2</sub> bubbles partially blocking the electrode surface, it is reasonable to conclude the actual electrode potential likely never exceeds -0.6 V as observed for rotation speeds high enough to quickly dislodge bubbles (see the dashed, black curve in Figure 6–2 (b)). The addition of 0.1 to 100 mM TBA to the electrolyte is seen to inhibit the proton reduction, with significant inhibition occurring at the smallest tested concentration of 0.1 mM and the effect becoming saturated at 1 mM TBA. Significantly more negative electrode potentials beyond -1.6 V are seen to be achievable at the same applied potential of -2 V. The current density becomes limited to less than 75 mA·cm<sup>-2</sup> throughout this range. A proton mass transport limiting current is not expected to manifest here, particularly as the dilute nature of the additive should not have a significant effect on the proton diffusivity. Instead, an interface phenomenon likely gives rise to this current limitation. Inspection of the potential region positive of -0.4 V shows that TBA does not generally result in negative

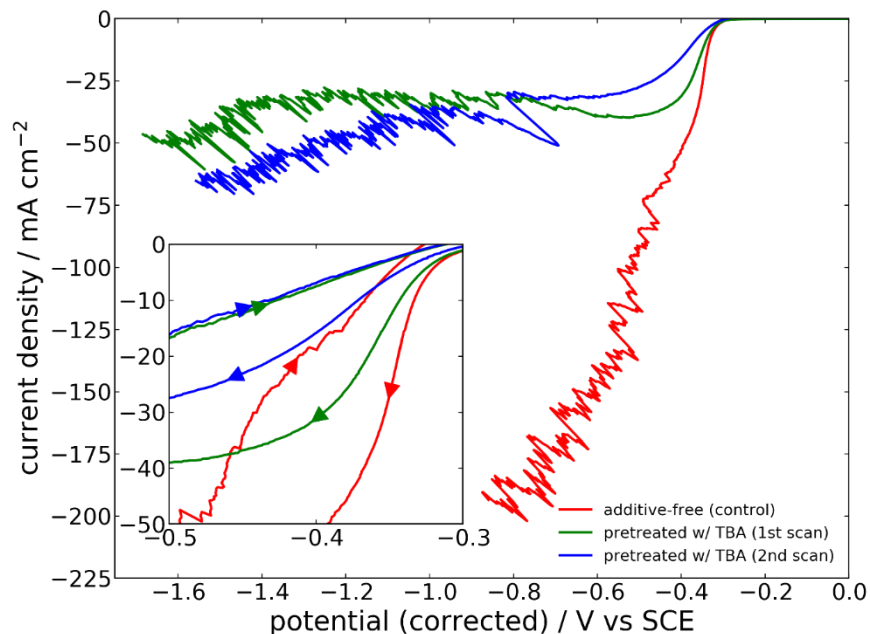


Figure 6-3. Cathodic direction sweeps of a CV cycled twice between -2 V and 1.5 V in 0.1 M H<sub>2</sub>SO<sub>4</sub> on an electrode pre-derivatized with TBA. Inset shows full CV (both cathodic and anodic direction sweeps).

current deviations from the additive-free electrolyte until more cathodic potentials are reached, and deviations become greater at more negative potentials. This suggests a potential-dependent additive adsorption process, where TBA adsorbed on the electrode surface or held within the Helmholtz plane inhibits proton reduction. While adsorbed TBA has been previously reported to prevent water reduction due to its hydrophobicity blocking access to the cathode, here it is suspected that a similar blocking of hydronium ions can inhibit proton reduction.

The HER suppressing effects of 1 mM TBA has been studied under rotating conditions as shown in Figure 6-2 (b). Gentle rotation up to 90 RPM has little effect on the suppression of proton reduction, however rotation of 400 RPM results in a slight increase of the proton reduction rate and rotating at 1600 RPM results in a proton reduction current with very little deviation from the additive-free case. To understand the mechanism of

proton adsorption/desorption, CVs were performed in additive-free electrolyte on an electrode surface that had been derivatized with TBA by immersion in 100 mM TBA for 5 min, followed by brief, gentle immersion in DI water to remove excess TBA, and gentle immersion into the electrolyte. Two CV cycles were performed, beginning at 0 V and sweeping in a negative direction to -2.0 V, with an anodic vertex of 1.5 V, shown in Figure 6-3. The suppressing effect on proton reduction is clearly observed on this derivatized electrode with no TBA in the electrolyte bulk, proving that this suppression is an interface effect. No further TBA adsorption can occur during this CV, so no effects from a potential dependent adsorption process are expected in this experiment, and the inset in Figure 6-3 shows clearly that proton reduction is inhibited from the onset. The second consecutive cycle in the CV shows similar inhibition, despite the fact that the electrode had been swept to a positive potential that might be expected to accelerate the desorption of cationic TBA. That the inhibiting effect remains nearly identical on the second scan suggests that TBA desorption is not induced by positive polarization of the electrode, and that it has slow kinetics. Gentle rotation (90 RPM) of a TBA derivatized electrode during a CV scan in additive-free electrolyte eliminates any HER inhibiting effect, indicating that electrolyte flow over the electrode surface is sufficient to cause desorption of TBA. It seems unusual that TBA adsorption is strong enough to prevent desorption even after a period of 30 seconds including a rinse in DI water, yet TBA is flushed off immediately by 90 RPM rotation. The nature and strength of TBA adsorption warrant further examination.

The dependence of proton reduction suppression on TBA concentration was examined with a potentiostatic hold experiment shown in Figure 6-4. A Pt foil electrode was mounted vertically in the additive-free electrolyte to allow easy escape of H<sub>2</sub> bubbles,

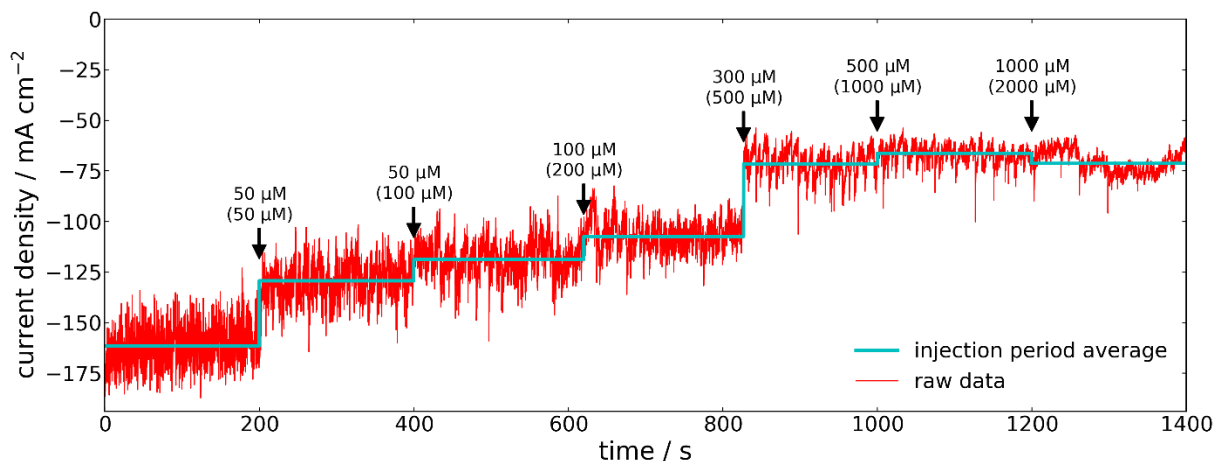


Figure 6–4. Current on a stationary Pt electrode during a potentiostatic hold at -1.5 V (applied) in 0.1 M H<sub>2</sub>SO<sub>4</sub> during TBA injections of the indicated amount (total amount). Agitation provided by vigorous N<sub>2</sub> bubbling. The average current during each injection period is shown by the cyan line.

and the applied potential was held at -1.5 V while current was recorded. TBA was injected at the indicated times, and it was found that 50 μM of TBA in solution was sufficient to achieve a noticeable decrease in HER current of 20%. Once a total of 500 μM of TBA had been injected into solution, a 56% decrease in HER current was achieved, and further additions of TBA did not further decrease the HER current.

The proton reduction inhibition at the interface by TBA was found to compound with the decrease of proton diffusivity in the bulk electrolyte caused by concentrated LiCl. Figure 6–5 shows a CV on a Pt electrode in 0.1 M H<sub>2</sub>SO<sub>4</sub>, and the individual and combined effects of 1 mM TBA and 5 M LiCl. It is notable that while water reduction is completely inhibited in the case of TBA only, electrolytes containing LiCl see an onset of water reduction at -1.0 to -1.2 V, resulting from the increased Lewis acidity of water molecules coordinated with Li cations.<sup>8</sup> Despite this, there is a potential window from the proton reduction onset until about -1.1 V where the combined effects of TBA and LiCl limit the current of the HER to below 20 mA·cm<sup>-2</sup>. Electrode potentials even more negative than this

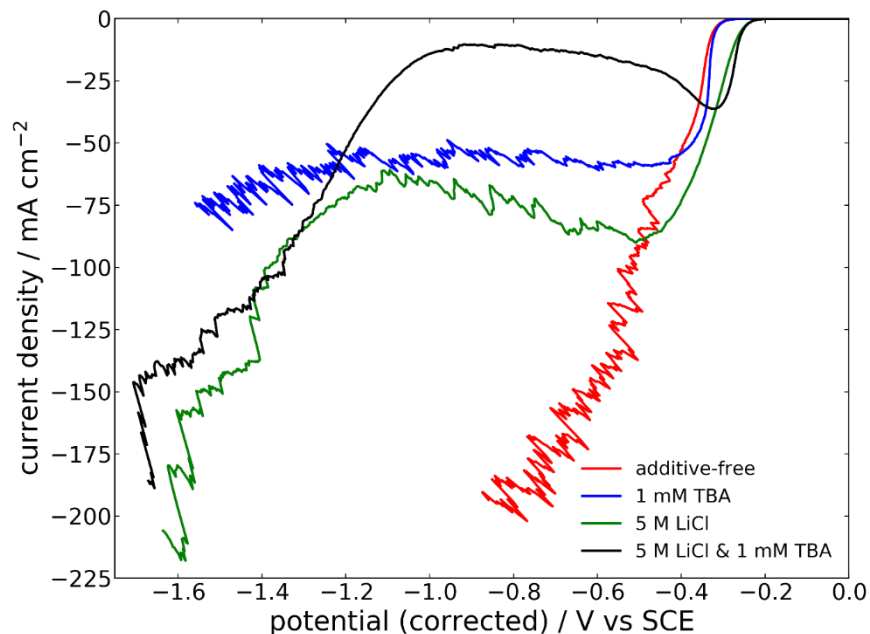


Figure 6-5. CVs of a Pt electrode in quiescent conditions in 0.1 M H<sub>2</sub>SO<sub>4</sub> with and without 1 mM TBA and/or 5 M LiCl.

are achievable, albeit with an increasing rate of hydrogen evolution. Such an expanded electrochemical window in aqueous solutions promises to enable the electrodeposition of less noble metals or metal ion complexes from aqueous solutions.

### Ruthenium deposition

The electrodeposition of Ru was studied from WiSE and the effects of TBA additive were examined. Plating baths were made by dissolving hydrated ruthenium trichloride into the electrolyte to be studied, followed by the addition of TBA if desired. A 3-electron reduction and subsequent oxidation between Ru(III) and Ru metal is assumed for partial current and current efficiency calculations, despite the fact that the plating bath can be expected to contain some amount of Ru(IV) species.<sup>7, 23</sup> The coordination chemistry of ruthenium chloride solutions is complex,<sup>24</sup> and the exact nature of the ruthenium species involved is outside the scope of this work, however indirect observations of speciation changes will be noted. It was observed that addition of ruthenium salt to the electrolyte



Figure 6–6. Photographs of Ru solutions as drops and paper stains.

containing 5 M LiCl was accompanied by gas bubble formation within the solution and a change in solution color from black to red, seen in Figure 6–6, indicative of a change in the predominant Ru species. Dissolution in a LiCl-free electrolyte did not result in color change from the black Ru salt or gas formation.

Electrodeposition of Ru is accompanied by significant hydrogen evolution resulting in a low current efficiency. Figure 6–7 shows partial currents of ruthenium deposition and current efficiencies in both additive-free electrolytes and ones containing 5 M LiCl and/or 1 mM TBA. A rotation rate of 400 RPM was used to prevent accumulation of H<sub>2</sub> bubbles on the electrode surface. A shift of approximately -300 mV in the onset potential of Ru deposition is noticed when depositing from LiCl containing electrolyte, evidence of differing Ru complexation chemistry between the two electrolytes. The use of 5 M LiCl, however, allows a greater Ru deposition rate to be obtained with a maximum of -10 mA·cm<sup>-2</sup> at an electrode potential of -0.8 V. As observed for other metal depositions,<sup>8, 10</sup> the presence of concentrated LiCl in the plating bath resulted in a decrease in the Ru deposition rate at highly cathodic potentials. Although the potential at which this occurs for Ru deposition is slightly obscured by experimental noise in the TBA free electrolyte (likely due to hydrogen bubble blockage of the electrode surface), the effect is clearly observed in the TBA containing electrolyte. This can be attributed to the formation of an insoluble

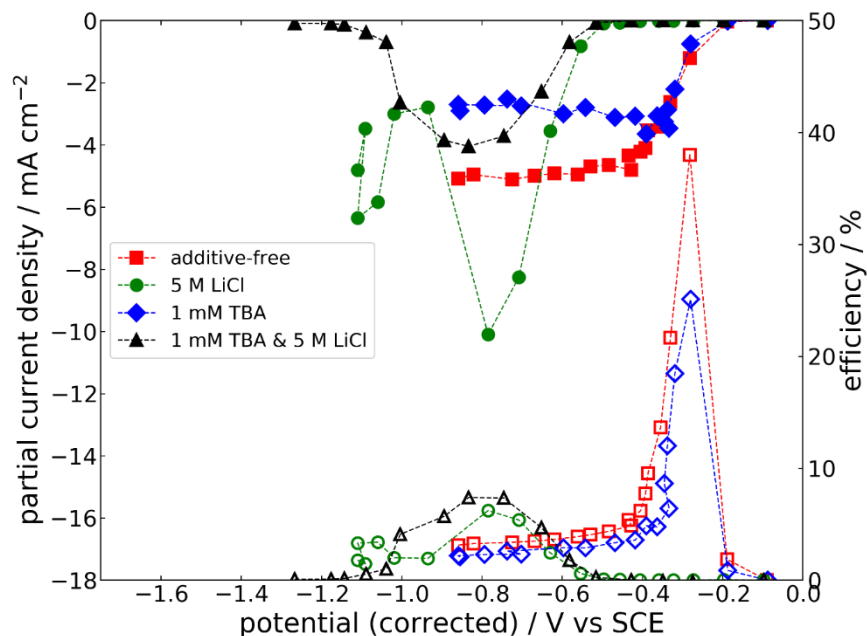


Figure 6-7. Ruthenium deposition partial currents (solid markers) and current efficiencies (outlined markers) in various electrolytes at 400 RPM.

hydroxide species at the electrode that blocks subsequent metal deposition. This could be either LiOH or ruthenium hydroxide that forms in the presence of  $\text{OH}^-$  liberated from water at highly cathodic electrode potentials.

The addition of TBA suppresses the deposition of Ru in the dilute aqueous electrolyte, limiting the partial current to  $-3 \text{ mA}\cdot\text{cm}^{-2}$  as opposed the limiting current of  $-5 \text{ mA}\cdot\text{cm}^{-2}$  that is attained from additive-free electrolyte. A similar suppression is observed in solutions containing 5 M LiCl upon addition of TBA. The inhibiting effect TBA has on proton reduction more than offsets the suppression of Ru deposition, leading to a 20% increase in peak current efficiency when TBA is used in a 5 M LiCl solution. A greater increase in current efficiency is expected if the rotation rate is reduced to 90 RPM or below, owing to a greater effectiveness of TBA. However, taking similar partial current measurements at lower rotation rates becomes infeasible because  $\text{H}_2$  bubbles accumulate on the electrode surface, particularly in less-suppressed electrolytes. The use of 5 M LiCl,

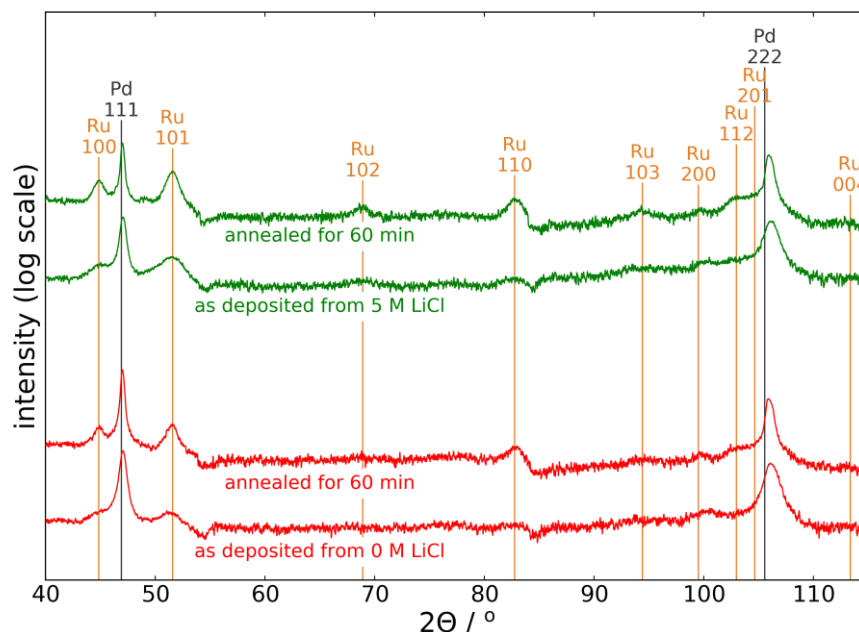


Figure 6–8. X-ray diffractograms of Ru thin films as-deposited from electrolytes containing 0 or 5 M LiCl, before and after annealing at 400 °C for 60 minutes.

particularly when combined with TBA, allows for Ru electrodeposition at improved current efficiencies between about -0.6 V and the onset of water reduction. While current efficiencies are highest in the potential range from -0.2 to -0.4 V in LiCl free electrolytes, plating rates in this region are low. Additionally, the ability to operate at highly negative potentials provides the flexibility to perform alloy electroplating with less noble metals.

Four Ru thin film samples have been electrodeposited from an additive free electrolyte and six from an electrolyte containing 5 M LiCl to study the differences in some properties relevant to interconnect applications, including resistivity and crystallinity. Film thicknesses cover a range from 215 nm to 1075 nm, although no thickness dependence was observed among the properties studied. Resistivities were calculated from the overall strip resistance using a model consisting of the Pd seed layer in parallel with the electrodeposited Ru thin film. The samples deposited from the additive-free electrolyte had resistivities of  $1.09 \times 10^{-6} \Omega \cdot \text{m}$  ( $\sigma = .20 \times 10^{-6} \Omega \cdot \text{m}$ ), whereas the samples deposited from

the 5 M LiCl electrolyte has resistivities of  $1.51 * 10^{-6} \Omega \cdot m$  ( $\sigma = .21 * 10^{-6} \Omega \cdot m$ ). These values are significantly higher than the reported bulk resistivity of Ru of  $7.1 * 10^{-8} \Omega \cdot m$ ,<sup>25</sup> a difference possibly accounted for by a high incorporation of chloride or other impurities within the deposit, and the nano-crystalline atomic order within the as-deposited films. X-ray diffractograms of as-deposited thin films presented in Figure 6–8 have only very broad peaks corresponding to Ru crystal lattice, indicating that large grains are not formed. By applying the Scherrer formula to the Ru (101) peak while accounting for instrumental line broadening of  $0.3^\circ$  and assuming a shape factor of 0.9, the average grain size in Ru films deposited from 0 and 5 M LiCl electrolytes is determined to be 7.6 and 6.5 nm, respectively. Upon annealing for 60 minutes at  $400^\circ C$ , an emergence of the Ru peaks is noted in samples deposited from solutions containing both 0 and 5 M LiCl, indicating that electrodeposited Ru can undergo grain growth at  $400^\circ C$  despite the probable presence of impurities within the film. After annealing, the average grain size grew to 26 and 24 nm for films deposited from 0 M LiCl and 5 M LiCl electrolytes, respectively. Despite grain growth upon annealing, no decrease in the resistivities could be measured, although this is likely due to delamination of the Ru thin film that occurred near the edges of the strip during annealing, resulting in an irregular Ru strip and inaccurate model for calculating resistivities from the measured resistance.

## **Conclusion**

The proton diffusivity decrease by concentrated LiCl is confirmed to be due to a disruption of the extensive hydrogen bonding network present within dilute solutions. The hydrophobic cation TBA adsorbs onto the electrode surface with a potential-dependent rate. Upon adsorption, hydronium access to the surface is blocked and proton reduction to

hydrogen is inhibited. The inhibiting effects of WiSE and TBA can be combined to significantly decrease the rate of hydrogen evolution, and provide an expanded electrochemical window beyond -1 V vs SCE within which electrodeposition of materials can be feasibly performed. This has been proven for the electrodeposition of Ru, where, despite the transition to a less noble complex found in water-in-salt electrolytes, Ru deposition can proceed with greater efficiency at potentials much more negative than proton reduction. Electrodeposited thin films were found to be nano-crystalline, however grain growth could be induced by annealing at 400 °C. Resistivities of the Ru films were higher than expected for bulk Ru, likely due to the nanocrystalline structure and impurities within the film.

### **Acknowledgements**

The authors wish to thank Matthew Confer and Dr. Jair Lizarazo-Adarme for training and support on Raman and profilometer instrumentation, the University of Alabama Central Analytical Facility for support with XRD, and Rick Smith at the Department of Chemistry Glassblowing Facility for fabricating the electrochemical cells.

### **References**

1. Adelman, C.; Gong Wen, L.; Peter, A.; Kong Siew, Y.; Croes, K.; Swerts, J.; Popovici, M.; Sankaran, K.; Pourtois, G.; Van Elshocht, S.; Bömmels, J.; Tokei, Z., *Alternative metals for advanced interconnects*. 2014; p 173-176.
2. Fuchs, K. In *The conductivity of thin metallic films according to the electron theory of metals*, Mathematical Proceedings of the Cambridge Philosophical Society, Cambridge University Press: 1938; pp 100-108.
3. Sondheimer, E. H., The mean free path of electrons in metals. *Advances in physics* **1952**, *1* (1), 1-42.

4. Xunyuan, Z.; Huai, H.; Patlolla, R.; Wei, W.; Mont, F. W.; Juntao, L.; Chao-Kun, H.; Liniger, E. G.; McLaughlin, P. S.; Labelle, C.; Ryan, E. T.; Canaperi, D.; Spooner, T.; Bonilla, G.; Edelstein, D. In *Ruthenium interconnect resistivity and reliability at 48 nm pitch*, 2016 IEEE International Interconnect Technology Conference / Advanced Metallization Conference (IITC/AMC), 23-26 May 2016; 2016; pp 31-33.
5. Veen, M. H. v. d.; Heyler, N.; Pedreira, O. V.; Ciofi, I.; Decoster, S.; Gonzalez, V. V.; Jourdan, N.; Struyf, H.; Croes, K.; Wilson, C. J.; Tókei, Z. In *Damascene Benchmark of Ru, Co and Cu in Scaled Dimensions*, 2018 IEEE International Interconnect Technology Conference (IITC), 4-7 June 2018; 2018; pp 172-174.
6. Rao, C. R. K.; Trivedi, D. C., Chemical and electrochemical depositions of platinum group metals and their applications. *Coordination Chemistry Reviews* **2005**, *249* (5), 613-631.
7. Jones, T., Electroplating of ruthenium. *Metal finishing* **2001**, *6* (99), 121-128.
8. De, S.; White, J.; Brusuelas, T.; Patton, C.; Koh, A.; Huang, Q., Electrochemical Behavior of Protons and Cupric Ions in Water in Salt Electrolytes with Alkaline Metal Chloride. *in preparation* **2019**.
9. Huang, Q.; Hu, Y., Electrodeposition of Superconducting Rhenium with Water-in-Salt Electrolyte. *Journal of The Electrochemical Society* **2018**, *165* (16), D796-D801.
10. Huang, Q.; Lyons, T. W., Electrodeposition of rhenium with suppressed hydrogen evolution from water-in-salt electrolyte. *Electrochemistry Communications* **2018**, *93*, 53-56.
11. Suo, L.; Hu, Y.-S.; Li, H.; Armand, M.; Chen, L., A new class of Solvent-in-Salt electrolyte for high-energy rechargeable metallic lithium batteries. *Nat. Commun.* **2013**, *4*, 1481.
12. Suo, L.; Borodin, O.; Gao, T.; Olguin, M.; Ho, J.; Fan, X.; Luo, C.; Wang, C.; Xu, K., "Water-in-salt" electrolyte enables high-voltage aqueous lithium-ion chemistries. *Science* **2015**, *350* (6263), 938.
13. Kühnel, R.-S.; Reber, D.; Remhof, A.; Figi, R.; Bleiner, D.; Battaglia, C., "Water-in-salt" electrolytes enable the use of cost-effective aluminum current collectors for aqueous high-voltage batteries. *Chemical Communications* **2016**, *52* (68), 10435-10438.

14. Bin, D.; Wang, F.; Tamirat, A. G.; Suo, L.; Wang, Y.; Wang, C.; Xia, Y., Progress in Aqueous Rechargeable Sodium-Ion Batteries. *Advanced Energy Materials* **2018**, *8* (17), 1703008.
15. Agmon, N., The Grotthuss mechanism. *Chemical Physics Letters* **1995**, *244* (5), 456-462.
16. Dubouis, N.; Serva, A.; Salager, E.; Deschamps, M.; Salanne, M.; Grimaud, A., The Fate of Water at the Electrochemical Interfaces: Electrochemical Behavior of Free Water Versus Coordinating Water. *The journal of physical chemistry letters* **2018**, *9* (23), 6683-6688.
17. Sides, W.; Hassani, E.; Oh, T.-S.; Pappas, D. P.; Hu, Y.; Huang, Q., Grain Growth and Superconductivity of Rhenium Electrodeposited from Water-in-Salt Electrolytes. *In preparation* **2019**.
18. Moskovits, M.; Michaelian, K. H., A reinvestigation of the Raman spectrum of water. *The Journal of Chemical Physics* **1978**, *69* (6), 2306-2311.
19. Li, R.; Jiang, Z.; Chen, F.; Yang, H.; Guan, Y., Hydrogen bonded structure of water and aqueous solutions of sodium halides: a Raman spectroscopic study. *Journal of Molecular Structure* **2004**, *707* (1), 83-88.
20. Furić, K.; Ciglencčki, I.; Čosović, B., Raman spectroscopic study of sodium chloride water solutions. *Journal of Molecular Structure* **2000**, *550-551*, 225-234.
21. Sun, Q., Raman spectroscopic study of the effects of dissolved NaCl on water structure. *Vibrational Spectroscopy* **2012**, *62*, 110-114.
22. Auer, B. M.; Skinner, J. L., IR and Raman spectra of liquid water: Theory and interpretation. *The Journal of Chemical Physics* **2008**, *128* (22), 224511.
23. Rard, J. A., Chemistry and thermodynamics of ruthenium and some of its inorganic compounds and aqueous species. *Chemical Reviews* **1985**, *85* (1), 1-39.
24. Greenwood, N. N.; Earnshaw, A., 25. Iron, Ruthenium and Osmium. In *Chemistry of the Elements (2nd Edition)*, Elsevier.

25. Electrical Resistivity of Pure Metals. In *CRC Handbook of Chemistry and Physics*, 100th Edition (Internet Version 2019) ed.; Rumble, J. R., Ed. CRC Press/Taylor & Francis, Boca Raton, FL.

## CHAPTER 7. CONCLUSIONS AND RECOMMENDATIONS

The electroplating of metals, as well as binary and tertiary alloys, has been studied from a variety of electrolytes designed to reduce side reactions, namely proton reduction, while operating at highly cathodic potentials. The nucleation and growth of a binary codeposition system have been characterized with regard to the effects of a negative Gibbs free energy of compound formation.<sup>1</sup> Deep eutectic solvents provide a direct method to eliminate proton reduction by removing the reactant species from the solution altogether. A deep eutectic solvent is used to electrodeposit metallic manganese,<sup>2</sup> and this capability is extended to incorporate manganese into a ferromagnetic tertiary Co-Fe-Mn alloy.<sup>3</sup> An interesting finding from these studies is that manganese deposition becomes inhibited at sufficiently negative electrode potentials. Throughout this work, similar behavior has been observed, whether in deep eutectic solvents or water-in-salt electrolytes, for metals including Co, Mn, Re, Ru. There are certainly likely to be multiple and differing causes of this behavior in the different metal/electrolyte systems, however the exact cause is not well understood in any case. While in some cases, a passivating layer is believed to form on the substrate, in other cases there is the possibility of further reduction of the metal deposit to a soluble anionic species.

A highly concentrated solution of LiCl, known as water-in-salt, has been employed for the electrodeposition of Mn, Re,<sup>4</sup> and Ru metals,<sup>5</sup> and a Mn-Re alloy. A disruption of the hydrogen bonding network within the electrolyte was shown to be the cause of a significant decrease in proton diffusivity. Additionally, the tetrabutylammonium cation

causes a surface inhibition of proton reduction, which can further decrease the rate of hydrogen evolution at significant overpotentials to proton reduction. While hydrogen evolution is not eliminated in these electrolytes, it is inhibited enough to achieve metal deposition at potentials 1.8 V more negative than the onset of proton reduction. Such a widening of the electrochemical window in aqueous electrolytes promises to enable aqueous electroplating of numerous metals which had previously been plagued by prohibitively low current efficiencies. Additionally, alloys can be easily plated from a single bath. While significant proton reduction inhibition has been demonstrated, further inhibition is likely possible with the optimization of the proton, LiCl, and TBA concentrations and the agitation rate.

Electrodeposited rhenium has recently been found to possess an elevated critical temperature of superconductivity.<sup>6-7</sup> A significant outcome of this work is the attribution of this property to the disordered atomic structure within electrodeposited rhenium. Electrodeposition is a non-equilibrium process, enabling the fabrication of materials in a metastable, disordered state; in the case of rhenium, this achieves an enhanced critical temperature. Once deposited in a disordered state, grain growth becomes detrimental to the enhanced critical temperature. It has been shown that maintaining film thickness below a critical value around 270 nm prevents grain growth within the films. It is also demonstrated that impurities incorporated within the rhenium inhibit grain growth, and that hydrogen present in the annealing atmosphere encourages grain growth.

In addition to the many benefits electrodeposition enjoys as a fabrication method of superconducting materials for devices from a practical standpoint, this method for fabricating superconducting rhenium allows for easy fabrication and study of alloy

superconductors. Some rhenium alloys have been found to have significantly higher critical temperatures than elemental rhenium.<sup>8</sup> Water-in-salt electrolytes enable the flexibility to codeposit binary rhenium alloys from a single bath, such as Re-Ru and Mn-Re. This capability provides a convenient way to study enhanced superconductivity in electrodeposited Re alloys. It is not known whether these alloys would benefit from a disordered atomic structure, as such behavior is rather unusual among the known superconducting materials, although this is certainly worth pursuing. Alloys that cannot be codeposited from a single bath, such as Re-Mo, could still likely be fabricated by electrodepositing multilayers of the elements from individual baths, followed by a high temperature thermal treatment to achieve a homogenous alloy phase. While such a process may result in grain growth within the films, it still provides a convenient fabrication pathway for a relatively high critical temperature material. Whether from a single bath or not, the electrodeposition of superconducting metals and alloys certainly warrants further exploration.

## References

1. Sides, W. D.; Huang, Q., Electrochemical Nucleation and Growth of Antimony Telluride Binary Compound on Gold Substrate. *Journal of The Electrochemical Society* **2018**, *165* (11), D568-D573.
2. Sides, W. D.; Huang, Q., Electrodeposition of manganese thin films on a rotating disk electrode from choline chloride/urea based ionic liquids. *Electrochimica Acta* **2018**, *266*, 185-192.
3. Sides, W.; Kassouf, N.; Huang, Q., Electrodeposition of Ferromagnetic FeCo and FeCoMn Alloy from Choline Chloride Based Deep Eutectic Solvent. *Journal of The Electrochemical Society* **2019**, *166* (4), D77-D85.

4. Sides, W.; Hassani, E.; Oh, T.-S.; Pappas, D. P.; Hu, Y.; Huang, Q., Grain Growth and Superconductivity of Rhenium Electrodeposited from Water-in-Salt Electrolytes. *In preparation* **2019**.
5. Sides, W. D.; Huang, Q., Ruthenium Electrodeposition from Water-in-Salt Electrolytes for Interconnect Applications and the Influence of Tetrabutylammonium. *In preparation* **2019**.
6. Huang, Q.; Hu, Y., Electrodeposition of Superconducting Rhenium with Water-in-Salt Electrolyte. *Journal of The Electrochemical Society* **2018**, *165* (16), D796-D801.
7. Pappas, D. P.; David, D. E.; Lake, R. E.; Bal, M.; Goldfarb, R. B.; Hite, D. A.; Kim, E.; Ku, H. S.; Long, J. L.; McRae, C. R. H.; Pappas, L. D.; Roshko, A.; Wen, J. G.; Plourde, B. L. T.; Arslan, I.; Wu, X., Enhanced superconducting transition temperature in electroplated rhenium. *Applied Physics Letters* **2018**, *112* (18), 182601.
8. Testardi, L. R.; Hauser, J. J.; Read, M. H., Enhanced superconducting T<sub>c</sub> and structural transformation in Mo-Re alloys. *Solid State Communications* **1971**, *9* (21), 1829-1831.

## APPENDIX

### Ongoing Work

#### Manganese and Mn-Re alloys

Manganese has been studied previously in this work as a metal whose low deposition potential ( $-1.2$  V vs. proton reduction) precludes its electrodeposition from typical aqueous electrolytes. While its deposition from a choline chloride based deep eutectic solvent has been demonstrated, there is still interest in depositing metallic Mn from aqueous electrolyte baths.<sup>1</sup> The use of water-in-salt electrolytes to electrodeposit manganese is examined in this chapter. Its codeposition is examined to deposit a Mn-Re alloy from a single bath.

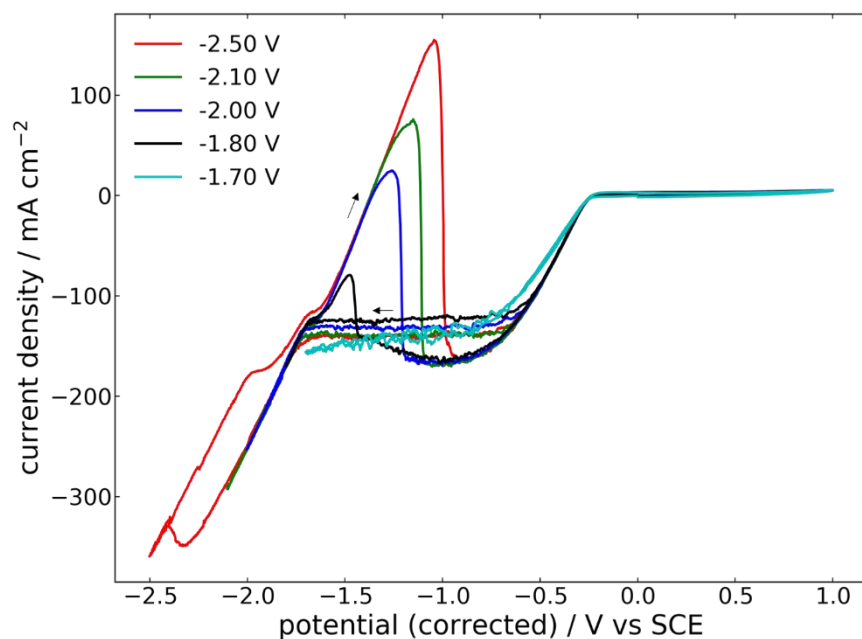


Figure A 1. Cyclic voltammograms on a Pt RDE rotating at 1600 RPM to different cathodic potentials in an electrolyte containing 0.2 M MnCl<sub>2</sub>, 5 M LiCl, and 0.1 M HCl.

Figure A 1 shows cyclic voltammograms taken in a water-in-salt electrolyte containing 0.2 M Mn(II). As is typical for these electrolytes, a mass-transfer limiting current is observed for the proton reduction reaction, made possible by concentrated Li<sup>+</sup> ions interrupting proton diffusion along hydrogen bonding networks.<sup>2</sup> An anodic peak on the reverse scan, beginning near -1.65 V, appears with increasing area on scans that were swept to -1.8 V or beyond, providing evidence that Mn<sup>2+</sup> is reduced to Mn metal at these potentials. Due to the relatively high concentration of Mn in this experiment, the cathodic current of Mn<sup>2+</sup> reduction is clearly visible as a wave beginning at -1.75 V, which peaks at -2.35 V due to hydroxide formation on the electrode surface, similarly to behavior noted in Chapters 3 through 6. Mn deposition partial current measurements in this system, shown in Figure A 2, show that this current wave is initially due entirely to Mn reduction, however this reaction is suppressed at potentials more negative than -2.1. Despite this, a

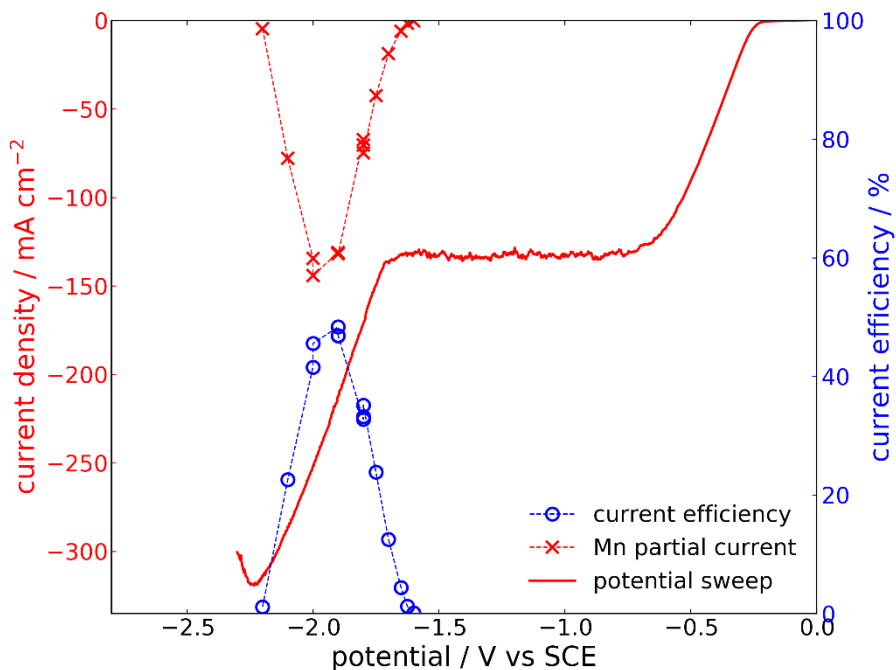


Figure A 2. Negative-direction sweep of a CV in the same conditions as Figure A 1, showing partial currents and current efficiencies of Mn deposition measured by potentiostatic stripping analysis.

rising current wave is still observed in CVs beyond this potential, indicating the onset of water reduction. Indeed, this water reduction and the subsequently high concentration of hydroxide are likely the reason that Mn deposition is inhibited beyond -2.1 V.

The single bath codeposition of Mn and Re was demonstrated for this water-in-salt electrolyte. Figure A 3 shows CVs taken in a solution containing 10 mM of Mn(II) as well as 25 mM of Re(VII). Also shown are measurements of the Mn content in Mn-Re films deposited potentiostatically for 60 s. The shape of the anodic stripping peaks for a given CV potential limit, combined with the XRF determinations of deposit composition, reveals the Faradaic processes occurring at various potentials. At potentials positive of -0.8 V, no stripping peak is observed indicating cathodic current is entirely proton reduction. A single stripping peak corresponding to Re oxidation first emerges as the potential is swept to -0.9 V. CV sweeps to potentials of -1.3 V or beyond result in a more complex stripping peak,

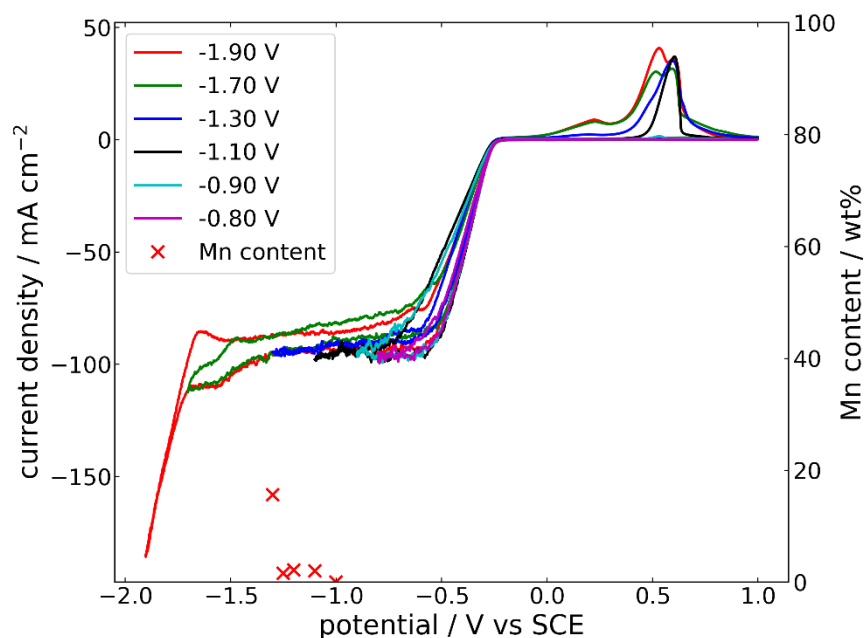


Figure A 3. Cyclic voltammograms on a Pt RDE rotating at 1600 RPM to different cathodic potentials in an electrolyte containing 10 mM  $\text{MnCl}_2$ , 25 mM  $\text{NH}_4\text{ReO}_4$ , 5 M LiCl, and 0.1 M HCl. Markers show Mn content of films deposited potentiostatically at the indicated potential.

with up to three discernable components. While the most positive peak has been identified as Re oxidation, the other two are likely oxidation of a Mn-Re alloy. In this case, the Mn stripping peak is significantly shifted toward more positive values versus the stripping peaks observed for pure Mn. This can be possible because of the Gibbs energy of compound formation, as demonstrated in Chapter 2. Composition measurements support this conclusion, and in fact show that Mn undergoes underpotential deposition (UPD) with Re, wherein deposits contain about 2% Mn if deposited from -1.1 V to -1.25 V, well above the onset deposition potential of pure Mn deposition. Such an UPD phenomenon further indicates that a Mn-Re alloy is more thermodynamically stable than the elemental metals.<sup>3</sup>

Measurements of the superconductivity of deposits obtained from this system show superconductivity with a  $T_c$  similar to the Re films deposited from the pure Re bath described in Chapter 5 only for films deposited positive of -1.0 V, which contained no traces of Mn. Films deposited at more negative potentials, which incorporated small amounts of Mn (as little as 0.1%) were not found to be superconductive at any temperature down to 1.8 K.

This water-in-salt electrolyte has been shown to enable the easy electrodeposition of Mn from an aqueous electrolyte. A relatively high concentration of metal ions can achieve current efficiencies up to 50% by limiting the proton evolution side reaction. The codeposition from a single bath of Mn-Re alloys has also been shown to be feasible using this electrolyte.

### **Molybdenum rhenium alloys**

The superconducting Mo-Re alloy has been found to have a superconducting critical temperature of up to 13 K, and as such has found interest for applications in

superconducting electronics.<sup>4-7</sup> Attempts to electrodeposit molybdenum from a water-in-salt electrolyte containing 10 mM  $\text{Na}_2\text{MoO}_4$  were unsuccessful, preventing Mo incorporation into a superconducting alloy Mo-Re from a single bath. As an alternate approach, the Mo plating procedures described by Duan *et al.*<sup>8</sup> were used to deposit a layer of Mo on Au-seeded substrates. A current density of  $2.5 \text{ A}\cdot\text{cm}^{-2}$  was employed to minimize oxygen incorporation. Subsequently, a water-in-salt electrolyte containing 5 M LiCl, 0.1 M  $\text{H}_2\text{SO}_4$ , and 25 mM perrhenate was used to deposit a layer of rhenium. Finally, a 20 nm layer of protective Au was sputtered. A cross-section of the resulting layered structures is presented in Figure A 4. Electrodeposited Mo films without Re did not exhibit superconductivity down to 1.8 K, the lowest temperature our tests are capable of. Mo is expected to have a  $T_c$  of 0.9 K,<sup>9</sup> so this was not an unexpected result. However, the complete

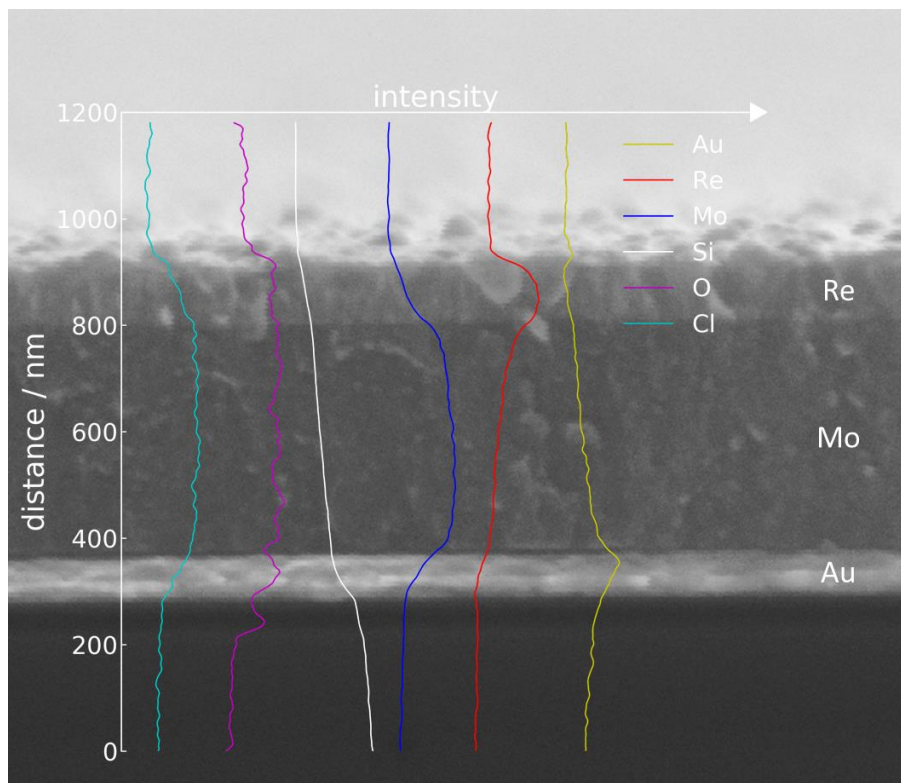


Figure A 4. Cross-section SEM image of a Au/Mo/Re/Au stacked structure fabricated on a Si/SiO<sub>2</sub> substrate. Overlain EDS measurements are scaled to the maximum intensity measured for each element.

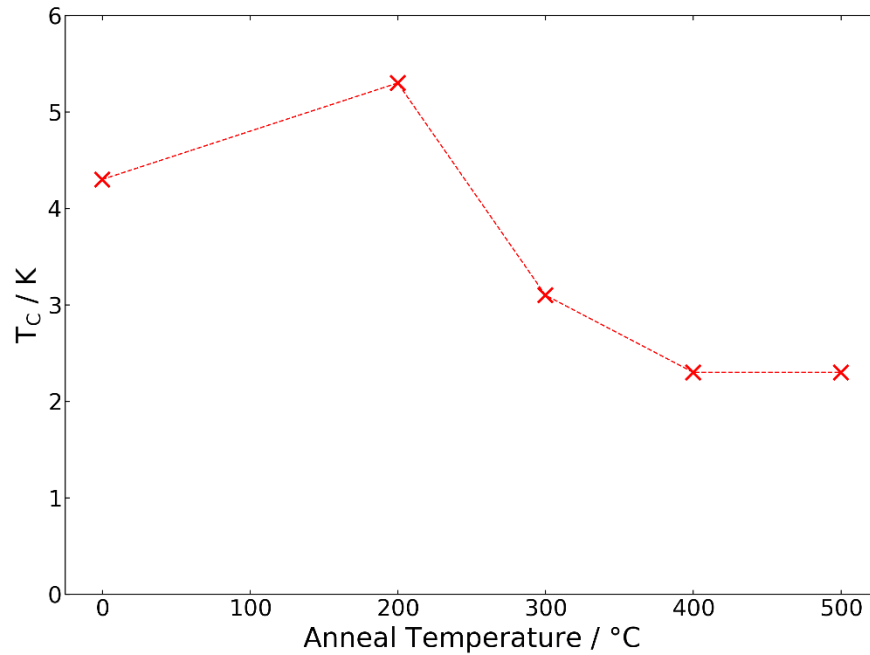


Figure A 5. Superconducting critical temperature of a Re/Mo layered structure after annealing treatments for 30 minutes each at various temperatures.

Mo/Re stack exhibited superconductivity with transition temperatures of 4.3 to 5.2 K, consistent with observations for Re thin films. Vacuum annealing was performed at various temperatures up to 500 °C in attempts to cause the Mo and Re to interdiffuse, achieving a homogenous Mo-Re alloy with enhanced superconductivity. Subsequent EDS measurements showed that no noticeable interdiffusion between the metal layers was achieved, however a decrease of the  $T_c$  was noted as the structure was annealed at higher temperatures, as seen in Figure A 5. This behavior is likely due solely to grain growth in the Re layer. While the film is thin enough to resist grain growth at 200 °C, higher annealing temperatures are capable of achieving some grain growth and subsequently reducing the  $T_c$ . It is worth noting that the  $T_c$  appears to reach a minimum value of 2.3 K once annealed at 400 °C, and higher annealing temperatures do not cause a further reduction. This is still a slightly enhanced  $T_c$  for Re, and indicates that in these thin Re films, grain growth is still somewhat inhibited at 500 °C.

## References

1. Gong, J.; Zangari, G., Electrodeposition and Characterization of Manganese Coatings. *Journal of The Electrochemical Society* **2002**, *149* (4), C209-C217.
2. De, S.; White, J.; Brusuelas, T.; Patton, C.; Koh, A.; Huang, Q., Electrochemical Behavior of Protons and Cupric Ions in Water in Salt Electrolytes with Alkaline Metal Chloride. *in preparation* **2019**.
3. Porter, D. A.; Easterling, K. E.; Sherif, M., *Phase Transformations in Metals and Alloys, (Revised Reprint)*. CRC press: 2009.
4. Testardi, L. R.; Hauser, J. J.; Read, M. H., Enhanced superconducting T<sub>c</sub> and structural transformation in Mo-Re alloys. *Solid State Communications* **1971**, *9* (21), 1829-1831.
5. Andreone, A.; Barone, A.; Chiara, A. D.; Mascolo, G.; Palmieri, V.; Peluso, G.; Uccio, U. S. d., Mo-Re superconducting thin films by single target magnetron sputtering. *IEEE Transactions on Magnetics* **1989**, *25* (2), 1972-1975.
6. Singh, V.; Schneider, B. H.; Bosman, S. J.; Merkkx, E. P. J.; Steele, G. A., Molybdenum-rhenium alloy based high-Q superconducting microwave resonators. *Applied Physics Letters* **2014**, *105* (22), 222601.
7. Sundar, S.; Banik, S.; Chandra, L. S.; Chattopadhyay, M.; Ganguli, T.; Lodha, G.; Pandey, S. K.; Phase, D.; Roy, S., Electronic structure of Mo<sub>1-x</sub>Re<sub>x</sub> alloys studied through resonant photoemission spectroscopy. *Journal of Physics: Condensed Matter* **2016**, *28* (31), 315502.
8. Duan, F. H.; Lin, Y.; Pan, J.; Wang, Y. X.; Yao, J. H.; Li, Y., Influence of oxygen on the glass formation of Mo-O binary alloys. *Journal of Non-Crystalline Solids* **2018**, *500*, 210-216.
9. Matthias, B. T.; Geballe, T. H.; Compton, V. B., Superconductivity. *Reviews of Modern Physics* **1963**, *35* (1), 1-22.